

# Reconstructing Chemistry from $P_0$ : A Three-Dimensional Energy Continuum Framework (20260410)

Liu Heng  
86808600@qq.com

## Abstract

This paper develops the  $P_0$  energy-continuum framework for chemistry, derived from the companion physics monograph [1], which establishes the continuum-mechanical foundations. The framework reconstructs chemical phenomena from one axiom ( $P_0$ : total energy partitions into propagating and topologically locked components), two topological postulates (T1: electric charge as vortex winding number; T2: electron geometry as horn-torus), and five empirical continuum constants ( $\epsilon_0$ ,  $\mu_0$ ,  $c$ ,  $\nu$ ,  $\hbar$ ).

**What the framework derives (Class A: structural derivations).** The derivation chain  $P_0 \rightarrow \text{continuity} \rightarrow \text{Euler} \rightarrow \text{NS} \rightarrow \text{Madelung} \rightarrow \text{NLSE} \rightarrow \text{Schrödinger}$  is algebraically exact given the five empirical constants and two declared correspondences [DC1, DC8] whose precise scope and dimensional status are documented in §1.14. From the resulting acoustic Schrödinger equation, the framework derives the functional *forms* of the Nernst equation, Arrhenius equation, Born–Landé lattice energy, Henderson–Hasselbalch equation, and Butler–Volmer kinetics without additional postulates. All standard results of non-relativistic quantum chemistry that follow from the linear Schrödinger equation are reproduced within this framework.

**Non-trivial predictions (Class NT: zero-parameter results).** Two results are derived without fitting any parameter to the predicted quantity: (i) the tetrahedral bond angle (109.47) as the global minimum of the four-body Thomson problem on  $S^2$ —in exact agreement with the methane geometry; (ii) the Hückel  $4n+2$  aromaticity rule from cyclic standing-wave boundary conditions. These are the framework’s only predictions that are independent of empirical inputs in the quantity being compared.

**Consistency checks (Class B).** All other numerical comparisons with experiment—including the Daniell cell EMF (1.102 V), combustion enthalpies, ionic lattice energies, ionisation energies, the Fe-catalysed Haber barrier (148 kJ mol<sup>−1</sup>, using the uncatalysed barrier as calibration input), and quantum dot confinement energies (2–6% error using bulk effective masses)—are computed by inserting NIST tabulated data into Class A equations. These results confirm internal consistency with the NIST dataset; they are not independent predictions of the framework.

**FP-New force field (Track 2).** The proposed FP-New computational method pre-tabulates acoustic stiffness constants fitted to quantum-chemical potential-energy surfaces and uses the Fast Multipole Method (FMM; Greengard & Rokhlin 1987) to evaluate pair interactions in  $\mathcal{O}(N \log N)$  operations. The  $\mathcal{O}(N \log N)$  scaling is a standard FMM result, not a novel  $P_0$  derivation. All force-field parameters ( $K$ ,  $W$ , partial charges) are empirically fitted; FP-New is a parameterised force field, not a parameter-free method. Its computational advantage over Kohn–Sham DFT [ $\mathcal{O}(N^3)$  SCF cycle] in scaling is established analytically; its quantitative accuracy relative to DFT benchmarks has not yet been validated and remains an open experimental question.

**Acknowledged open gaps (OG-0 through OG-7).** The framework contains eight documented structural gaps: the Burgers-vortex stability threshold (OG-0); the two-phase viscosity inconsistency between background ( $\nu_{\text{bg}} \approx 2 \times 10^{-35} \text{ m}^2 \text{ s}^{-1}$ ) and vortex-core ( $\nu_{\text{core}} = \hbar/(2m_e) \approx 5.79 \times 10^{-5} \text{ m}^2 \text{ s}^{-1}$ ) regimes, which prevents a globally self-consistent single-phase N-S description (OG-0b); the Gaussian-ansatz approximation for the NLSE quintic coefficient  $\gamma$  (OG-1); the uncomputed particle mass ratio  $m_p/m_e$  from the NLSE eigenvalue problem, the  $6\pi^5 \approx 1836$  value having been retracted (OG-2); the planar approximation in the spin angular-momentum integral (OG-3); the spin-statistics theorem, invoked from relativistic quantum field theory (OG-4); the zero-temperature limit in the  $\alpha(s)$  interpolation (OG-5); and the E2 anti-periplanar preference, not derivable from acoustic phase-matching alone (OG-E2). All gaps are labelled **[OPEN GAP]** or **[LIMITATION]** at their point of occurrence.

**Relationship to standard quantum chemistry.** The  $P_0$  framework is a *reinterpretation*, not a replacement, of quantum chemistry: it demonstrates that the mathematical structure of the Schrödinger equation and associated formalism can be obtained from classical viscous compressible fluid mechanics given the five empirical constants above. It does not reduce the number of independent empirical inputs below five, does not derive the values of those constants, and for the cases examined here does not provide predictive accuracy beyond standard quantum chemistry. The open gaps define a concrete research agenda; the falsifiable experimental predictions listed in the Epilogue provide the tests required to assess the framework's validity beyond its Class NT results.

**Axiom  $P_0$  and primary consequences:**

$$\underbrace{E_{\text{total}} = E_{\text{space}} + E_{\text{locked}}}_{\text{Axiom } P_0}$$

$$\underbrace{\frac{\partial \epsilon}{\partial t} + \nabla \cdot (\epsilon \mathbf{v}) = 0}_{\text{Master conservation law (Gauss theorem applied to } P_0 \text{)}}$$

Master conservation law (Gauss theorem applied to  $P_0$ )

$$c = \frac{1}{\underbrace{\sqrt{\mu_0 \epsilon_0}}_{\text{Transverse wave speed (identifies } \mu_0, \epsilon_0 \text{ among the five constants)}}}$$

Transverse wave speed (identifies  $\mu_0, \epsilon_0$  among the five constants)

## Chapter 1

# The Physical Foundations of the Chemical Continuum

This chapter constructs the complete physical bedrock of the  $P_0$  framework. The derivation is strictly one-directional: each equation is the *unique* algebraic or analytic consequence of the preceding step and the declared inputs. Every empirical constant is named at its first use. Every step that is a declared correspondence rather than a deduction is labelled **[DC]**. Every step whose proof has a gap is labelled **[OG]** with a number.

**Declared empirical constants (all five).**

Symbol	SI unit	Value	Role in framework
$\epsilon_0$	$\text{F m}^{-1}$	$8.8542 \times 10^{-12}$	Vacuum permittivity; reinterpreted as the energy-density scale of the continuum via $u_E = \frac{1}{2}\epsilon_0 E^2$ <b>[DC1]</b>
$\mu_0$	$\text{H m}^{-1}$	$1.2566 \times 10^{-6}$	Vacuum permeability; reinterpreted as the shear modulus of the continuum <b>[DC2]</b>
$c$	$\text{m s}^{-1}$	$2.9979 \times 10^8$	Speed of light $= 1/\sqrt{\mu_0\epsilon_0}$ ; transverse wave speed of the continuum
$\nu$	$\text{m}^2 \text{s}^{-1}$	$\approx 2 \times 10^{-35}$	Kinematic viscosity of the <i>background</i> continuum (distinct from the electron vortex-core viscosity $\nu_{\text{core}} = \hbar/(2m_e) \approx 5.79 \times 10^{-5} \text{ m}^2 \text{s}^{-1}$ ; see §1.5.1 and [OG-0b]). <b>[v41 correction]:</b> The v40 claim “value chosen so that $4\pi\nu m_e = \hbar$ ” was erroneous for this $\nu_{\text{bg}}$ value: $4\pi \times (2 \times 10^{-35}) \times m_e = 2.3 \times 10^{-64} \text{ J s} \neq \hbar$ . The correct relation is $4\pi\nu_{\text{core}} m_e = \hbar$ (Planck’s constant), which holds for $\nu_{\text{core}} = \hbar/(2m_e)$ only. The value $\nu_{\text{bg}} \approx 2 \times 10^{-35} \text{ m}^2 \text{s}^{-1}$ is an order-of-magnitude estimate for the background medium and is not the viscosity entering the Madelung-to-Schrödinger derivation.
$\hbar$	$\text{J s}$	$1.0546 \times 10^{-34}$	Reduced Planck constant; enters the Madelung transformation as the action scale <b>[DC3]</b> ; post-hoc interpreted as $2m_e\nu$ <b>[OG-0]</b>

The effective mass density of the continuum is *defined by declared correspondence* as:

$$\rho_{\text{eff}} \stackrel{[\text{DC1-dim}]}{\equiv} \frac{\epsilon_0}{c^2} = \frac{8.854 \times 10^{-12}}{(2.998 \times 10^8)^2} = 9.85 \times 10^{-29} \text{ kg m}^{-3} \quad (1.1)$$

**[DC1-dim] — Dimensional correspondence.** In SI,  $\epsilon_0$  carries units  $\text{C}^2 \text{s}^2 (\text{kg m}^3)^{-1}$  (farads per metre), while  $c^2$  carries units  $\text{m}^2 \text{s}^{-2}$ . Consequently  $\epsilon_0/c^2$  has SI units  $\text{C}^2 \text{s}^4 (\text{kg m}^5)^{-1}$ , which is *not* equal to  $\text{kg m}^{-3}$  without suppressing the electromagnetic unit factor  $\text{C}^2 \text{s}^4 (\text{kg}^2 \text{m}^2)^{-1}$ . The identification of the numerical value  $9.85 \times 10^{-29}$  with a mass density is therefore a **declared correspondence** of the framework (**[DC1]**), not a dimensional identity. Any computation that uses  $\rho_{\text{eff}}$  as a mechanical mass density (as in Steps 4–8 below) carries this caveat implicitly.

**[C2 — v41-corr: Scope of [DC1-dim].]** Every equation in Steps 2–8 that contains  $\rho_{\text{eff}}$  inherits the dimensional caveat of **[DC1]**. In practice, all such equations are used in one of two ways that restore dimensional consistency: (i) as *ratios* — e.g.,  $P/\rho_{\text{eff}} = \alpha c^2$ , which is an energy-per-unit-mass relation, dimensionally consistent in SI; or (ii) combined with **[DC7]** ( $m_e = \rho_{\text{eff}} V_{\text{core}}$ ), which maps the continuum density to the electron mass. No equation in this framework equates a quantity carrying unresolved electromagnetic units directly with a purely

mechanical quantity without going through one of these two routes. The [DC1-dim] caveat applies to the *identification* of the numerical value  $9.85 \times 10^{-29}$  with a mass density; it does not invalidate the algebraic structure of the fluid-mechanical equations, which is that of standard continuum mechanics with a scalar density field.

## 1.1 Axiom $P_0$ : Energy Partition in Three-Dimensional Euclidean Space

**Manifold.** The universe is modelled as the unbounded, simply-connected manifold  $\mathcal{M} = \mathbb{R}^3$  with a global uniform time coordinate  $t \in \mathbb{R}$ . No extra dimensions and no spacetime curvature are assumed.

**Fields.** At every event  $(\mathbf{r}, t) \in \mathbb{R}^3 \times \mathbb{R}$  two  $C^1$  fields are defined:

- Energy-density scalar:  $\epsilon(\mathbf{r}, t) \geq 0$  [ $\text{J m}^{-3}$ ]
- Energy-flux velocity:  $\mathbf{v}(\mathbf{r}, t)$  [ $\text{m s}^{-1}$ ]

**[AXIOM  $P_0$ ].** For every material volume element  $dV$ , the total energy decomposes orthogonally into two non-negative parts:

$$\boxed{E_{\text{total}} = E_{\text{space}} + E_{\text{locked}}} \quad (1.2)$$

$E_{\text{space}} = \alpha \epsilon dV$  is the wave-borne (propagating) energy;  $\alpha \in [1/3, 2/3]$  is the kinematic fraction derived in §1.11.  $E_{\text{locked}}$  is energy trapped by internal topological constraints and invariant under volume change. Global conservation:  $\dot{E}_{\text{total}} = 0$ .

## 1.2 Step 1 — Master Conservation Law

**Derivation.** Fix an arbitrary control volume  $V$  with closed boundary  $\partial V$ . By Axiom  $P_0$  the energy inside  $V$  can change only through flux across  $\partial V$ :

$$\frac{d}{dt} \int_V \epsilon d^3r = - \oint_{\partial V} (\epsilon \mathbf{v}) \cdot d\mathbf{A} \quad (1.3)$$

Apply the Gauss Divergence Theorem to the right side:  $\oint_{\partial V} (\epsilon \mathbf{v}) \cdot d\mathbf{A} = \int_V \nabla \cdot (\epsilon \mathbf{v}) d^3r$ . Since  $V$  is arbitrary the integrand must vanish pointwise, giving the **master conservation law**:

$$\boxed{\frac{\partial \epsilon}{\partial t} + \nabla \cdot (\epsilon \mathbf{v}) = 0} \quad (1.4)$$

This is the only mathematical consequence of  $P_0$  and energy conservation; no dynamical assumption has been made yet.

## 1.3 Step 2 — Euler Equation: Inviscid Momentum Balance

**Derivation.** Consider a fluid parcel of the continuum with mass  $\delta m = \rho_{\text{eff}} dV$ . By Newton's second law, its acceleration equals the net pressure force per unit volume. The acoustic pressure is  $P = \alpha \epsilon$  (from Axiom  $P_0$ ,  $E_{\text{space}} = \alpha \epsilon dV$ , and the thermodynamic identity  $P = \partial E_{\text{space}} / \partial V = \alpha \epsilon$ ). In the inviscid limit (no viscous stress):

$$\rho_{\text{eff}} \frac{D\mathbf{v}}{Dt} = -\nabla P = -\nabla(\alpha \epsilon) \quad (1.5)$$

where  $D/Dt = \partial/\partial t + \mathbf{v} \cdot \nabla$  is the material derivative. Using the vector identity  $(\mathbf{v} \cdot \nabla)\mathbf{v} = \nabla(|\mathbf{v}|^2/2) - \mathbf{v} \times \boldsymbol{\omega}$  with vorticity  $\boldsymbol{\omega} = \nabla \times \mathbf{v}$ , the equivalent Lamb form is:

$$\frac{\partial \mathbf{v}}{\partial t} + \nabla \left( \frac{|\mathbf{v}|^2}{2} \right) - \mathbf{v} \times \boldsymbol{\omega} = -\frac{\nabla(\alpha \epsilon)}{\rho_{\text{eff}}} \quad (1.6)$$

**[Epistemic note: scope of  $P_{\text{locked}} = 0$ .]** Axiom  $P_0$  sets  $P_{\text{locked}} = 0$  for isolated topological solitons at densities where vortex cores do not overlap (the dilute regime). In this regime the locked component contributes no net momentum to a macroscopic boundary, and the acoustic pressure  $P = \alpha\epsilon$  is the complete pressure of the continuum. At extreme densities ( $\rho \gtrsim \rho_{\text{nuc}}$ , e.g. neutron-star interiors), adjacent vortex cores touch; the Korteweg gradient-energy term (Eq. (1.25)) generates a repulsive inter-vortex pressure that is *not* captured by  $P = \alpha\epsilon$ . For all chemical applications in this document (atomic and molecular scales,  $r \gg \bar{\lambda}_C$ ), the dilute-regime assumption is valid and  $P = \alpha\epsilon$  is the correct pressure.

## 1.4 Step 3 — Cauchy Momentum Equation: Elastic Stress

**Derivation.** The continuum has shear modulus  $\mu_0$  ([DC2]). For a linearly elastic isotropic medium the Cauchy stress tensor is:

$$\sigma_{ij} = -P\delta_{ij} + \mu_0 \left( \frac{\partial v_i}{\partial x_j} + \frac{\partial v_j}{\partial x_i} - \frac{2}{3}\delta_{ij}\nabla \cdot \mathbf{v} \right) + \lambda_0(\nabla \cdot \mathbf{v})\delta_{ij} \quad (1.7)$$

where  $\lambda_0$  is the second Lamé coefficient. Newton's second law applied to a volume element with the full stress tensor  $\nabla \cdot \boldsymbol{\sigma}$  gives the **Cauchy momentum equation**:

$$\rho_{\text{eff}} \frac{D\mathbf{v}}{Dt} = -\nabla P + \mu_0 \nabla^2 \mathbf{v} + \left( \frac{\mu_0}{3} + \lambda_0 \right) \nabla(\nabla \cdot \mathbf{v}) \quad (1.8)$$

## 1.5 Step 4 — Navier–Stokes Equation

**Derivation.** Define the kinematic viscosity  $\nu \equiv \mu_0/\rho_{\text{eff}}$  [ $\text{m}^2 \text{s}^{-1}$ ]. Inside a closed vortex core the flow is topologically solenoidal:  $\nabla \cdot \mathbf{v} = 0$  (Helmholtz vortex theorem applied to the incompressible core region). Substituting into Eq. (1.8) with  $\nabla \cdot \mathbf{v} = 0$ :

$$\boxed{\frac{\partial \mathbf{v}}{\partial t} + (\mathbf{v} \cdot \nabla) \mathbf{v} = -\frac{\nabla P}{\rho_{\text{eff}}} + \nu \nabla^2 \mathbf{v}} \quad (1.9)$$

together with  $\nabla \cdot \mathbf{v} = 0$  inside vortex cores.

**Derivation chain (no circularity):**

$$P_0 \xrightarrow{\text{Gauss}} \text{continuity (1.4)} \xrightarrow{\text{Newton 2}} \text{Euler (1.5)} \xrightarrow{\text{Cauchy stress, } \nu} \text{N-S (1.9)}$$

No quantum input has entered.

### 1.5.1 Burgers Vortex: Exact N-S Solution

The N-S equation (1.9) with  $\nabla \cdot \mathbf{v} = 0$  admits an exact analytical steady-state solution for an axisymmetric vortex subject to an external axial strain rate  $\alpha_s$  [ $\text{s}^{-1}$ ]: the **Burgers vortex**. In cylindrical coordinates  $(r, \theta, z)$ , with  $v_z = \alpha_s z$  and  $v_r = -\alpha_s r/2$ , the azimuthal component is:

$$v_\theta(r) = \frac{\Gamma}{2\pi r} \left( 1 - e^{-\alpha_s r^2/(2\nu)} \right) \quad (1.10)$$

**Verification:** substitute Eq. (1.10) into the  $\theta$ -component of N-S with  $v_r = -\alpha_s r/2$ ,  $v_z = \alpha_s z$ ; direct computation confirms both the N-S and continuity equations are satisfied identically for any  $\Gamma$  and  $\alpha_s > 0$ .

The vortex core radius is  $a = \sqrt{2\nu/\alpha_s}$ . The circulation  $\Gamma = \oint_C \mathbf{v} \cdot d\mathbf{l}$  is conserved for any closed contour enclosing the core. The core Reynolds number is  $\text{Re}_{\text{core}} = \Gamma/(2\nu)$ .

**[OG-0] — Minimum stable circulation.** The Burgers vortex exists as an exact steady N-S solution for *any*  $\Gamma > 0$ . A lower bound  $\Gamma_{\text{min}} = 4\pi\nu$  is *postulated* by identifying the stability

threshold with  $\text{Re}_{\text{core}} = 2\pi$ ; this criterion is not derived from the N-S equation within this framework but is assumed as a stability postulate:

$$\Gamma_{\min} \equiv 4\pi\nu \equiv \kappa_0 \quad \text{[postulated stability threshold]} \quad (1.11)$$

**[OG-0b] — Identification of  $\hbar$ .** The combination  $m_e\kappa_0 = 4\pi m_e\nu$  has dimensions of action. The framework *defines*:

$$h_{P_0} \equiv m_e\kappa_0 = 4\pi m_e\nu \quad (1.12)$$

and then *identifies*  $h_{P_0} \equiv h$  (Planck’s constant) by the requirement that the resulting acoustic Schrödinger equation reproduces the observed hydrogen spectrum. This is a declared correspondence ([DC3]), not a derivation:  $\nu$  is fixed post-hoc by  $\nu = h/(4\pi m_e) = \hbar/(2m_e) \approx 5.79 \times 10^{-5} \text{ m}^2 \text{ s}^{-1}$  — *not* the  $\sim 10^{-35} \text{ m}^2 \text{ s}^{-1}$  value stated in the constants table.

**Resolution:** The value  $\nu \approx 2 \times 10^{-35} \text{ m}^2 \text{ s}^{-1}$  quoted in the constants table corresponds to the kinematic viscosity of the *background* continuum, while  $\hbar/(2m_e)$  is the kinematic viscosity of the *electron vortex core*. These are distinct quantities; the identification uses the core viscosity. Both are declared empirical inputs; neither is derived from  $P_0$  alone.

**[OPEN GAP OG-0b] — Two-phase viscosity inconsistency.** The background viscosity  $\nu_{\text{bg}} \approx 2 \times 10^{-35} \text{ m}^2 \text{ s}^{-1}$  and the vortex-core viscosity  $\nu_{\text{core}} = \hbar/(2m_e) \approx 5.79 \times 10^{-5} \text{ m}^2 \text{ s}^{-1}$  differ by approximately **30 orders of magnitude**. The Navier–Stokes equation (1.9) as written in Step 4 is a *single-phase* equation with a single scalar kinematic viscosity  $\nu$ . A continuum that simultaneously requires two viscosities differing by  $10^{30}$  cannot be correctly described by a single-phase N-S equation without: (i) modelling the system as a two-phase fluid with an interface boundary condition and viscosity-jump tensor at the vortex-core boundary, and (ii) deriving the core-boundary conditions from first principles. Until this two-phase structure is formalised, Step 4 and the Burgers vortex solution of §1.5.1 apply only to one regime at a time (either background or core), not simultaneously. This is a genuine structural gap that must be resolved before the framework can claim a self-consistent single-fluid foundation.

**[C5 — v41-corr: Concrete consequence of OG-0b.]** Steps 4 (N-S equation), 5 (Helmholtz decomposition), and 6 (Madelung transformation) each use a *single* kinematic viscosity  $\nu$ . Any equation in these steps that involves  $\nu$  explicitly—such as the Burgers vortex core radius  $a = \sqrt{2\nu/\alpha_s}$  or the minimum circulation  $\Gamma_{\min} = 4\pi\nu$ —is valid only in one regime at a time. For all chemical applications in this document (Chapters 2–37), the operative value is  $\nu = \nu_{\text{core}} = \hbar/(2m_e)$ ; the background value  $\nu_{\text{bg}} \approx 2 \times 10^{-35} \text{ m}^2 \text{ s}^{-1}$  applies only to the inter-vortex vacuum continuum. This choice is physically consistent: electron–nucleus interactions and covalent bonds occur at the length scale of vortex cores, where  $\nu_{\text{core}}$  governs the dynamics. The inconsistency flagged by OG-0b arises at the level of the *global* fluid description, not at the level of individual chemical applications, which uniformly use  $\nu_{\text{core}}$ .

**[C3 — v41-corr: Definitive statement on  $\hbar$ .]**  $\hbar = 1.0546 \times 10^{-34} \text{ Js}$  enters *all* subsequent chapters as the fifth empirical constant, declared in §1.1. It is *not* derived from the background kinematic viscosity  $\nu_{\text{bg}} \approx 2 \times 10^{-35} \text{ m}^2 \text{ s}^{-1}$ , nor from the vortex-core viscosity  $\nu_{\text{core}} = \hbar/(2m_e) \approx 5.79 \times 10^{-5} \text{ m}^2 \text{ s}^{-1}$ . The relation  $h_{P_0} = 4\pi m_e\nu$  (Eq. (1.12)) is a dimensional observation:  $m_e\kappa_0$  has units of action. The identification  $h_{P_0} \equiv h$  is made post-hoc by requiring consistency with the hydrogen spectrum and constitutes a declared correspondence [DC3], not a first-principles derivation. As a consequence, the claim that the  $P_0$  framework “reconstructs quantum mechanics from classical fluid mechanics” should be read as: *the mathematical structure* of quantum mechanics (the Schrödinger equation, Coulomb’s law, Pauli exclusion) is reproduced by the framework given five empirical constants, two topological postulates, and the open gaps listed in §1.14. The framework does *not* reduce the number of independent empirical inputs below five.



### 1.5.2 Kelvin's Circulation Theorem and Vortex Stability

For an ideal (inviscid) continuum, taking the material derivative of  $\Gamma(t) = \oint_{C(t)} \mathbf{v} \cdot d\mathbf{l}$  and applying the Euler equation (1.5) gives:

$$\frac{d\Gamma}{dt} = \oint_{C(t)} \frac{D\mathbf{v}}{Dt} \cdot d\mathbf{l} = - \oint_{C(t)} \frac{\nabla P}{\rho_{\text{eff}}} \cdot d\mathbf{l} = 0 \quad (1.13)$$

The last equality holds because  $P/\rho_{\text{eff}} = \alpha c^2$  is a function of state, making  $\oint \nabla(P/\rho_{\text{eff}}) \cdot d\mathbf{l} = 0$  for any closed curve. Consequences:

1. By  $\nabla \cdot \boldsymbol{\omega} = 0$  (Helmholtz), vortex lines cannot terminate inside the fluid; in  $\mathbb{R}^3$  without boundaries, stable vortex structures must be closed loops.
2. In the viscous case, a closed vortex loop persists provided  $\text{Re}_{\text{core}} \geq 2\pi$ , i.e.,  $\Gamma \geq \kappa_0$  (from postulate Eq. (1.11)).

## 1.6 Step 5 — Helmholtz Decomposition and Topological Particle Classification

**Derivation.** The Helmholtz decomposition theorem (proved for any  $C^1$  vector field on  $\mathbb{R}^3$  vanishing at infinity) gives:

$$\mathbf{v} = -\nabla\Phi + \nabla \times \mathbf{A} \quad (1.14)$$

The irrotational part  $-\nabla\Phi$  (curl-free) propagates as waves, carrying  $E_{\text{space}}$ . The solenoidal part  $\nabla \times \mathbf{A}$  (divergence-free identically) carries  $E_{\text{locked}}$ . By Kelvin's theorem, solenoidal structures that are closed loops are topologically stable.

**[DC4] — Topological Postulate T1: Electric Charge.** Electric charge is declared to be the topological winding number  $q$  of a vortex, scaled by the elementary charge  $e$  ( $e = 1.602 \times 10^{-19}$  C, empirical). Two stable matter attractors are identified by Taylor–Moffatt helicity relaxation of the viscous N-S equation:

- The unknot (trivial knot, Hopf index  $n_H = 0$ ): identified with the **electron**, winding number  $q = -1$ , mass  $m_e = 9.109 \times 10^{-31}$  kg (empirical).
- The (3,2) torus knot (trefoil, minimal crossing number 3,  $n_H = 1$ ): identified with the **proton**, winding number  $q = +1$ , mass  $m_p = 1.673 \times 10^{-27}$  kg (empirical).

This identification is a **declared correspondence**; the claim that exactly these two knot types are the only stable N-S attractors is supported by Taylor relaxation and Crow instability arguments, but has not been rigorously proved within this framework.

## 1.7 Step 6 — Madelung Transformation: N-S to NLSE

**Setup.** Define the complex amplitude field:

$$\Phi(\mathbf{r}, t) = \sqrt{\frac{\epsilon(\mathbf{r}, t)}{\epsilon_0}} e^{iS(\mathbf{r}, t)/\hbar} \quad (1.15)$$

Here  $\hbar$  is the fifth empirical constant declared in §1.1;  $S$  is Hamilton's principal function [ $S$ ] = Js = kg m<sup>2</sup>s<sup>-1</sup>.

**[DC8] — Velocity definition.** The standard Madelung transformation of the quantum probability-density equation uses  $\mathbf{v} = \nabla S/m_e$  (gradient of action divided by the *particle mass*  $m_e$  [kg]), which has dimensions [ $\nabla S/m_e$ ] = m s<sup>-1</sup> ✓. The  $P_0$  framework instead writes:

$$\mathbf{v} = \frac{\nabla S}{\rho_{\text{eff}}} \quad (1.16)$$

where  $\rho_{\text{eff}}$  [kg m<sup>-3</sup>] is the continuum mass density. This gives  $[\nabla S/\rho_{\text{eff}}] = \text{m}^4\text{s}^{-1}$ , which is *not* a velocity in SI dimensions. The substitution is valid only in the sense of a **declared correspondence** ([DC8]): inside the electron vortex core of volume  $V_{\text{core}} = 2\pi^2 a^3$ , the core mass satisfies  $m_e \stackrel{[\text{DC7}]}{=} \rho_{\text{eff}} V_{\text{core}}$ , so one can formally write  $\rho_{\text{eff}} = m_e/V_{\text{core}}$ ; the replacement  $m_e \rightarrow \rho_{\text{eff}}$  in the velocity definition amounts to absorbing the volume factor into the definition of  $S$ . All subsequent equations that follow from (1.16) inherit this caveat.

**Imaginary part (continuity).** Substituting into the continuity equation (1.4) with  $|\Phi|^2 = \epsilon/\epsilon_0$ :

$$\frac{\partial |\Phi|^2}{\partial t} + \nabla \cdot \left( |\Phi|^2 \frac{\nabla S}{\rho_{\text{eff}}} \right) = 0 \quad (1.17)$$

This is identically satisfied by construction.

**Real part (Euler without viscosity).**

**[C1 — v41-corr: DC8 denominator correction.]** The continuum velocity field is  $\mathbf{v} = \nabla S/\rho_{\text{eff}}$  (Eq. (1.16), [DC8]). Inside the electron vortex core, [DC7] gives  $m_e = \rho_{\text{eff}} V_{\text{core}}$ , so  $\rho_{\text{eff}} = m_e/V_{\text{core}}$ . Substituting:

$$\mathbf{v}_{\text{continuum}} = \frac{\nabla S}{\rho_{\text{eff}}} = \frac{V_{\text{core}} \nabla S}{m_e} \equiv V_{\text{core}} \cdot \mathbf{v}_{\text{Madelung}}, \quad \mathbf{v}_{\text{Madelung}} \equiv \frac{\nabla S}{m_e} \quad (1.18)$$

All subsequent equations use the *particle* convention  $\mathbf{v} = \nabla S/m_e$  (which carries dimensions  $[\nabla S/m_e] = \text{m s}^{-1}$  ✓). The continuum convention absorbs the factor  $V_{\text{core}}$  into the normalisation of  $S$ ; this is a valid redefinition inside the vortex core under [DC7]. [DC8] is therefore a *continuum-level* correspondence only; the NLSE derivation that follows uses the particle convention and is dimensionally exact.

Substituting  $\mathbf{v} = \nabla S/m_e$  into the Euler equation (1.5) and writing  $S = \hbar\theta$ :

$$\frac{\partial S}{\partial t} + \frac{(\nabla S)^2}{2m_e} + V(\mathbf{r}) + Q = 0 \quad (1.19)$$

where  $V(\mathbf{r})$  is the Coulomb potential of the nucleus and  $Q$  is the **Bohm quantum pressure**:

$$Q = -\frac{\hbar^2}{2m_e} \frac{\nabla^2 |\Phi|}{|\Phi|} \quad (1.20)$$

$Q$  is not a postulate; it arises algebraically from the Madelung substitution applied to the gradient kinetic-energy term.

**Recombination to complex PDE.** Multiply Eq. (1.17) by  $i\hbar$ , multiply Eq. (1.19) by  $|\Phi|$ , and add, using the algebraic identity

$$\frac{\partial(\sqrt{\rho} e^{i\theta})}{\partial t} = e^{i\theta} \left( \frac{\dot{\rho}}{2\sqrt{\rho}} + i\sqrt{\rho}\dot{\theta} \right)$$

to obtain:

$$i\hbar \frac{\partial \Phi}{\partial t} = -\frac{\hbar^2}{2m_e} \nabla^2 \Phi + V(\mathbf{r})\Phi + g_3 |\Phi|^2 \Phi \quad (1.21)$$

The linear terms follow exactly. The nonlinear term  $g_3 |\Phi|^2 \Phi$  arises from the pressure  $P = \alpha\epsilon$  entering Eq. (1.19). In the non-relativistic vortex core  $\alpha \rightarrow 2/3$  (from §1.11), so  $P = (2/3)\epsilon_0 |\Phi|^2$ ; this contributes to the real part (1.19) a term  $(2/3)\epsilon_0 |\Phi|^2/\rho_{\text{eff}} = (2/3)c^2 |\Phi|^2$ , giving:

$$g_3 = \frac{2}{3} \frac{\epsilon_0 c^2}{\rho_{\text{eff}}} = \frac{2}{3} c^2 \cdot \frac{\epsilon_0}{\rho_{\text{eff}}} = \frac{2}{3} c^4 \quad (1.22)$$

**[OG-1] — Quintic stabilisation term.** For a localised ( $L^2$ ) soliton in  $\mathbb{R}^3$ , Derrick's theorem (1964) proves that a purely cubic NLSE has no stable localised solution: any such solution either spreads or collapses under rescaling. A quintic term  $-\gamma|\Phi|^4\Phi$  with  $\gamma > 0$  is required for stability. Derrick's virial identity for the full cubic-quintic NLSE reads  $2E_{\text{kin}} = 3(E_{\text{quint}} - E_{\text{cub}})$ , where  $E_{\text{kin}} = \frac{\hbar^2}{2m_e} \int |\nabla\Phi|^2 d^3r$ ,  $E_{\text{cub}} = \frac{g_3}{2} \int |\Phi|^4 d^3r$ , and  $E_{\text{quint}} = \frac{\gamma}{3} \int |\Phi|^6 d^3r$ . This constrains  $\gamma$  in terms of the soliton profile but does *not* uniquely determine  $\gamma$  without knowing the profile. The value of  $\gamma$  is therefore a **model parameter** fixed by a Gaussian-ansatz approximation ([OG-1]):

$$\gamma \approx \frac{g_3^2}{3m_e c^2} \quad \text{[Gaussian-ansatz approximation]} \quad (1.23)$$

The complete NLSE with both terms:

$$\boxed{i\hbar \frac{\partial \Phi}{\partial t} = -\frac{\hbar^2}{2m_e} \nabla^2 \Phi + V(\mathbf{r})\Phi + g_3|\Phi|^2\Phi - \gamma|\Phi|^4\Phi} \quad (1.24)$$

**Variational origin of the kinetic term (Korteweg gradient energy).** The kinetic term  $-(\hbar^2/2m_e)\nabla^2\Phi$  in Eq. (1.24) has a precise variational origin in the  $P_0$  energy functional. With amplitude  $R \equiv \sqrt{\epsilon}$ , the locked elastic strain energy from density gradients is:

$$E_{\text{locked}} \supset \int \kappa_0 (\nabla R)^2 d^3r = \int \kappa_0 (\nabla \sqrt{\epsilon})^2 d^3r, \quad \kappa_0 > 0 \quad (1.25)$$

**Critical note:** The gradient penalty must be  $(\nabla \sqrt{\epsilon})^2$  (*gradient of amplitude*), not  $(\nabla \epsilon)^2$  (*gradient of density*). These differ:  $(\nabla \sqrt{\epsilon})^2 = (\nabla R)^2$ , while  $(\nabla \epsilon)^2 = 4R^2(\nabla R)^2$ . Only the former yields the correct Euler-Lagrange equation:

$$\frac{\delta E}{\delta R} = 2\alpha_{\text{kin}}R - 2\kappa_0 \nabla^2 R = 0 \xrightarrow{\psi = Re^{i\theta}} -2\kappa_0 \nabla^2 \psi + \alpha\psi - g|\psi|^2\psi = 0 \quad (1.26)$$

Comparing with the NLSE kinetic term gives:

$$2\kappa_0 = \frac{\hbar^2}{2m_e} \implies \kappa_0 = \frac{\hbar^2}{4m_e} \quad (1.27)$$

This is the Korteweg capillarity coefficient of the  $P_0$  medium, expressed in terms of the empirical constants  $\hbar$  and  $m_e$ . **[DERIVED from Po variational principle, given  $\hbar$  and  $m_e$  as inputs.]**

The quantisation condition on the phase integral is not an additional postulate; it follows from classical vortex fluid mechanics:

*Step 1: Irrotational flow and multi-valued velocity potential.* Outside the vortex core the flow is irrotational, so the velocity can be written as a gradient:  $\mathbf{v} = (\kappa_0/2\pi)\nabla S$ , where  $S$  is a dimensionless phase field (Eq. (1.16) with  $\rho_{\text{eff}}$  absorbed into the definition of  $S$ ). For a vortex flow, the velocity potential  $\phi \propto S$  is *multi-valued*: it increases by  $\kappa_0$  every time a closed loop encircles the vortex core (Kelvin circulation theorem, §1.5.2, with  $\Gamma = \kappa_0$  for the minimum stable vortex).

*Step 2: Single-valuedness forces integer quantisation.* The physical velocity  $\mathbf{v}$  must be single-valued (it is an observable). Since  $\mathbf{v} \propto \nabla S$ , the field  $S$  may increase by any integer multiple of  $2\pi$  around a closed loop without changing  $\mathbf{v}$ . Therefore  $S$  maps to the circle  $S^1 = \mathbb{R}/(2\pi\mathbb{Z})$ , and the fundamental group  $\pi_1(S^1) = \mathbb{Z}$  guarantees:

$$\oint_C \nabla S \cdot d\mathbf{l} = 2\pi n, \quad n \in \mathbb{Z} \quad (1.28)$$

This is a **theorem of classical ideal-fluid vortex mechanics**, not an additional postulate: it follows from the Kelvin circulation theorem (§1.5.2) and the requirement that  $\mathbf{v}$  be single-valued.

*Step 3: Restoration of dimensions.* In the Madelung representation with  $S$  having dimensions of action [J·s], the phase enters as  $S/\hbar$  (dimensionless); the boundary condition becomes:

$$\oint_C \nabla S \cdot d\mathbf{l} = 2\pi n\hbar, \quad n \in \mathbb{Z} \quad (1.29)$$

The integer  $n$  is the topological winding number, a conserved classical topological invariant of the vortex flow. **[DERIVED from classical fluid mechanics.]**

**[OG-2] — Particle mass eigenvalues.** The NLSE (1.24) with boundary conditions (1.29) constitutes an eigenvalue problem whose solutions give the locked energies (rest masses) of the particles. The numerical solution of this eigenvalue problem for  $n = 0$  (electron) and  $n = 1$  (proton) has not been carried out within this framework. The mass ratio  $m_p/m_e = 1836.15$  has not been derived.

### 1.7.1 Linearisation: Acoustic Schrödinger Equation

In the Coulomb well  $V(r) = -Ze^2/(4\pi\epsilon_0 r)$ , the acoustic density perturbation  $\psi(\mathbf{r})$  around the background  $|\Phi_0|^2 = \text{const}$  satisfies  $|\psi| \ll |\Phi_0|$ . In this limit  $|\Phi|^2 \approx |\Phi_0|^2$ ; the cubic and quintic terms become constant energy offsets renormalising the energy zero; the NLSE reduces exactly to:

$$\left[ -\frac{\hbar^2}{2m_e} \nabla^2 + V(\mathbf{r}) \right] \psi(\mathbf{r}) = E\psi(\mathbf{r}) \quad (1.30)$$

This is the time-independent Schrödinger equation, here interpreted as the acoustic standing-wave condition in the Coulomb well. All results of non-relativistic quantum chemistry that follow from Eq. (1.30) are reproduced within this framework.

## 1.8 Step 7 — Coulomb's Law from the Laplace Equation

**Derivation.** An isolated vortex of winding number  $q$  in the background continuum generates a static shear-stress potential  $\phi(\mathbf{r})$  [V] satisfying, in the source-free exterior region:

$$\nabla^2 \phi = 0 \quad (1.31)$$

**[DC5] — Identification of  $\phi$  with the electric potential.** The shear-stress field  $\phi$  is identified with the electrostatic potential. This is a declared correspondence; it is not derivable from the Laplace equation alone.

**Sourced Gauss law — distributional treatment.** At the vortex core (a singular point or curve in the field  $\phi$ ), the field is not  $C^2$ , so Eq. (1.31) does not hold in the classical sense. The correct treatment uses distributional (Schwartz) field theory: decompose  $\phi = \phi_{\text{reg}} + \phi_{\text{sing}}$ , where  $\phi_{\text{reg}}$  satisfies the Laplace equation in the smooth exterior and  $\phi_{\text{sing}}$  carries the vortex-core singularity. By the Gauss divergence theorem applied to a small ball  $B_\varepsilon(\mathbf{r}_0)$  of radius  $\varepsilon \rightarrow 0$  enclosing the core at  $\mathbf{r}_0$ :

$$\lim_{\varepsilon \rightarrow 0} \int_{B_\varepsilon} \nabla^2 \phi \, d^3r = \oint_{\partial B_\varepsilon} (-\nabla \phi) \cdot d\mathbf{A} = \frac{qe}{\epsilon_0} \quad (1.32)$$

In the distributional (point-source) limit this gives:

$$\nabla^2 \phi = -\frac{qe}{\epsilon_0} \delta^{(3)}(\mathbf{r} - \mathbf{r}_0) \quad (1.33)$$

The unique solution of Eq. (1.33) in  $\mathbb{R}^3$  decaying at infinity is:

$$\phi(\mathbf{r}) = \frac{qe}{4\pi\epsilon_0 |\mathbf{r} - \mathbf{r}_0|} \quad (1.34)$$

A second vortex of winding number  $q'$  placed at position  $\mathbf{r}$  in this field experiences:

$$\mathbf{F} = q'e(-\nabla\phi) = \frac{qq'e^2}{4\pi\epsilon_0 r^2} \hat{\mathbf{r}} \quad (1.35)$$

The  $1/r^2$  dependence is a parameter-free consequence of the distributional Laplace equation in  $\mathbb{R}^3$ . The integer quantisation of  $q$  follows from the winding-number topology ( $\pi_1(U(1)) = \mathbb{Z}$ , derived in Step 6). The prefactor uses the empirical constants  $e$  and  $\epsilon_0$ . **[DERIVED, given [DC5].]**

## 1.9 Step 8 — Electron Spin: Horn-Torus Integration

**[DC6] — Topological Postulate T2.** The ground-state electron vortex is declared to adopt the horn-torus geometry: tube-core radius  $a$  equals major radius  $R$  (i.e.,  $a = R$ ). The acoustic energy of a torus is  $E_{\text{torus}} = \pi^2 \mu_0 a^2 R [1 + O(a^2/R^2)]$ ; at fixed locked mass  $m_e$ , the ratio  $E_{\text{shear}}/m_e$  is minimised at  $a = R$  within the class of tori, consistent with T2. This postulate is **[DC6]**.

**Circulation quantisation.** Single-valuedness of phase around the vortex core ( $\oint \nabla S \cdot d\mathbf{l} = 2\pi\hbar$ ) gives:

$$\Gamma = \frac{2\pi\hbar}{m_e} \quad (1.36)$$

**Angular momentum derivation.** The total angular momentum of the horn-torus vortex about its symmetry axis is:

$$\mathbf{L} = \int \rho_{\text{eff}}(\mathbf{r} \times \mathbf{v}) d^3r \quad (1.37)$$

**[OG-3] — Axis alignment.** The tube-azimuthal velocity  $v_\phi(r') = \Gamma r'/(2\pi a^2)$  (solid-body core rotation) is the flow around the tube axis  $\hat{\phi}_{\text{tube}}$ . The  $\hat{z}$ -component of  $\mathbf{r} \times \mathbf{v}$  for this flow involves the projection of the tube angular momentum onto the torus symmetry axis. For a planar vortex ring these axes are parallel; for a horn-torus in 3D the alignment must be verified. We proceed with the planar approximation (**[OG-3]**).

In toroidal coordinates with major radius  $R = a$  and minor radius  $r' \in [0, a]$ , using the tube-azimuthal angular-momentum approximation (**[OG-3]**):

$$\begin{aligned} L_z &= \underbrace{\int_0^{2\pi} d\varphi}_{=2\pi} \underbrace{\int_0^{2\pi} d\phi (R + r' \cos \phi)}_{=2\pi R} \int_0^a \rho_{\text{eff}} v_\phi(r') r'^2 dr' \\ &= 4\pi^2 R \rho_{\text{eff}} \int_0^a \frac{\Gamma r'^3}{2\pi a^2} dr' \\ &= 4\pi^2 R \rho_{\text{eff}} \cdot \frac{\Gamma}{2\pi a^2} \cdot \frac{a^4}{4} = \frac{\pi}{2} \rho_{\text{eff}} \Gamma R a^2 \end{aligned} \quad (1.38)$$

(The  $\cos \phi$  term in  $(R + r' \cos \phi)$  integrates to zero over  $\phi \in [0, 2\pi]$ , correctly giving only the  $2\pi R$  contribution. The two factors of  $r'$  in the integrand are: one from the angular-momentum lever arm about the tube axis, one from the polar-coordinate Jacobian  $r' dr'$ .)

**Verification of intermediate coefficient.** Step-by-step:

$$4\pi^2 R \rho_{\text{eff}} \cdot \frac{\Gamma}{2\pi a^2} \cdot \frac{a^4}{4} = \frac{4\pi^2 \cdot \Gamma \cdot a^2 \cdot R \rho_{\text{eff}}}{8\pi} = \frac{\pi \Gamma R a^2 \rho_{\text{eff}}}{2}$$

In the horn-torus limit  $a = R$ :  $L_z = \frac{\pi}{2} \rho_{\text{eff}} \Gamma a^3$ .

In the horn-torus limit  $a = R$ :  $L_z = \frac{\pi}{2}\rho_{\text{eff}}\Gamma a^3$ .

**Horn-torus mass.** Volume of horn-torus at  $a = R$ :  $V_{\text{horn}} = (2\pi R)(\pi a^2)|_{a=R} = 2\pi^2 a^3$ . Using [DC7]:  $\rho_{\text{eff}} = \epsilon_0/c^2$  is declared to be the mass density of the vortex core:

$$m_e \stackrel{[\text{DC7}]}{=} \rho_{\text{eff}} \cdot 2\pi^2 a^3 \implies \rho_{\text{eff}} a^3 = \frac{m_e}{2\pi^2} \quad (1.39)$$

This is a declared correspondence;  $\rho_{\text{eff}}$  is a vacuum parameter whose identification with the electron core density is non-trivial (see [OG-3]).

Substituting Eqs. (1.36) and (1.39) into  $L_z = \frac{\pi}{2}\rho_{\text{eff}}\Gamma a^3$ :

$$|L_z| = \frac{\pi}{2} \rho_{\text{eff}} \cdot \frac{2\pi\hbar}{m_e} \cdot a^3 = \frac{\pi}{2} \cdot \frac{m_e}{2\pi^2} \cdot \frac{2\pi\hbar}{m_e} = \frac{\pi}{2} \cdot \frac{2\pi}{2\pi^2} \cdot \hbar = \frac{\pi}{2} \cdot \frac{1}{\pi} \cdot \hbar = \frac{\hbar}{2} \quad (1.40)$$

**Step-by-step verification:**  $\frac{\pi}{2} \cdot \frac{1}{2\pi^2} \cdot 2\pi = \frac{\pi \cdot 2\pi}{2 \cdot 2\pi^2} = \frac{2\pi^2}{4\pi^2} = \frac{1}{2} \checkmark$

Subject to the caveats [DC6], [DC7], and [OG-3], spin  $\hbar/2$  follows geometrically.

## 1.10 Step 9 — Pauli Exclusion from $\pi_1(SO(3))$

**Step 9a: Phase reversal under  $2\pi$  rotation.** The vortex amplitude field  $\Psi$  maps  $\mathbb{R}^3$  into  $SU(2)$  (the universal cover of  $SO(3)$ , with  $\pi_1(SO(3)) = \mathbb{Z}_2$ ). A continuous rotation of  $2\pi$  traces the non-contractible loop in  $SO(3)$ ; in  $SU(2)$  this connects  $I$  to  $-I$ . Therefore:

$$\Psi(\mathbf{r} \text{ rotated by } 2\pi) = -\Psi(\mathbf{r}) \quad (1.41)$$

**Step 9b: Antisymmetry under exchange. [OG-4] — Spin-statistics step.** In  $\mathbb{R}^3$ , the configuration space of two identical particles has  $\pi_1 = \mathbb{Z}_2$ , so two classes of statistics are possible: symmetric and antisymmetric. The assignment of half-integer-spin particles to the antisymmetric class is the content of the **spin-statistics theorem**, whose proof requires relativistic quantum field theory (Pauli 1940; Lüders–Zumino 1958). This theorem is *invoked* here as an established mathematical result:

$$\Psi(\dots, \mathbf{r}_1, \dots, \mathbf{r}_2, \dots) = -\Psi(\dots, \mathbf{r}_2, \dots, \mathbf{r}_1, \dots) \quad (1.42)$$

**Step 9c: Pauli exclusion.** Setting  $\mathbf{r}_1 = \mathbf{r}_2 = \mathbf{r}$  in Eq. (1.42):  $\Psi(\mathbf{r}, \mathbf{r}) = -\Psi(\mathbf{r}, \mathbf{r})$ , so  $\Psi(\mathbf{r}, \mathbf{r}) = 0$ . Two identical electron vortices cannot occupy the same state.

## 1.11 Step 10 — Kinematic Energy Fraction $\alpha(s)$

**Derivation.** For a single continuum element with reduced momentum  $s = p/(m_{\text{eff}}c)$  and Lorentz factor  $\gamma_L = (1 + s^2)^{1/2}$ :

- Total energy:  $E = \gamma_L m_{\text{eff}} c^2$
- Velocity:  $v = sc/(1 + s^2)^{1/2}$
- Kinetic pressure contribution:  $pv/3$  (isotropic ideal gas in 3D)

The spatial energy fraction for a *monoenergetic* beam is:

$$\alpha(s) = \frac{pv/3}{E} = \frac{s^2/(3\sqrt{1+s^2})}{\sqrt{1+s^2}} = \frac{s^2}{3(1+s^2)} \quad (1.43)$$

This gives  $\alpha(0) = 0$  (non-relativistic rest: all energy locked) and  $\alpha(\infty) = 1/3$  (ultra-relativistic: radiation pressure).

However, for the energy continuum the relevant quantity is the *total* spatial fraction including both propagating kinetic energy and a thermal baseline. In the non-relativistic limit a monatomic ideal gas satisfies  $\langle pv \rangle / (3E_{\text{tot}}) = 2/3$  when  $E_{\text{tot}}$  counts only kinetic energy, or  $2E_{\text{kin}} / (3E_{\text{kin}}) = 2/3$ . Including the rest-mass energy in the denominator shifts the intercept. The interpolating formula that satisfies  $\alpha(0) = 2/3$  (non-relativistic continuum) and  $\alpha(\infty) = 1/3$  (radiation) and is monotone on  $[0, \infty)$  with a single rational form is:

$$\alpha(s) = \frac{2 + s^2}{3(1 + s^2)}, \quad \alpha \in [1/3, 2/3] \quad (1.44)$$

**Verification of limits:**  $\lim_{s \rightarrow 0} \alpha(s) = 2/3 \checkmark$ ;  $\lim_{s \rightarrow \infty} \alpha(s) = 1/3 \checkmark$ .

**[OG-5] — Interpolation.** Eq. (1.44) is the unique rational function of the form  $(a + bs^2)/(c + ds^2)$  that matches both limits exactly. **Uniqueness argument (complete):** A rational function with finite limits at both  $s = 0$  and  $s \rightarrow \infty$  must have equal degree in numerator and denominator; the minimal such form is  $(a + bs^2)/(c + ds^2)$  with four parameters. Condition 1:  $\alpha(0) = a/c = 2/3$ , i.e.  $a = 2c/3$ . Condition 2:  $\alpha(\infty) = b/d = 1/3$ , i.e.  $b = d/3$ . Condition 3 (normalisation): choose  $c = d$  (i.e. normalise the denominator so that its leading and constant coefficients are equal; this is the unique normalisation that makes the denominator  $(c + cs^2) = c(1 + s^2)$ , i.e. a simple Lorentzian form). Substituting: numerator  $= a + bs^2 = (2c/3) + (c/3)s^2 = c(2 + s^2)/3$ ; denominator  $= c(1 + s^2)$ ; hence  $\alpha(s) = (2 + s^2)/(3(1 + s^2))$  uniquely given the normalisation convention  $c = d$ . *Caveat:* A different normalisation convention (e.g.  $a = b$ ) would yield a distinct functional form satisfying the same two limits; the uniqueness claim therefore relies on the Lorentzian-denominator normalisation, which is physically motivated (isotropic pressure tensor in 3D) but not uniquely forced by the limits alone. For a genuine thermal distribution (Maxwell–Jüttner), Eq. (1.44) is the zero-temperature ( $T \rightarrow 0$ ) limit; finite-temperature corrections are  $O(k_B T / m_e c^2)$  and are neglected.

## 1.12 FP-New: Dual Computational Philosophy

Two computational strategies are available:

**Track 1 (Exact).** Solve the NLSE (1.24) directly. Scales as  $\mathcal{O}(N^3)$  or worse.

**Track 2 (FP-New Effective Field Theory).** Pre-tabulate the acoustic impedance, stiffness, and yield integrals of specific vortex topologies. During simulation evaluate only macroscopic acoustic superpositions. Scales as  $\mathcal{O}(N \log N)$  via acoustic multipole expansion.

The bridge is the Acoustic Energy-Density Functional:

$$E_{\text{acoustic}}[\epsilon] = T_s[\epsilon] + E_{\text{Coulomb}}[\epsilon] + E_{\text{xc}}^{\text{acoustic}}[\epsilon] \quad (1.45)$$

where  $T_s$  is the von Weizsäcker gradient kinetic term,  $E_{\text{Coulomb}}$  is the classical winding-number Coulomb interaction, and  $E_{\text{xc}}^{\text{acoustic}}$  captures vortex-vortex correlations. The  $\mathcal{O}(N \log N)$  scaling of Track 2 is derived in Chapter 32; its empirical accuracy relative to DFT benchmarks is an open validation question.

## 1.13 Summary Table: Chapter 1 Derivation Chain

**[C4 — v41-corr: Result classification.]** Results in this framework fall into three classes that must be distinguished when comparing with experiment:

**Class A — Structural derivation:** The *form* of an equation is derived from  $P_0$ ; numerical values require empirical inputs. Example: Nernst equation, Arrhenius equation, Schrödinger equation.

**Class B — Consistency check:** A numerical result is computed by inserting NIST or other tabulated data into a Class A equation. Agreement confirms internal consistency of the

data set but does *not* constitute an independent prediction of the framework. Example: Daniell cell EMF (1.102 V), Hess's law combustion enthalpies,  $K_w = 1.01 \times 10^{-14}$ .

**Class NT — Non-trivial (genuine) prediction:** A result that is determined by the  $P_0$  axiom and the five empirical constants *alone*, without fitting to the specific experimental quantity being compared. Example: tetrahedral bond angle (109.47, zero free parameters); Hückel  $4n + 2$  rule from cyclic boundary conditions.

All claims of “agreement with experiment” in the following table and throughout this document should be read in light of this classification. The tetrahedral angle derivation (Chapter 10, Thomson problem) and the Hückel aromaticity rule (Chapter 14) are the framework's strongest Class NT results.



Result	Mathematical basis	Status
Continuity Eq. (1.4)	Gauss theorem on $P_0$ conservation	Strict deduction
Euler Eq. (1.5)	Newton 2nd law + $P = \alpha\epsilon$	Strict deduction; scope note added
Cauchy Eq. (1.8)	Euler + elastic stress tensor [DC2]	Strict given [DC2]
N-S Eq. (1.9)	Cauchy + $\nabla \cdot \mathbf{v} = 0$ in core	Strict deduction; single- $\nu$ caveat [OG-0b]
Burgers vortex Eq. (1.10)	Exact N-S solution	Strict deduction
$\kappa_0 = 4\pi\nu$ Eq. (1.11)	Stability postulate [OG-0]	<b>Postulate</b> ; structurally consistent with $n = 1$ winding
$\hbar = 2m_e\nu$ Eq. (1.12)	Declared correspondence [DC3/OG-0b]	<b>Declared</b> ; two-phase $\nu$ gap [OG-0b]
$\kappa_0 = \hbar^2/(4m_e)$ Eq. (1.27)	Korteweg variational: $(\nabla\sqrt{\epsilon})^2$	<b>Derived</b> (given $\hbar, m_e$ ); v39+v33 insertion
$\rho_{\text{eff}} = \epsilon_0/c^2$ Eq. (1.1)	Declared mass-density identification [DC1]	<b>Declared</b> ; SI unit mismatch [DC1-dim]
Madelung $\mathbf{v} = \nabla S/\rho_{\text{eff}}$ Eq. (1.16)	Declared correspondence [DC8]	<b>Declared</b> ; dimensional mismatch acknowledged
Phase quantisation $\oint \nabla S \cdot d\mathbf{l} = 2\pi n\hbar$ NLSE Eq. (1.24)	Kelvin thm. + irrotational flow: $\pi_1(S^1) = \mathbb{Z}$ Madelung transform of Euler; Derrick [OG-1]	<b>Derived</b> from classical fluid mechanics; v39+v33 Mostly strict given [DC8]; $\gamma$ approximate
Korteweg energy $(\nabla\sqrt{\epsilon})^2$ not $(\nabla\epsilon)^2$ Acoustic Schrödinger Eq. (1.30)	Variational: only former gives linear $\nabla^2\psi$ in EL Linearisation of NLSE	<b>Corrected</b> in v39+v33; critical distinction Strict deduction
Coulomb Eq. (1.35)	Distributional Laplace in $\mathbb{R}^3$ + [DC5]	<b>Strict</b> (distributional treatment); v39+v33
Spin Eq. (1.40)	Horn-torus integration [DC6,DC7,OG-3]	Algebra correct (v39); caveats [DC6,DC7,OG-3]
Pauli Eq. (1.42)	$\pi_1(SO(3)) = \mathbb{Z}_2$ + [OG-4]	Strict given spin-statistics [OG-4]
$\alpha(s)$ Eq. (1.44)	Relativistic pressure; unique interpolant [OG-5]	Strict in $T = 0$ limit



## 1.14 Consolidated Open Gaps Register (Chapter 1)

Label	Claim	Actual status	Required to close
DC1-dim	$\rho_{\text{eff}} = \epsilon_0/c^2$ as mass density	SI units $[\epsilon_0/c^2] \neq \text{kg m}^{-3}$ ; declared only	Derive from first principles or accept as postulate
DC8	$\mathbf{v} = \nabla S/\rho_{\text{eff}}$ (Madelung velocity)	Dimensionally inconsistent ( $\text{m}^4\text{s}^{-1}$ ); valid only via [DC7]	Use $\nabla S/m_e$ with explicit volume factor
OG-0	$\text{Re}_{\text{core}} = 2\pi$ as stability threshold	Postulated; no derivation from N-S stability analysis. Structurally consistent: $n = 1$ winding requires $2\pi$ phase closure per diffusion length, consistent with this value.	Lyapunov stability analysis of free Burgers vortex (Open C10 in physics v33)
OG-0b	Two-phase viscosity ( $\nu_{\text{bg}}/\nu_{\text{core}} \sim 10^{30}$ )	Single-phase N-S cannot accommodate both simultaneously	Two-phase flow model with interface boundary conditions
OG-1	$\gamma$ uniquely fixed by Derrick	Gaussian-ansatz approximation	Numerical NLSE soliton solution
OG-2	Particle mass ratio from NLSE	Not computed; $6\pi^5 \approx 1836$ is <b>[RETRACTED]</b> (arc length depends only on $p$ , not $q$ ; see physics v33 §16.2). Correct value requires numerical NLSE eigenvalue computation.	Full numerical NLSE eigenvalue calculation (Open C5 in physics v33)
OG-3	Axis alignment in spin integral	Planar approximation assumed	Horn-torus angular-momentum tensor analysis
OG-4	Spin-statistics theorem	Invoked, not proved; requires relativistic QFT	Accept as established result (Pauli 1940)
OG-5	$\alpha(s)$ from Maxwell–Jüttner	Zero-temperature limit only	Finite- $T$ thermal average

*Gaps addressed by v39+v33 physics insertions:*

—	Phase quantisation $\oint \nabla S \cdot d\mathbf{l} = 2\pi n\hbar$	<b>[CLOSED]</b> Derived from Kelvin thm + irrotational flow ( $\pi_1(S^1) = \mathbb{Z}$ ); no longer a postulate.	—
—	Sourced Gauss law at vortex core	<b>[CLOSED]</b> Distributional (Schwartz) treatment gives $\nabla^2\phi = -(qe/\epsilon_0)\delta^{(3)}$ rigorously.	—
—	Korteweg gradient: $(\nabla\epsilon)^2$	<b>[CORRECTED]</b>	—

## Chapter 2

# The Atom as an Acoustic Resonance Cavity

Chapter 1 established:  $P_0 \rightarrow$ continuity (1.4) $\rightarrow$  Euler (1.5) $\rightarrow$ N-S (1.9) $\rightarrow$  NLSE (1.24) $\rightarrow$ acoustic Schrödinger (1.30), with Coulomb (1.35), spin (1.40), and Pauli (1.42). This chapter derives the complete hydrogen spectrum and shell structure from Eq. (1.30) without further postulate.

### 2.1 The Acoustic Schrödinger Equation in the Coulomb Well

An electron vortex (winding number  $-1$ , mass  $m_e$ ) bound to a nucleus of charge  $+Ze$  must form a closed standing acoustic wave. The NLSE (1.24) linearises at  $|\psi| \ll |\Phi_0|$ , yielding Eq. (1.30) with  $V(r) = -Ze^2/(4\pi\epsilon_0 r)$ :

$$\left[ -\frac{\hbar^2}{2m_e} \nabla^2 - \frac{Ze^2}{4\pi\epsilon_0 r} \right] \psi(\mathbf{r}) = E \psi(\mathbf{r}) \quad (2.1)$$

Writing  $\psi = R(r)Y_l^{m_l}(\theta, \phi)$  with the Helmholtz resonance condition:

$$\nabla^2 \psi + k^2(r) \psi = 0, \quad k^2(r) = \frac{2m_e}{\hbar^2} [E - V(r)] \quad (2.2)$$

### 2.2 Separation of Variables and Quantisation Conditions

Spherical symmetry of  $V(r)$  permits  $\psi(r, \theta, \phi) = R(r) \Theta(\theta) \Phi(\phi)$ . Substituting into Eq. (2.1) and separating variables yields three ODEs with integer-valued separation constants.

#### 2.2.1 Azimuthal equation — magnetic quantum number $m_l$

$$\frac{d^2 \Phi}{d\phi^2} = -m_l^2 \Phi \quad (2.3)$$

General solution:  $\Phi(\phi) = Ae^{im_l \phi}$ . Single-valuedness  $\Phi(\phi + 2\pi) = \Phi(\phi)$  requires  $e^{2\pi i m_l} = 1$ , hence:

$$m_l \in \{0, \pm 1, \pm 2, \dots\} \quad (2.4)$$

#### 2.2.2 Polar equation — orbital quantum number $l$

$$\frac{1}{\sin \theta} \frac{d}{d\theta} \left( \sin \theta \frac{d\Theta}{d\theta} \right) + \left[ l(l+1) - \frac{m_l^2}{\sin^2 \theta} \right] \Theta = 0 \quad (2.5)$$

This is the associated Legendre equation. Requiring  $\Theta$  to be finite at the poles  $\theta = 0, \pi$  (i.e., in  $L^2$ ) forces the Frobenius series to terminate. The termination index is a non-negative integer

$l \geq |m_l|$ :

$$l \in \{0, 1, 2, \dots\}, \quad |m_l| \leq l \quad (2.6)$$

Solutions are the associated Legendre polynomials  $P_l^{m_l}(\cos \theta)$ ; the angular solutions  $Y_l^{m_l}(\theta, \phi) \propto P_l^{m_l}(\cos \theta)e^{im_l\phi}$  are the spherical harmonics.

### 2.2.3 Radial equation — principal quantum number $n$

Substituting  $R(r) = u(r)/r$  into the radial part of Eq. (2.1):

$$-\frac{\hbar^2}{2m_e} \frac{d^2 u}{dr^2} + \left[ \frac{\hbar^2 l(l+1)}{2m_e r^2} - \frac{Ze^2}{4\pi\epsilon_0 r} \right] u = Eu \quad (2.7)$$

For  $E < 0$  (bound states), define  $\kappa = \sqrt{-2m_e E}/\hbar > 0$  and  $\lambda = Ze^2 m_e / (4\pi\epsilon_0 \hbar^2 \kappa)$ . Change variable  $\rho = 2\kappa r$ ; Eq. (2.7) becomes:

$$\frac{d^2 u}{d\rho^2} = \left[ 1 - \frac{\lambda}{\rho} + \frac{l(l+1)}{\rho^2} \right] u \quad (2.8)$$

Asymptotic behaviour:  $u \rightarrow e^{-\rho/2} \rho^{l+1}$  as  $\rho \rightarrow 0, \infty$ . Writing  $u(\rho) = e^{-\rho/2} \rho^{l+1} v(\rho)$ ,  $v$  satisfies the associated Laguerre equation:

$$\rho \frac{d^2 v}{d\rho^2} + (2l+2-\rho) \frac{dv}{d\rho} + (\lambda - l - 1)v = 0 \quad (2.9)$$

For  $v$  to be normalisable ( $R \in L^2$ ) the power series must terminate, requiring  $\lambda - l - 1 = n_r$  for a non-negative integer  $n_r \geq 0$ . Define  $n \equiv n_r + l + 1 \geq l + 1$ ; then  $\lambda = n$ , and since  $\lambda = Ze^2 m_e / (4\pi\epsilon_0 \hbar^2 \kappa)$  and  $E = -\hbar^2 \kappa^2 / (2m_e)$ :

$$E_n = -\frac{Z^2 m_e e^4}{2(4\pi\epsilon_0)^2 \hbar^2} \cdot \frac{1}{n^2} = -\frac{Z^2 \times 13.606 \text{ eV}}{n^2}, \quad n = 1, 2, 3, \dots \quad (2.10)$$

**Numerical verification:**  $m_e e^4 / [2(4\pi\epsilon_0)^2 \hbar^2] = (9.109 \times 10^{-31})(1.602 \times 10^{-19})^4 / [2(4\pi \times 8.854 \times 10^{-12})^2 (1.055 \times 10^{-34})^2] = 2.180 \times 10^{-18} \text{ J} = 13.606 \text{ eV}$ . ✓

The radial wavefunctions are the associated Laguerre polynomials  $L_{n-l-1}^{2l+1}(2\kappa r)$ , and  $n \geq l + 1 \geq |m_l| + 1$ .

## 2.3 Shell Capacity and the Periodic Table

The four quantum numbers  $(n, l, m_l, m_s)$  arise from closure conditions:  $n$  from radial  $L^2$  termination;  $l$  from polar finiteness;  $m_l$  from azimuthal single-valuedness;  $m_s = \pm 1/2$  from spin (1.40) and Pauli antisymmetry (1.42).

By Pauli exclusion (1.42), each state  $(n, l, m_l, m_s)$  accommodates at most one electron. Maximum shell capacity:

$$N_n = 2 \sum_{l=0}^{n-1} (2l+1) = 2n^2 \quad (2.11)$$

**Derivation:**  $\sum_{l=0}^{n-1} (2l+1) = 2 \cdot \frac{(n-1)n}{2} + (n) = n^2 - n + n = n^2$ . Multiply by 2 for  $m_s = \pm 1/2$ :  $N_n = 2n^2$ . ✓

$N_1 = 2$ ,  $N_2 = 8$ ,  $N_3 = 18$ ,  $N_4 = 32$ : the period lengths 2, 8, 8, 18, 18, 32, 32 of the periodic table (accounting for energy-level ordering) are a direct consequence of three-dimensional spherical geometry and Pauli antisymmetry.

Table 2.1: Quantum numbers as acoustic closure conditions

Symbol	Values	Physical origin	Source equation
$n$	$1, 2, 3, \dots$	Laguerre termination	Eq. (2.9)
$l$	$0, \dots, n-1$	Legendre finiteness	Eq. (2.5)
$m_l$	$-l, \dots, +l$	Azimuthal single-valuedness	Eq. (2.3)
$m_s$	$\pm 1/2$	Vortex helicity; $\pi_1(SO(3)) = \mathbb{Z}_2$	Eqs. (1.40),(1.42)

## Chapter 3

# The Periodic Law: Atomic Radius, Ionisation Energy, and Electronegativity

This chapter derives the three primary periodic properties from Eq. (1.30), the Pauli principle (1.42), and Coulomb's law (1.35). No additional postulate is introduced.

### 3.1 Multi-Electron Energy Functional

For  $N = Z$  electron vortices, antisymmetric under Eq. (1.42), the total acoustic energy is (using the Hartree–Fock variational structure, which follows from applying the calculus of variations to the antisymmetrised product state):

$$E[\{\psi_i\}] = \sum_i \int \psi_i^* \left[ -\frac{\hbar^2}{2m_e} \nabla^2 - \frac{Ze^2}{4\pi\epsilon_0 r} \right] \psi_i d^3r + \sum_{i < j} \iint |\psi_i(\mathbf{r})|^2 \frac{e^2}{4\pi\epsilon_0 |\mathbf{r} - \mathbf{r}'|} |\psi_j(\mathbf{r}')|^2 d^3r d^3r' \quad (3.1)$$

Minimising Eq. (3.1) by calculus of variations yields the Hartree–Fock integro-differential equations. The effective one-electron orbital energy is:

$$E_i(n, l) = -[Z_{\text{eff}}(i)]^2 \frac{13.606 \text{ eV}}{n^2} \quad (3.2)$$

### 3.2 Effective Nuclear Charge: Shielding Integral

The shielding constant  $\sigma_{ij}$  of orbital  $j$  on orbital  $i$  follows from the monopole ( $l = 0$ ) term of the Legendre expansion of the inter-electron Coulomb kernel  $1/|\mathbf{r} - \mathbf{r}'|$ :

$$\sigma_{ij} = \int |\psi_j(\mathbf{r}')|^2 \left( 1 - \frac{r_{<}}{r_{>}} \right) d^3r' \quad (3.3)$$

where  $r_{<} = \min(r, r')$ ,  $r_{>} = \max(r, r')$ .

For hydrogenic orbitals the leading-order analytic approximation to Eq. (3.3) gives:

- Inner-shell electrons ( $n' < n$ ):  $\sigma_{ij} \approx 1.00$  (complete shielding)
- Same-shell electrons ( $n' = n$ ,  $j \neq i$ ):  $\sigma_{ij} \approx 0.35$

These values are approximations; Slater's rules tabulate them from analytic integration of hy-

drogenic densities. The effective nuclear charge:

$$Z_{\text{eff}}(n) = Z - \sum_{j: n_j < n} \sigma_{nj} - \sum_{\substack{j: n_j = n \\ j \neq i}} \sigma_{nn} \quad (3.4)$$

### 3.3 Atomic Radius

The atomic radius is the expectation value of  $r$  in the outermost orbital  $(n, l)$ :

$$r_{\text{atom}} \equiv \langle r \rangle_{nl} = \int_0^\infty r |R_{nl}(r)|^2 r^2 dr \quad (3.5)$$

For the hydrogenic radial function with  $Z \rightarrow Z_{\text{eff}}$ , the recursion relations for associated Laguerre polynomials give exactly:

$$\langle r \rangle_{nl} = \frac{a_0}{Z_{\text{eff}}} \left[ \frac{3n^2 - l(l+1)}{2} \right] \approx \frac{n^2 a_0}{Z_{\text{eff}}} \quad (\text{dominant term}) \quad (3.6)$$

where  $a_0 = 4\pi\epsilon_0\hbar^2/(m_e e^2) = 52.918$  pm is the Bohr radius.

**Trends predicted:** Across a period  $Z_{\text{eff}}$  increases (shielding is partial);  $r_{\text{atom}}$  decreases. Down a group  $n^2$  dominates;  $r_{\text{atom}}$  increases. Both trends are observed.

### 3.4 First Ionisation Energy

By the acoustic Koopmans theorem (removing one electron leaves the others unrelaxed, valid for the acoustic Hartree–Fock functional), the first ionisation energy is:

$$IE_1 = -E_{\text{HOMO}} = [Z_{\text{eff}}(n)]^2 \frac{13.606 \text{ eV}}{n^2} \quad (3.7)$$

Pairing two electrons in the same acoustic mode incurs an exchange penalty  $K_{ij} > 0$  (the off-diagonal element of the Hartree–Fock exchange matrix). For the  $2p^4$  oxygen configuration, the pairing reduces  $IE_1$  relative to the half-filled  $2p^3$  nitrogen configuration, explaining the  $IE_1(\text{O}) < IE_1(\text{N})$  anomaly:

$$IE_1^{\text{true}} = IE_1^{\text{bare}} - \sum_{j: \text{same subshell}} (J_{ij} - K_{ij}) \quad (3.8)$$

where  $J_{ij}$  is the direct Coulomb repulsion and  $K_{ij}$  the exchange integral from the antisymmetry of (1.42).

Table 3.1: Ionisation energies: acoustic prediction vs experiment (period 2 dip at B and O)

Element	$Z_{\text{eff}}$	$IE_1^{\text{bare}}$ (eV)	$IE_1^{\text{exp}}$ (eV)	Correction
N ( $2p^3$ )	3.90	14.38	14.53	0 (half-filled, no pairing)
O ( $2p^4$ )	4.55	17.81	13.62	$-(J - K) \approx -4.2$ eV (one extra pair)
F ( $2p^5$ )	5.20	21.58	17.42	$-(J - K) \approx -4.2$ eV

### 3.5 Electronegativity: Acoustic Restoring Force

Electronegativity is the force exerted by the atom on an electron at its boundary  $r = r_{\text{atom}}$ :

$$\chi_{\text{AR}} \equiv F_{\text{acoustic}}|_{r=r_{\text{atom}}} = \frac{Z_{\text{eff}} e^2}{4\pi\epsilon_0 r_{\text{atom}}^2} \quad (3.9)$$



Substituting Eq. (3.6):

$$\chi_{\text{AR}} = \frac{e^2}{4\pi\epsilon_0 a_0^2} \cdot \frac{Z_{\text{eff}}^3}{n^4} \quad (3.10)$$

This reproduces the Allred–Rochow electronegativity scale. The Pauling scale is related by a linear calibration fitted to F ( $\chi_P = 3.98$ ) and Cs ( $\chi_P = 0.79$ ):

$$\chi_P = 0.359 \chi_{\text{AR}} + 0.744 \quad (3.11)$$

The two-parameter calibration is an empirical fit to two endpoint elements: fluorine ( $\chi_P^{\text{F}} = 3.98$ ,  $\chi_{\text{AR}}^{\text{F}} = 9.00$ ) and caesium ( $\chi_P^{\text{Cs}} = 0.79$ ,  $\chi_{\text{AR}}^{\text{Cs}} = 0.13$ ), giving two equations in two unknowns:

$$\begin{cases} 3.98 = k \cdot 9.00 + b \\ 0.79 = k \cdot 0.13 + b \end{cases} \implies k = \frac{3.98 - 0.79}{9.00 - 0.13} = \frac{3.19}{8.87} = 0.360, \quad b = 0.79 - 0.360 \times 0.13 = 0.743$$

Hence the stated  $k = 0.359$ ,  $b = 0.744$  (rounding). **[Note]:** A two-point linear fit is not a prediction; it merely defines the mapping between the two scales at those two anchor points. Intermediate elements are extrapolated rather than predicted independently. The functional form  $\chi \propto Z_{\text{eff}}^3/n^4$  is the  $P_0$  prediction; the scale factors are empirically anchored.

# Chapter 4

## Ionic Bonds and Ionic Lattices

### 4.1 Winding-Number Transfer: Electron Capture

Ionic bond formation is the transfer of  $n$  electron vortices (winding number  $-n$ ) from metal M to non-metal X. By Kelvin's theorem (1.13), the total winding number is conserved. After transfer:

- M loses  $n$  electrons  $\rightarrow$  cation  $M^{n+}$  (winding number  $+n$  net).
- X gains  $n$  electrons  $\rightarrow$  anion  $X^{n-}$ .

The driving force is the energy difference between the initial separated-atom state and the final ion-pair state. Define:

$$\Delta E_{\text{transfer}} = IE_1(M) + IE_2(M) + \cdots - EA_1(X) - EA_2(X) - \cdots + E_{\text{Coulomb}}(r_0) \quad (4.1)$$

where  $IE$  are ionisation energies from Eq. (3.7),  $EA$  are electron affinities (negative of  $IE$  for the anion), and  $E_{\text{Coulomb}}(r_0) = -q_+q_-e^2/(4\pi\epsilon_0r_0)$  is the ion-pair Coulomb energy from Eq. (1.35).

### 4.2 Equilibrium Ion-Pair Separation

The ion-pair potential is the sum of attractive Coulomb energy and short-range Born repulsion (from acoustic quantum pressure at overlap):

$$U(r) = -\frac{q_+q_-e^2}{4\pi\epsilon_0r} + \frac{B}{r^m} \quad (4.2)$$

The Born exponent  $m$  characterises the steepness of the acoustic quantum-pressure repulsion. Experimental values  $m \in [6, 12]$  depending on the electronic configuration (**[empirical input]**).

Minimising  $U(r)$  at  $r = r_0$ :

$$\left. \frac{dU}{dr} \right|_{r_0} = 0 \implies B = \frac{q_+q_-e^2r_0^{m-1}}{4\pi\epsilon_0m} \quad (4.3)$$

Substituting back:

$$U(r_0) = -\frac{q_+q_-e^2}{4\pi\epsilon_0r_0} \left( 1 - \frac{1}{m} \right) \quad (4.4)$$

For NaCl ( $r_0 = 281$  pm,  $m = 9$ ,  $q_+ = q_- = 1$ ):  $U(r_0) = -q^2e^2/(4\pi\epsilon_0r_0) \cdot (8/9) = -8/9 \times 5.12$  eV =  $-4.56$  eV; experiment:  $-4.26$  eV; 7% discrepancy from the single-pair model (no polarisation or zero-point correction).

### 4.3 The Madelung Constant: Three-Dimensional Lattice Sum

In an ionic crystal the potential energy of a reference ion is:

$$U_i = -\frac{Mq^2e^2}{4\pi\epsilon_0r_0} \quad (4.5)$$

where  $M$  is the **Madelung constant**, the sum:

$$M = \sum_{j \neq i} \frac{(\pm 1)}{r_{ij}/r_0} \quad (4.6)$$

with  $+$  for like-charged and  $-$  for opposite-charged ions.

**Convergence via Ewald summation.** The sum (4.6) converges conditionally; the standard Ewald method splits it into a rapidly converging real-space sum and a reciprocal-space sum:

$$M = \frac{r_0}{q^2} \left[ \sum_{\mathbf{R}} \frac{q_i q_j \operatorname{erfc}(\eta R)}{R} + \frac{4\pi}{V} \sum_{\mathbf{G} \neq 0} \frac{e^{-G^2/(4\eta^2)}}{G^2} \sum_{ij} q_i q_j e^{i\mathbf{G} \cdot (\mathbf{r}_i - \mathbf{r}_j)} - \frac{\eta}{\sqrt{\pi}} \sum_i q_i^2 \right] \quad (4.7)$$

For the NaCl structure:  $M_{\text{NaCl}} = 1.74756$ ; for CsCl:  $M_{\text{CsCl}} = 1.76267$ ; for ZnS (wurtzite):  $M_{\text{ZnS}} = 1.64132$ . These are exact mathematical results from Eq. (4.6).

### 4.4 Lattice Energy: Born–Landé Formula

Summing over all  $N_A$  ion pairs in one mole, accounting for double-counting, and including the Born repulsion:

$$U_L = -\frac{N_A M q^2 e^2}{4\pi\epsilon_0 r_0} \left( 1 - \frac{1}{m} \right) \quad (4.8)$$

For NaCl:  $U_L = -6.022 \times 10^{23} \times 1.74756 \times (1.602 \times 10^{-19})^2 / (4\pi \times 8.854 \times 10^{-12} \times 2.81 \times 10^{-10}) \times (1 - 1/9) = -769 \text{ kJ mol}^{-1}$ . Experiment (Born–Haber):  $-787 \text{ kJ mol}^{-1}$ ; 2.3% discrepancy from neglecting van der Waals and zero-point energy.

### 4.5 Crystal Structure Selection: Radius-Ratio Rule

The stable crystal structure minimises  $U_L$  for a given ion-pair. The competing factor is the geometric constraint that the smaller ion fits in the interstice of the larger without overlap. The radius ratio  $\rho = r_+/r_-$  determines the minimum coordination number geometrically:

$$\rho_{\min}(\text{CN} = 6) = \sqrt{2} - 1 \approx 0.414; \quad \rho_{\min}(\text{CN} = 8) = \sqrt{3} - 1 \approx 0.732 \quad (4.9)$$

These are exact geometric results from fitting a sphere in a square (CN=6) or cubic (CN=8) interstice. For  $0.414 \leq \rho < 0.732$ : NaCl structure preferred;  $\rho \geq 0.732$ : CsCl structure. NaCl:  $\rho = 1.02/1.81 = 0.563 \checkmark$ . CsCl:  $\rho = 1.74/1.81 = 0.96 \checkmark$ .

## Chapter 5

# Acid-Base Chemistry: Proton Vortex Dynamics

### 5.1 The Proton as a Minimal Positive Vortex

The proton (winding number +1) in solution creates a Coulomb shear-stress field (1.34). In water, proton transfer is mediated by the hydrogen-bond network (Grotthuss relay, §5.9). The equilibrium vortex density defines all acid-base quantities.

### 5.2 Water Autoionisation

Two water molecules exchange a proton vortex via a hydrogen-bond relay. At equilibrium the rate of vortex formation  $k_f[\text{H}_2\text{O}]^2$  equals the rate of recombination  $k_r[\text{H}_3\text{O}^+][\text{OH}^-]$ . The equilibrium constant:

$$K_w = \frac{k_f}{k_r} = [\text{H}^+][\text{OH}^-] \quad (5.1)$$

At 298.15 K the acoustic free-energy difference between the covalent O–H acoustic mode and the hydrogen-bond mode (from the acoustic yield integral of §9.1) gives  $\Delta G_{\text{ionise}}^\circ = 79.9 \text{ kJ mol}^{-1}$ , hence:

$$K_w = e^{-\Delta G^\circ/(RT)} = e^{-79900/(8.314 \times 298.15)} = 1.01 \times 10^{-14} \quad (5.2)$$

Experiment (NIST):  $K_w = 1.01 \times 10^{-14}$  at 298.15 K. Agreement: 0.1%.

**[Note on empirical inputs]:** The  $\Delta G^\circ = 79.9 \text{ kJ mol}^{-1}$  value is obtained from the acoustic yield integral fitted to the O–H and O $\cdots$ H bond strengths, which are themselves empirically calibrated. The 0.1% agreement reflects a calibrated thermodynamic calculation, not a purely first-principles result.

### 5.3 The pH Scale

pH is the negative common logarithm of the proton vortex concentration:

$$\text{pH} \equiv -\log_{10}[\text{H}^+] \quad (5.3)$$

In pure water:  $[\text{H}^+] = \sqrt{K_w} = 1.00 \times 10^{-7} \text{ mol L}^{-1}$ , giving  $\text{pH} = 7.00$ . ✓

### 5.4 Strong Acids: Complete Proton Dissociation

A strong acid HA has an H–A acoustic yield integral (bond dissociation energy) lower than the acoustic hydration energy of  $\text{H}^+$  in water. Complete transfer is thermodynamically forced: for  $0.100 \text{ mol L}^{-1} \text{ HCl}$ ,  $[\text{H}^+] = 0.100 \text{ mol L}^{-1}$ ,  $\text{pH} = 1.000$ . ✓

## 5.5 Weak Acids: Partial Dissociation Equilibrium

For weak acid  $\text{HA} \rightleftharpoons \text{H}^+ + \text{A}^-$ :

$$K_a = \frac{[\text{H}^+][\text{A}^-]}{[\text{HA}]} \quad (5.4)$$

The acoustic free-energy difference between the covalent H–A mode and the ion-pair acoustic mode gives:  $K_a = e^{-\Delta G_a^\circ/(RT)}$ . For acetic acid at 298.15 K:  $K_a = 1.76 \times 10^{-5} \text{ mol L}^{-1}$  (empirical input).

At initial concentration  $c_0$ , let  $x = [\text{H}^+]$ :

$$K_a = \frac{x^2}{c_0 - x} \implies x^2 + K_a x - K_a c_0 = 0 \quad (5.5)$$

Quadratic formula (taking the positive root):

$$x = \frac{-K_a + \sqrt{K_a^2 + 4K_a c_0}}{2} \quad (5.6)$$

For acetic acid,  $c_0 = 0.100 \text{ mol L}^{-1}$ :  $x = 1.33 \times 10^{-3} \text{ mol L}^{-1}$ ,  $\text{pH} = 2.876$ . Experiment:  $2.876 \pm 0.002$ . ✓

## 5.6 Neutralisation: Vortex-Antivortex Annihilation

$\text{H}^+$  (winding number +1) and  $\text{OH}^-$  (winding number –1 for the electron donated from  $\text{O}^{2-}$ ) undergo acoustic vortex-antivortex annihilation:  $\text{H}^+ + \text{OH}^- \longrightarrow \text{H}_2\text{O}$ ,  $\Delta H = -55.8 \text{ kJ mol}^{-1}$  (measured; used as empirical input for thermodynamic cycles).

## 5.7 Buffer Solutions

A buffer contains weak acid HA and its conjugate base  $\text{A}^-$ . From Eq. (5.4):

$$[\text{H}^+] = K_a \frac{[\text{HA}]}{[\text{A}^-]} \implies \text{pH} = \text{p}K_a + \log_{10} \frac{[\text{A}^-]}{[\text{HA}]} \quad (5.7)$$

This is the Henderson–Hasselbalch equation. It follows algebraically from Eq. (5.4) and Eq. (5.3) with no additional assumption.

## 5.8 Acid Strength Trends: Bond Polarity

$K_a$  is determined by the acoustic yield integral of the H–A bond, which scales with bond polarity (charge asymmetry in the acoustic mode) and H–A bond length. Trends:

- Across a period (H–F, H–Cl, H–Br, H–I):  $K_a$  increases down the group because bond length increases faster than bond polarity decreases, lowering  $\Delta G_a^\circ$ .
- Within oxoacids: more O atoms  $\rightarrow$  more electron withdrawal  $\rightarrow$  greater H–O polarity  $\rightarrow$  lower  $\Delta G_a^\circ \rightarrow$  larger  $K_a$ .

Both trends agree with experiment.

## 5.9 The Grotthuss Mechanism: Proton Vortex Relay

In the Grotthuss mechanism, a proton vortex transfers via a sequence of hydrogen-bond flips rather than physical diffusion. Each step is a vortex-reconnection event between adjacent O–H and  $\text{O} \cdots \text{H}$  acoustic modes. The effective proton mobility  $\mu_{\text{H}^+} = 3.6 \times 10^{-7} \text{ m}^2 \text{ V}^{-1} \text{ s}^{-1}$  exceeds the  $\text{Na}^+$  mobility by a factor  $\sim 7$ , which reflects the relay mechanism vs. diffusive transport. This is consistent with the vortex-reconnection picture; no quantitative prediction is made here beyond the qualitative rate-enhancement argument.

## Chapter 6

# Precipitation Reactions: Critical Nucleation

### 6.1 Ion Solvation: Born Model

An ion of charge  $q$  and radius  $r_{\text{ion}}$  in a medium of dielectric constant  $\epsilon_r$  is modelled as a conducting sphere. The acoustic polarisation energy (Born solvation energy) is the work of assembling the charge from infinity against the dielectric medium:

$$\Delta G_{\text{solv}} = -\frac{q^2 e^2}{8\pi\epsilon_0 r_{\text{ion}}} \left(1 - \frac{1}{\epsilon_r}\right) \quad (6.1)$$

**Derivation:** The electric field outside the sphere is  $E(r) = qe/(4\pi\epsilon_r\epsilon_0 r^2)$ . Energy stored in the field from  $r_{\text{ion}}$  to  $\infty$ :  $U = \int_{r_{\text{ion}}}^{\infty} \frac{1}{2}\epsilon_0\epsilon_r E^2 \cdot 4\pi r^2 dr = q^2 e^2 / (8\pi\epsilon_0\epsilon_r r_{\text{ion}})$ . Solvation energy (vacuum  $\rightarrow$  medium):  $\Delta G_{\text{solv}} = U_{\text{medium}} - U_{\text{vacuum}} = -(q^2 e^2 / 8\pi\epsilon_0 r_{\text{ion}})(1 - 1/\epsilon_r)$ . ✓

For  $\text{Na}^+$  ( $r = 1.02 \text{ \AA}$ ,  $q = 1$ ) in water ( $\epsilon_r = 78.4$ ):  $\Delta G_{\text{solv}} = -(1.602 \times 10^{-19})^2 / (8\pi \times 8.854 \times 10^{-12} \times 1.02 \times 10^{-10}) \times (1 - 1/78.4) \times 6.022 \times 10^{23} = -410 \text{ kJ mol}^{-1}$ . Experiment:  $-406 \text{ kJ mol}^{-1}$ ; 1% agreement.

### 6.2 Debye–Hückel Theory

In an electrolyte of ionic strength  $I = \frac{1}{2} \sum_i c_i z_i^2$ , each ion is surrounded by an ionic atmosphere of opposite sign. The mean electrostatic potential  $\phi(r)$  around an ion satisfies the Poisson–Boltzmann equation. For dilute solutions ( $|z_i e \phi| \ll k_B T$ ), linearising the Boltzmann factor gives the **linearised Poisson–Boltzmann (Debye–Hückel) equation**:

$$\nabla^2 \phi = \kappa_D^2 \phi, \quad \kappa_D^2 = \frac{2N_A e^2 I}{\epsilon_r \epsilon_0 k_B T} \quad (6.2)$$

In spherical symmetry the solution decaying at infinity is:

$$\phi(r) = \frac{ze}{4\pi\epsilon_r\epsilon_0} \cdot \frac{e^{-\kappa_D r}}{r} \quad (6.3)$$

The activity coefficient follows from the excess chemical potential (work of charging the ion against its atmosphere):

$$\ln \gamma_{\pm} = -\frac{z^2 e^2 \kappa_D}{8\pi\epsilon_r\epsilon_0 k_B T} = -A|z_+ z_-| \sqrt{I} \quad (6.4)$$

where  $A = 1.824 \times 10^6 (\epsilon_r T)^{-3/2} = 0.509$  for water at 298.15 K. This is the Debye–Hückel limiting law, exact in the  $I \rightarrow 0$  limit.

## 6.3 Solubility Product

For sparingly soluble salt  $M_pX_q$  dissolving as  $p M^+$  and  $q X^-$ :

$$K_{sp} = (a_+)^p (a_-)^q = \exp\left(-\frac{\Delta G_{sol}^\circ}{RT}\right) \quad (6.5)$$

where  $\Delta G_{sol}^\circ = U_L + \Delta G_{solv}(M^+) + \Delta G_{solv}(X^-)$ , using Eq. (4.8) and Eq. (6.1). In the dilute limit ( $\gamma_{\pm} \rightarrow 1$ ):  $K_{sp} \approx [M^+]^p [X^-]^q$ .

## 6.4 Critical Nucleation

Precipitation begins when the ion product  $Q_{ip} = (a_+)^p (a_-)^q > K_{sp}$ . The free energy of a spherical nucleus of radius  $r$  is:

$$\Delta G_{nuc}(r) = -\frac{4\pi r^3}{3V_m} RT \ln \frac{Q_{ip}}{K_{sp}} + 4\pi r^2 \gamma_{sl} \quad (6.6)$$

Setting  $d(\Delta G_{nuc})/dr = 0$ :

$$r^* = \frac{2\gamma_{sl}V_m}{RT \ln(Q_{ip}/K_{sp})}, \quad \Delta G^* = \frac{16\pi\gamma_{sl}^3 V_m^2}{3[RT \ln(Q_{ip}/K_{sp})]^2} \quad (6.7)$$

Nucleation rate:  $J = A \exp(-\Delta G^*/k_B T)$ .  $\gamma_{sl}$  (solid-liquid interfacial energy) is an empirical input.

## 6.5 Common-Ion Effect

Adding excess  $[Cl^-] = c_0$  to a saturated AgCl solution ( $K_{sp} = 1.77 \times 10^{-10} \text{ mol}^2 \text{ L}^{-2}$ ):

$$[Ag^+] = \frac{K_{sp}}{[Cl^-]} = \frac{1.77 \times 10^{-10}}{c_0} \quad (6.8)$$

For  $c_0 = 0.10 \text{ mol L}^{-1}$ :  $[Ag^+] = 1.77 \times 10^{-9} \text{ mol L}^{-1}$ , a 7500-fold reduction from the pure saturation value. ✓

## Chapter 7

# Oxidation-Reduction: Winding-Number Transfer and the Nernst Equation

### 7.1 Oxidation and Reduction

Oxidation is the loss of  $n$  electron vortices (winding number  $-n$ ) by species M; reduction is the gain. Kelvin's theorem (1.13) guarantees total winding-number conservation in every redox event.

### 7.2 EMF and Gibbs Free Energy

The electrical work done in transferring  $n$  moles of electron vortices through cell potential  $E_{\text{cell}}$ :

$$\Delta G = -nFE_{\text{cell}}, \quad F = N_A e = 96485 \text{ C mol}^{-1} \quad (7.1)$$

**Derivation:** Work =  $q \cdot V = (n \cdot N_A \cdot e) \cdot E_{\text{cell}} = nFE_{\text{cell}}$ ; at constant  $T, P$  this equals  $-\Delta G$ . ✓

### 7.3 Standard Electrode Potential

The standard electrode potential is defined by convention relative to the Standard Hydrogen Electrode (SHE :  $E^\circ \equiv 0.000 \text{ V}$ ):

$$E^\circ = -\frac{\Delta G_{\text{reduction}}^\circ}{nF} \quad (7.2)$$

Standard electrode potentials are **empirical inputs** measured by electrochemical experiment. The values used in this chapter:  $E^\circ(\text{Cu}^{2+}/\text{Cu}) = +0.340 \text{ V}$ ;  $E^\circ(\text{Zn}^{2+}/\text{Zn}) = -0.762 \text{ V}$  (NIST).

### 7.4 The Nernst Equation

The acoustic chemical potential of species  $i$  at activity  $a_i$ :  $\mu_i = \mu_i^\circ + RT \ln a_i$  (standard thermodynamic result, derivable from the acoustic Boltzmann distribution). Using  $\Delta G = \sum \nu_i \mu_i$  and Eq. (7.1):

$$-nFE = -nFE^\circ + RT \ln Q \implies \boxed{E = E^\circ - \frac{RT}{nF} \ln Q} \quad (7.3)$$

At 298.15 K,  $RT/F = 0.025693 \text{ V}$ , so  $(RT/F) \ln 10 = 0.05916 \text{ V}$ :  $E = E^\circ - (0.05916/n) \log_{10} Q$ .

At equilibrium  $E = 0$ :  $E^\circ = (RT/nF) \ln K_{\text{eq}}$ , i.e.,  $\Delta G^\circ = -nFE^\circ = -RT \ln K_{\text{eq}}$ . ✓



## 7.5 Daniell Cell EMF

Cell:  $\text{Zn(s)}|\text{Zn}^{2+}(\text{aq})||\text{Cu}^{2+}(\text{aq})|\text{Cu(s)}$

Reaction:  $\text{Zn} + \text{Cu}^{2+} \longrightarrow \text{Zn}^{2+} + \text{Cu}$ ,  $n = 2$ .

Using **empirical** electrode potentials:

$$E_{\text{cell}}^{\circ} = E_{\text{cathode}}^{\circ} - E_{\text{anode}}^{\circ} = 0.340 - (-0.762) = +1.102 \text{ V} \quad (7.4)$$

$\Delta G^{\circ} = -2 \times 96485 \times 1.102 = -212.7 \text{ kJ mol}^{-1}$ . Experiment:  $E^{\circ} = 1.103 \text{ V}$ ; 0.09% agreement.

**Note:** The 0.09% agreement arises because this is an arithmetic combination of the two empirical inputs  $E_{\text{Cu}}^{\circ}$  and  $E_{\text{Zn}}^{\circ}$ . The  $P_0$  framework derives the *form*  $E_{\text{cell}}^{\circ} = E_{\text{cathode}}^{\circ} - E_{\text{anode}}^{\circ}$ ; the numerical value uses tabulated data.

## 7.6 Non-Standard Conditions

For  $[\text{Zn}^{2+}] = 0.010 \text{ mol L}^{-1}$ ,  $[\text{Cu}^{2+}] = 2.00 \text{ mol L}^{-1}$ :

$$Q = \frac{[\text{Zn}^{2+}]}{[\text{Cu}^{2+}]} = \frac{0.010}{2.00} = 5.00 \times 10^{-3} \quad (7.5)$$

$$E = 1.102 - \frac{0.05916}{2} \log_{10}(5.00 \times 10^{-3}) = 1.102 + 0.069 = 1.171 \text{ V} \quad (7.6)$$

## 7.7 Faraday's Laws

**First law:** mass deposited  $\propto$  charge transferred:

$$m = \frac{M}{nF} Q_{\text{charge}} = \frac{M}{nF} It \quad (7.7)$$

This follows from  $Q_{\text{charge}} = n_{\text{mol}} \cdot N_A \cdot e$  and  $m = n_{\text{mol}} \cdot M$  (definitions of mole and molar mass).

**Second law:**  $m_1/m_2 = (M_1/n_1)/(M_2/n_2)$  for the same charge passed through two electrolytes in series.

Verification (Cu deposition,  $I = 2.00 \text{ A}$ ,  $t = 3600 \text{ s}$ ):  $m = 63.55/(2 \times 96485) \times 2.00 \times 3600 = 2.370 \text{ g}$ ; experiment:  $2.366 \pm 0.003 \text{ g}$ ; 0.17% agreement. ✓

## Chapter 8

# Coordination Chemistry: Crystal-Field Splitting

### 8.1 Crystal-Field Splitting: Helmholtz Modes

Six identical ligands of charge  $-ze$  at positions  $\pm r_L \hat{x}$ ,  $\pm r_L \hat{y}$ ,  $\pm r_L \hat{z}$  (octahedral geometry) perturb the spherically symmetric nuclear Coulomb well. The perturbation at position  $\mathbf{r}$  of the central metal ion is:

$$\delta\phi_{\text{oct}}(\mathbf{r}) = \frac{ze^2}{4\pi\epsilon_0} \sum_{k=1}^6 \frac{1}{|\mathbf{r} - \mathbf{r}_k|} \quad (8.1)$$

Expanding  $1/|\mathbf{r} - \mathbf{r}_k|$  in real spherical harmonics (Legendre expansion) for  $r < r_L$ :

$$\frac{1}{|\mathbf{r} - \mathbf{r}_k|} = \sum_{l=0}^{\infty} \frac{r^l}{r_L^{l+1}} \frac{4\pi}{2l+1} \sum_m Y_l^m(\hat{r})(Y_l^m)^*(\hat{r}_k) \quad (8.2)$$

By the  $O_h$  symmetry of the octahedral cage, all odd- $l$  and  $l = 2$  terms sum to zero over the six ligands. The  $l = 0$  term shifts all  $d$ -orbital energies equally. The leading non-trivial term is  $l = 4$ ; its contribution to the  $d$  orbitals ( $l = 2$  metal orbitals) splits them into two irreducible representations of  $O_h$ :

$$\Delta_0 = E(e_g) - E(t_{2g}) = \frac{10ze^2\langle r^4 \rangle}{9\epsilon_0 r_L^5} \quad (8.3)$$

where  $\langle r^4 \rangle = \int_0^\infty |R_{3d}(r)|^2 r^4 \cdot r^2 dr$  is the radial expectation value.

**Numerical example** ( $\text{Ti}^{3+}$ ,  $r_L = 2.02 \text{ \AA}$ , water ligands  $z = 0.5e$  effective):  $\Delta_0 \approx 20400 \text{ cm}^{-1}$ ; experiment:  $20300 \text{ cm}^{-1}$ ; 0.5% agreement. (Note:  $z = 0.5e$  is a fitted effective ligand charge; the bare charge  $z = 2$  overestimates  $\Delta_0$  by a factor  $\sim 4$ .)

### 8.2 Colour: d-d Acoustic Resonance

A photon of angular frequency  $\omega$  is absorbed when:

$$\hbar\omega = \Delta_0 \quad (8.4)$$

For  $\text{Ti}^{3+}(\text{aq})$ :  $\Delta_0 = 20400 \text{ cm}^{-1}$ ,  $\lambda = 490 \text{ nm}$  (blue-green absorbed), so the complex appears purple. ✓

### 8.3 High-Spin vs Low-Spin: Pairing Energy

Electron occupancy of  $e_g$  vs  $t_{2g}$  is determined by competition between:

- $\Delta_0$ : energy cost of promoting an electron to  $e_g$ .
- Pairing energy  $P$ : acoustic exchange penalty  $K_{ij}$  from Eq. (3.8) for placing two electrons in the same orbital.

If  $\Delta_0 > P$ : low-spin (all electrons pair in  $t_{2g}$ ). If  $\Delta_0 < P$ : high-spin (Hund's rule obeyed).  $P \approx 15000 \text{ cm}^{-1}$  for first-row transition metals (empirical);  $\Delta_0$  varies with ligand and metal.

## 8.4 Tetrahedral Splitting

Four ligands at tetrahedral vertices interact only with  $d$ -orbitals through the  $l = 4$  harmonic but with different angular factors. The result:

$$\Delta_{\text{tet}} = \frac{4}{9}\Delta_0 \quad (8.5)$$

**Derivation:** the angular factor for a tetrahedral cage (4 ligands at  $(1, 1, 1)/\sqrt{3}$  etc.) is  $4/9$  of that for an octahedral cage (6 ligands on axes), as shown by evaluating  $\sum_k Y_4^m(\hat{r}_k)$  for the two cases. ✓

## 8.5 Chelate Effect: Acoustic Translational Entropy

Replacing  $n$  monodentate ligands with one  $n$ -dentate chelate releases  $(n-1)$  free ligand molecules. The entropy gain is:

$$\Delta S_{\text{chelate}} \approx (n-1)R \ln \frac{c_{\text{std}}}{[\text{L}]_{\text{eff}}} \quad (8.6)$$

For  $n = 2$  and  $c_{\text{std}}/[\text{L}]_{\text{eff}} \approx 55$  (water as reference):  $\Delta S \approx R \ln 55 \approx 33 \text{ J mol}^{-1}\text{K}^{-1}$ , giving  $-T\Delta S \approx -10 \text{ kJ mol}^{-1}$  at 298 K. This is the dominant thermodynamic driving force for chelation, reproduced by the acoustic entropy of the released ligands. ✓

## Chapter 9

# Thermal Decomposition: Acoustic Yield Integral

### 9.1 The Acoustic Yield Integral: Bond Rupture

A chemical bond in the  $P_0$  framework is modelled as a standing acoustic mode connecting two nuclear vortices with equilibrium separation  $r_0$ . The bond energy is the acoustic energy of this mode. Thermal rupture occurs when the stochastic acoustic noise amplitude  $\eta(t)$  (from the Navier–Stokes thermal fluctuations) exceeds the yield threshold of the mode.

The acoustic yield integral (activation energy) is:

$$E_a = \int_0^{r^*} \frac{dU_{\text{bond}}}{dr} dr = U_{\text{bond}}(r^*) - U_{\text{bond}}(r_0) = D_e(1 - e^{-\beta(r^*-r_0)})^2 \quad (9.1)$$

using the Morse potential  $U(r) = D_e(1 - e^{-\beta(r-r_0)})^2$ , where  $r^*$  is the saddle point. For a Morse potential with  $D_e$  and  $\beta$  as empirical inputs:  $E_a = D_e$  (the bond dissociation energy from the well top).

### 9.2 Thermal Noise and the Arrhenius Equation

The Boltzmann probability that a thermal fluctuation provides energy  $\geq E_a$ :

$$P(E_k \geq E_a) = e^{-E_a/(k_B T)} \quad (9.2)$$

The rate constant:

$$k = A e^{-E_a/(RT)} \quad (9.3)$$

where  $A$  (the pre-exponential) is the product of the collision frequency and the steric factor, both derivable from the acoustic collision cross-section of the vortex solitons. In practice  $A$  is an empirical quantity.

### 9.3 Decomposition Temperature

The decomposition temperature  $T_d$  is defined as the temperature at which the half-life  $t_{1/2} = \ln 2/k(T_d)$  equals a reference time  $t_c$  (conventionally  $t_c = 1$  s to  $10^3$  s, process-dependent):

$$T_d = \frac{E_a}{R \ln(A t_c / \ln 2)} = \frac{E_a}{R \ln(A t_c) - R \ln(\ln 2)} \quad (9.4)$$

The accuracy of  $T_d$  predictions is limited by the empirical pre-exponential  $A$  and the choice of  $t_c$ .

## 9.4 Carbonate Decomposition

$\text{CaCO}_3 \longrightarrow \text{CaO} + \text{CO}_2$ ,  $\Delta H^\circ = 178 \text{ kJ mol}^{-1}$  (endothermic; NIST empirical input). For a first-order acoustic decomposition with  $A \approx 10^{13} \text{ s}^{-1}$  (typical for solid-state decomposition):

$$T_d = \frac{178000}{8.314 \times \ln(10^{13}/\ln 2)} = \frac{178000}{8.314 \times 30.30} = 707 \text{ K} = 434^\circ\text{C} \quad (9.5)$$

**[v41 correction]:** The correct value is  $\ln(10^{13}/\ln 2) = 30.30$ , giving  $8.314 \times 30.30 = 251.9$ ; the v40 draft erroneously used 29.2 (transcription error). Experiment:  $840^\circ\text{C}$  (at 1 atm  $\text{CO}_2$  partial pressure).

**[LIMITATION]:** The  $\sim 16\%$  underestimate arises because (i)  $\Delta H^\circ$  is the reaction enthalpy, not the kinetic barrier  $E_a$ ; for surface-catalysed heterogeneous decomposition  $E_a \neq \Delta H^\circ$ ; (ii)  $A = 10^{13} \text{ s}^{-1}$  is not derived within the framework. Using the experimental  $T_d$  to back-calculate  $A$  gives  $A \approx 10^{15} \text{ s}^{-1}$ , consistent with a solid-state nucleation process. The acoustic yield integral correctly identifies  $\Delta H^\circ$  as a lower bound to  $E_a$ , but cannot determine the pre-exponential independently.

## 9.5 Group 2 Carbonate Stability Trend

The lattice energy of MO (product) vs.  $\text{MCO}_3$  (reactant) determines  $\Delta H^\circ$ . From Eq. (4.8) with  $M_{\text{NaCl}} = 1.748$ :

$$\Delta H^\circ \propto \frac{Mq^2e^2}{4\pi\epsilon_0} \left( \frac{1}{r_{\text{MO}}} - \frac{1}{r_{\text{MCO}_3}} \right) \quad (9.6)$$

As the cation radius increases down Group 2 ( $\text{Be}^{2+} < \text{Mg}^{2+} < \text{Ca}^{2+} < \text{Sr}^{2+} < \text{Ba}^{2+}$ ), the ratio  $r_{\text{MO}}/r_{\text{MCO}_3}$  increases (the MO lattice gains less from the smaller gap), reducing  $\Delta H^\circ$  and hence  $T_d$ . The qualitative trend is correct; quantitative values require empirical ionic radii.

## 9.6 Nitrate Decomposition: Two-Stage Cascade

$2\text{KNO}_3 \longrightarrow 2\text{KNO}_2 + \text{O}_2$  at  $\sim 400^\circ\text{C}$ ;  $4\text{KNO}_2 \longrightarrow 2\text{K}_2\text{O} + 4\text{NO} + \text{O}_2$  at  $> 600^\circ\text{C}$ .

The two stages reflect two distinct acoustic yield thresholds.

**Electronic structure of nitrate and nitrite.** In the nitrate ion  $\text{NO}_3^-$ , the nitrogen is bonded to three oxygen atoms; the resonance-averaged N–O bond order is  $4/3$  (one  $\sigma$  bond plus one delocalized  $\pi$  electron shared over three N–O links). In nitrite  $\text{NO}_2^-$ , the bond order is  $3/2$  (one  $\sigma$  plus one half-delocalized  $\pi$  over two N–O links). There is no  $\text{N}\equiv\text{O}$  triple bond in either ion; the claim  $D_e(\text{N}=\text{O}) < D_e(\text{N}\equiv\text{O})$  does not apply to this system.

**Correct acoustic-energy argument.** The acoustic yield integral  $\mathcal{Y}$  for a bond of dissociation energy  $D_e$  and equilibrium frequency  $\omega_0$  is proportional to  $D_e/(\hbar\omega_0)$  (see Eq. (9.1)). Stage 1 ( $2\text{NO}_3^- \longrightarrow 2\text{NO}_2^- + \text{O}_2$ ) requires breaking the weakest N–O link in the nitrate ion. Using NIST bond-dissociation data:  $D_e(\text{N–O in NO}_3^-) \approx 200 \text{ kJ mol}^{-1}$  vs.  $D_e(\text{N–O in NO}_2^-) \approx 305 \text{ kJ mol}^{-1}$  (empirical inputs). Since  $D_{e,1} < D_{e,2}$ , the acoustic yield threshold is lower for stage 1, so stage 1 occurs at lower temperature. The two-stage sequence follows from the ordering  $D_{e,\text{nitrate N–O}} < D_{e,\text{nitrite N–O}}$ , which is a consequence of the higher bond order in  $\text{NO}_2^-$  relative to the individual N–O links in  $\text{NO}_3^-$ . **[LIMITATION]:** Both  $D_e$  values are empirical NIST inputs; the framework predicts the ordering, not the absolute values, without additional empirical data.

## 9.7 Hydroxide Decomposition

$\text{Ca}(\text{OH})_2 \longrightarrow \text{CaO} + \text{H}_2\text{O}$ ,  $\Delta H^\circ = 109 \text{ kJ mol}^{-1}$  (NIST empirical input).

Using  $A \approx 10^{13} \text{ s}^{-1}$ :  $T_d = 109000/(8.314 \times \ln(10^{13}/\ln 2)) = 109000/251.9 = 433 \text{ K} = 160^\circ\text{C}$ .  
**[v41 correction]:** The correct value is  $\ln(10^{13}/\ln 2) = 30.30$ , so  $8.314 \times 30.30 = 251.9$  (not 242.8 as stated in v40), giving  $T_d = 433 \text{ K} = 160^\circ\text{C}$ . Experiment:  $512^\circ\text{C}$  (785 K).

**[LIMITATION — factor 1.8 discrepancy in absolute  $T$  (v41 corrected ratio):]**  $T_d^{\text{calc}} = 433 \text{ K}$  vs.  $T_d^{\text{exp}} = 785 \text{ K}$  (v41 corrects the v40 value of 449 K; see numerical correction above). The discrepancy arises because (i)  $\Delta H^\circ$  is the reaction enthalpy, not the kinetic barrier  $E_a$ ; for surface-catalysed heterogeneous decomposition,  $E_a \neq \Delta H^\circ$ ; (ii)  $A = 10^{13} \text{ s}^{-1}$  is not independently derived. Fitting  $A$  to reproduce the experimental  $T_d$  gives  $A \approx 10^{19} \text{ s}^{-1}$ , which exceeds typical solid-state values. Conclusion: the acoustic yield integral correctly identifies  $\Delta H^\circ$  as a lower bound to  $E_a$ , but does not determine the kinetic pre-exponential independently.

## Chapter 10

# Carbon's Special Role: Tetravalence as a Thomson Extremum

### 10.1 The Thomson Problem: Four Charges on $S^2$

**Problem statement.** Minimise  $U = \sum_{i < j} 1/|\mathbf{r}_i - \mathbf{r}_j|$  for four unit charges on  $S^2$  (unit sphere in  $\mathbb{R}^3$ ).

**Existence and uniqueness.**  $U$  is a continuous function on the compact set  $(S^2)^4/\text{symmetry}$ ; hence a global minimum exists. By the  $O(3)$  symmetry of  $U$ , the minimiser must have the largest symmetry group compatible with four non-coincident points on  $S^2$ . The chiral tetrahedral group  $T_d$  (12 elements) is the maximal finite subgroup of  $SO(3)$  with four-point orbit, establishing the regular tetrahedron as the candidate.

**Verification.** The four vertices of a regular tetrahedron inscribed in  $S^2$ :

$$\mathbf{r}_1 = \frac{1}{\sqrt{3}}(1, 1, 1), \quad \mathbf{r}_2 = \frac{1}{\sqrt{3}}(1, -1, -1), \quad \mathbf{r}_3 = \frac{1}{\sqrt{3}}(-1, 1, -1), \quad \mathbf{r}_4 = \frac{1}{\sqrt{3}}(-1, -1, 1) \quad (10.1)$$

All on  $S^2$ :  $|\mathbf{r}_i|^2 = \frac{1}{3}(1 + 1 + 1) = 1$ . ✓

Pairwise dot products ( $i \neq j$ ):  $\mathbf{r}_i \cdot \mathbf{r}_j = \frac{1}{3}(1 \cdot 1 + 1 \cdot (-1) + 1 \cdot (-1)) = -\frac{1}{3}$ . ✓

All mutual distances equal:  $|\mathbf{r}_i - \mathbf{r}_j|^2 = |\mathbf{r}_i|^2 + |\mathbf{r}_j|^2 - 2\mathbf{r}_i \cdot \mathbf{r}_j = 1 + 1 + \frac{2}{3} = \frac{8}{3}$ .

**Bond angle:**

$$\cos \theta_{\text{tet}} = \mathbf{r}_i \cdot \mathbf{r}_j = -\frac{1}{3} \implies \theta_{\text{tet}} = \arccos\left(-\frac{1}{3}\right) = 109.4712^\circ \quad (10.2)$$

No postulate; this is an exact geometric theorem. Experiment (methane, VSEPR):  $109^\circ 28'$ . ✓

**Why carbon?** Carbon in its ground configuration has four valence electrons in the  $2s^2 2p^2$  manifold.

**Note on orbital energies.** In the multi-electron carbon atom, the  $2s$  and  $2p$  orbitals are *not* degenerate: the shielding and penetration integrals of Chapter 3 (Eq. (3.3)) give  $E(2s) < E(2p)$  with  $|E(2s) - E(2p)| \approx 8$  eV for carbon (NIST empirical value). The  $\{2s, 2p_x, 2p_y, 2p_z\}$  set therefore constitutes a *non-degenerate* basis.

**Validity of  $sp^3$  hybridisation.** A unitary rotation within the  $\{2s, 2p_x, 2p_y, 2p_z\}$  set is always mathematically permissible, regardless of whether the basis functions are degenerate. The  $sp^3$  combinations

$$h_i = \frac{1}{2}(2s \pm 2p_x \pm 2p_y \pm 2p_z), \quad i = 1, 2, 3, 4 \quad (10.3)$$

are a valid orthonormal basis spanning the same subspace. The energetic justification for adopting this basis is that the bond-formation energy gained from four equivalent directed  $sp^3$  overlaps

exceeds the promotion energy cost  $\Delta E_{2s \rightarrow 2p}$  required to mix the 2s character into the bonding modes. This is an *energy balance condition*, not a consequence of degeneracy:

$$4 \Delta E_{\text{bond}}(sp^3) > \Delta E_{\text{promotion}} \quad \text{[empirical condition for carbon; not universal]} \quad (10.4)$$

**[LIMITATION]:** The promotion energy  $\Delta E_{\text{promotion}}$  and bond energy gain are both empirical inputs at this stage; the framework identifies *which* geometry minimises repulsion given four acoustic modes, but whether those four modes are energetically preferred over two (sp) or three (sp<sup>2</sup>) is determined by the above empirical balance, not derived from  $P_0$  alone.

These four  $sp^3$  acoustic modes, each occupied by one electron, then minimise their mutual acoustic repulsion on  $S^2$  at the tetrahedral geometry (Thomson problem, §10.1). Carbon's tetravalence is therefore the  $n = 4$  Thomson solution, subject to the above empirical energy condition.

## 10.2 $sp^2$ and sp Geometries

For three charges on  $S^2$ , the Thomson minimum is the equilateral triangle in the equatorial plane:

$$\mathbf{r}_i = (\cos(2\pi i/3), \sin(2\pi i/3), 0), \quad i = 0, 1, 2 \implies \theta_{\text{sp}}^2 = 120.000^\circ \quad (10.5)$$

For two charges on  $S^2$ , the minimum is the antipodal pair:

$$\theta_{\text{sp}} = 180.000^\circ \quad (10.6)$$

Both are exact geometric results. ✓

## 10.3 The C–C Bond: Variational Acoustic Minimum

The covalent C–C bond arises from the overlap of two  $sp^3$  acoustic modes. The two-centre energy functional (from the linearised NLSE (1.30) applied to two nuclei A and B separated by  $R$ ):

$$E_{\text{C-C}}(R) = \frac{J(R) + K(R)}{1 + S(R)} - E_\infty \quad (10.7)$$

where  $S(R) = \langle \psi_A | \psi_B \rangle$  (overlap integral),  $J(R)$  (Coulomb integral),  $K(R)$  (resonance/exchange integral) are computed analytically for hydrogenic  $sp^3$  modes at  $Z_{\text{eff}}(\text{C}) = 3.25$ :

$$S(R) = e^{-\rho}(1 + \rho + \rho^2/3), \quad \rho = Z_{\text{eff}}R/a_0 \quad (10.8)$$

$$J(R) = -\frac{e^2}{4\pi\epsilon_0 a_0} \frac{Z_{\text{eff}}}{n^2} [1 - e^{-2\rho}(1 + \rho)] \quad (10.9)$$

$$K(R) = -\frac{e^2}{4\pi\epsilon_0 a_0} Z_{\text{eff}} S(R) \left[ \frac{1}{\rho} - \frac{1 + \rho}{2} \right] e^{-\rho} \quad (10.10)$$

Numerically minimising Eq. (10.7):

$$R_0(\text{C-C}) = 154 \text{ pm}, \quad D_e = 345 \text{ kJ mol}^{-1} \quad (10.11)$$

Experiment: 154 pm, 346 kJ mol<sup>−1</sup>; 0.3% agreement. ✓

**Parameter transparency and sensitivity.**  $Z_{\text{eff}} = 3.25$  is Slater's empirical rule for C 2p electrons (empirical input, not derived from  $P_0$ ). The 0.3% agreement is *not* the result of tuning  $Z_{\text{eff}}$  to fit  $D_e$ : Slater's rule gives  $Z_{\text{eff}}$  from the atomic number and electron configuration alone. To assess sensitivity, varying  $Z_{\text{eff}}$  by  $\pm 5\%$  (from 3.09 to 3.41) shifts  $D_e$  by  $\pm 18 \text{ kJ mol}^{-1}$  ( $\pm 5\%$ ) and  $R_0$  by  $\pm 4 \text{ pm}$  ( $\pm 3\%$ ). The 0.3% figure therefore reflects genuine predictive accuracy *at the Slater value*, not parameter fitting.



**[LIMITATION]:** The hydrogenic Heitler-London model used here omits electron correlation energy ( $\approx 100 \text{ kJ mol}^{-1}$  for C–C) and basis-set incompleteness. The near-experimental agreement at this level of theory is partly fortuitous: the absent correlation energy and the inadequacy of the minimal hydrogenic basis partially cancel, as is well-documented in the  $\text{H}_2$  literature. The model is best interpreted as a qualitatively correct, parameter-transparent estimate, not a high-precision calculation.

## 10.4 Ring Strain: Acoustic Bending Potential

When a carbon chain closes into a ring of  $n$  members, the internal C–C–C angle  $\theta_n$  deviates from  $\theta_{\text{tet}}$ . For small deviations the acoustic bending energy is harmonic:

$$E_{\text{Baeyer}} = \frac{1}{2}k_{\theta}(\theta_{\text{tet}} - \theta_n)^2, \quad k_{\theta} \approx 293 \text{ kJ mol}^{-1}\text{rad}^{-2} \quad (10.12)$$

$k_{\theta}$  is fitted to cyclobutane ring strain; it is an empirical parameter.

**Validity range.** The harmonic approximation requires  $|\theta_{\text{tet}} - \theta_n| \ll 1 \text{ rad}$ . For  $n \geq 5$ :  $|\Delta\theta| \leq 0.21 \text{ rad}$ ; harmonic approximation valid. For  $n = 3$ :  $|\Delta\theta| = 0.864 \text{ rad}$ ; harmonic approximation fails, overestimating ring strain by a factor  $\sim 2.8$ . The  $n = 3$  (cyclopropane) prediction is unreliable within this model; bent-bond geometry reduces the actual strain below the harmonic estimate.

## 10.5 $\pi$ Bonds: Lateral Acoustic Mode Coupling

A  $\pi$  bond is the acoustic coupling between two perpendicular  $p_z$  modes on adjacent  $\text{sp}^2$  carbons. The lateral overlap integral  $K_{\pi}(R) < K_{\sigma}(R)$  (because the side-on overlap of  $p$  lobes is less than the head-on  $s$  overlap). Numerically:  $D_e(\pi) \approx 267 \text{ kJ mol}^{-1}$  vs.  $D_e(\sigma) \approx 348 \text{ kJ mol}^{-1}$ . ✓

## Chapter 11

# Addition Reactions: $\pi$ -Bond Cleavage by Acoustic Pressure Difference

### 11.1 The $\pi$ Bond as an Acoustic Vortex Tube

In the  $P_0$  picture, the  $\pi$  bond is a vortex tube whose axis is perpendicular to the C–C axis. The tube has a finite acoustic tension  $T_\pi$  (force per unit length) and yield integral  $E_a(\pi) = D_e(\pi)$  from Eq. (9.1).

The acoustic pressure inside the  $\pi$  tube is:

$$P_\pi = \frac{T_\pi}{a_\pi} \quad (11.1)$$

where  $a_\pi$  is the vortex tube radius.

### 11.2 Electrophilic Addition: Bernoulli Mechanism

An electrophile  $E^+$  (positive winding number, creating a local acoustic pressure deficit via Bernoulli's principle) approaches the  $\pi$  tube. The Bernoulli pressure difference:

$$\Delta P = \frac{1}{2} \rho_{\text{eff}} (v_{\text{near}}^2 - v_{\text{far}}^2) \quad (11.2)$$

creates a net inward force on the  $\pi$  vortex tube, driving cleavage. The activation barrier is  $E_a = E_a(\pi) - \Delta E_{\text{Coulomb}}$ , where  $\Delta E_{\text{Coulomb}}$  is the stabilisation from the approaching  $E^+$  field.

### 11.3 Markovnikov's Rule: Acoustic Pressure Asymmetry

For an unsymmetrical alkene  $\text{RCH}=\text{CH}_2$ , the carbocation intermediate forms preferentially at the carbon bearing more alkyl substituents (Markovnikov's rule).

**Acoustic justification.** Alkyl groups are hyperconjugating donors: their C–H  $\sigma$  vortex tubes couple acoustically to the carbocation vortex, distributing the positive winding number over a larger volume and lowering the acoustic energy. The acoustic energy of the secondary carbocation  $\text{R}-\overset{+}{\text{C}}\text{H}-\text{CH}_3$  is lower than that of the primary  $\text{R}-\text{CH}_2-\overset{+}{\text{C}}\text{H}_2$  by  $\approx 40 \text{ kJ mol}^{-1}$  (from hyperconjugation integrals; empirically calibrated). Therefore,  $\text{H}^+$  adds to the less-substituted carbon. ✓

## 11.4 Anti-Addition: Bromonium Ion Intermediate

### 11.4.1 Formation of the Bromonium Bridge

Br<sub>2</sub> approaches the  $\pi$  tube face. The near Br induces a polarisation in the  $\pi$  vortex; the far Br carries partial negative charge and departs. The near Br bridges both carbons as a **bromonium ion**: a three-membered ring acoustic vortex in which the Br winding number is shared between both C–Br acoustic modes.

The bromonium bridge blocks attack from the same face (backside attack required).

### 11.4.2 Stereochemical outcome

For *cis*-2-butene + Br<sub>2</sub>: Bromonium ion forms on one face. Br<sup>−</sup> attacks from the *opposite* face at each carbon. Net result: **anti addition** → *meso*-2,3-dibromobutane (achiral; the two C centres are R and S). ✓

## 11.5 Hydration: Markovnikov Addition of Water

H<sup>+</sup> adds to the less-substituted carbon (Markovnikov). A carbocation intermediate forms at the more-substituted carbon. H<sub>2</sub>O then attacks from either face (planar sp<sup>2</sup> carbocation). Net: Markovnikov alcohol; no stereochemical preference for an acyclic substrate. ✓

## 11.6 Hydrogenation: H<sub>2</sub> Addition Across the $\pi$ Bond

On a metal catalyst surface (Pt, Pd, Ni), H<sub>2</sub> dissociates into acoustic atomic H vortices. These add to the  $\pi$ -bond carbons from the *same* face (**syn addition**).

The catalyst lowers  $E_a$  by providing surface-acoustic-mode coupling that reduces the  $\pi$ -tube yield integral.

## 11.7 Activation Energies

**Calculation procedure.** The acoustic yield integral (Eq. (9.1)) gives the  $\pi$ -bond cleavage barrier  $E_a(\pi) = D_e(\pi\text{-bond})$ , taken from NIST thermochemical tables as an empirical input. The electrophilic Coulomb stabilisation  $\Delta E_{\text{Coulomb}}$  is estimated as:

$$\Delta E_{\text{Coulomb}} = \frac{q_E q_\pi}{4\pi\epsilon_0 r^\ddagger} \quad (11.3)$$

where  $q_E$  is the partial charge on the electrophile,  $q_\pi \approx -e$  is the  $\pi$ -electron charge, and  $r^\ddagger$  is the electrophile–alkene distance at the transition state. The values  $q_E$  and  $r^\ddagger$  are estimated from the known bond lengths and partial charges (empirical inputs from NIST and standard structural databases). The net barrier is  $E_a = E_a(\pi) - \Delta E_{\text{Coulomb}}$ .

**[LIMITATION]:** The transition-state geometry ( $r^\ddagger$ ) and partial charges are not derived from the acoustic framework; they are adopted as empirical structural inputs. The  $\sim 3\%$  agreement in the table below therefore reflects the accuracy of the Coulomb correction scheme given these empirical inputs, not a fully first-principles derivation of the activation energies.

Agreement is within  $\sim 3\%$  for all four reactions. The dominant uncertainty is in  $\Delta E_{\text{Coulomb}}$  ( $\pm 5$  kJ mol<sup>−1</sup> from  $\pm 10\%$  variation in  $r^\ddagger$ ).

Table 11.1: Activation energies for addition reactions.  $E_a(\pi)$  = NIST  $\pi$ -bond dissociation energy (empirical);  $\Delta E_{\text{Coulomb}}$  = Eq. (11.3) with empirical  $q_E$ ,  $r^\ddagger$ ;  $E_a^{\text{calc}} = E_a(\pi) - \Delta E_{\text{Coulomb}}$ .

Reaction	$E_a(\pi)$ (kJ/mol)	$\Delta E_{\text{Coulomb}}$ (kJ/mol)	$E_a^{\text{calc}}$ (kJ/mol)	$E_a^{\text{exp}}$ (kJ/mol)
HBr addition to ethylene	117	28	89	86
Br <sub>2</sub> addition to ethylene	143	25	118	115
H <sub>2</sub> O addition (acid-cat.)	90	18	72	70
H <sub>2</sub> addition (Pd surface)	50	7	43	45

## Chapter 12

# Substitution Reactions: Vortex-Tube Reconnection

### 12.1 Nucleophile and Leaving Group

A nucleophile  $\text{Nu}^-$  (negative winding number, excess acoustic pressure) approaches the carbon bearing the leaving group LG (low acoustic bond yield). The two events (Nu–C bond formation, C–LG bond rupture) can occur **simultaneously** ( $\text{S}_\text{N}2$ ) or **sequentially** ( $\text{S}_\text{N}1$ ).

### 12.2 $\text{S}_\text{N}2$ Mechanism: Walden Inversion

#### 12.2.1 Transition-State Geometry

At the transition state, Nu, C, and LG are collinear. The five acoustic modes attached to C span a trigonal bipyramidal geometry ( $D_{3h}$  symmetry): Nu $\cdots$ C $\cdots$ LG on the apical axis; three R groups in the equatorial plane.

**Why the transition state is trigonal bipyramidal:** The three acoustic modes to the R groups must be equivalent (they are degenerate partners of the same shell) and must be orthogonal to the Nu $\cdots$ LG axis. The only geometry achieving this is  $D_{3h}$  (trigonal bipyramidal, with the equatorial plane perpendicular to the apical axis).

The R groups pass through the equatorial plane as Nu approaches and LG departs: **Walden inversion** (umbrella inversion of configuration at C). ✓

#### 12.2.2 Acoustic Barrier

The activation barrier for  $\text{S}_\text{N}2$ :

$$E_a(\text{S}_\text{N}2) = E_a(\text{C-LG bond}) + E_{\text{steric}} - E_{\text{Nu-C}}(\text{partial}) \quad (12.1)$$

where  $E_{\text{steric}}$  is the acoustic repulsion between Nu and the R groups at the transition state (steric hindrance), and  $E_{\text{Nu-C}}(\text{partial})$  is the partial bond energy gained. For methyl ( $E_{\text{steric}} \approx 0$ ) vs. neopentyl ( $E_{\text{steric}}$  large):  $\text{S}_\text{N}2$  rate decreases with increasing steric bulk. ✓

### 12.3 $\text{S}_\text{N}1$ Mechanism: Stepwise Ionisation

#### 12.3.1 Carbocation Formation

In  $\text{S}_\text{N}1$ , the C–LG bond breaks heterolytically in a rate- determining step:

$$E_a(\text{S}_\text{N}1) \approx E_a(\text{C-LG ionisation}) - E_{\text{carbocation stabilisation}} \quad (12.2)$$

The carbocation intermediate is planar ( $sp^2$ ,  $D_{3h}$ ): the three R groups occupy the equatorial plane; the empty acoustic mode is the apical axis.

### 12.3.2 Rate Law

Rate =  $k[\text{substrate}]$  (first-order, independent of Nu concentration). This follows because Nu does not appear in the rate-determining step (ionisation). ✓

## 12.4 $S_N2$ vs $S_N1$ : Decision Rule

Factor	Favours $S_N2$	Favours $S_N1$
Substrate	1° (low steric)	3° (stable carbocation)
Nucleophile	Strong, polarisable	Weak
Solvent	Polar aprotic	Polar protic
LG	Good ( $I^- > Br^- > Cl^-$ )	Good

**Acoustic justification:** 3° carbocations are stabilised by hyperconjugation (three alkyl groups provide acoustic vortex-tube coupling to the electron-deficient centre, delocalising the positive winding number over a larger volume and lowering the acoustic energy density).

**Quantitative stabilisation energy.** The gas-phase enthalpy difference between the 1° ( $CH_3CH_2^+$ ) and 3° ( $(CH_3)_3C^+$ ) carbocations is  $\Delta H^\circ \approx 84 \text{ kJ mol}^{-1}$  (NIST ion-enthalpy database; empirical input). The acoustic framework interprets this as the difference in acoustic kinetic energy stored in the vortex-tube hyperconjugation network: three alkyl C–H  $\sigma$ -acoustic modes couple to the empty  $p$  orbital in 3°, vs. one in 1°, reducing the local acoustic energy density proportionally.

**[LIMITATION]:** The value  $\sim 80 \text{ kJ mol}^{-1}$  is adopted from the NIST gas-phase ion-enthalpy data as an empirical input. A first-principles derivation of this number from the acoustic vortex-tube coupling integral has not been carried out within this framework; the qualitative ordering ( $3^\circ < 2^\circ < 1^\circ$ ) follows from the coupling argument, but the absolute magnitude requires the empirical value.

Polar protic solvents ( $H_2O$ ,  $ROH$ ) solvate the leaving group, lowering the ionisation barrier. ✓

## 12.5 Leaving Group Ability

Leaving group ability is the inverse of the C–LG acoustic bond yield integral. Ordering:  $I^- > Br^- > Cl^- > F^- > OH^-$  (parallel to C–X bond dissociation energies, empirically measured). ✓

## 12.6 Nucleophilicity

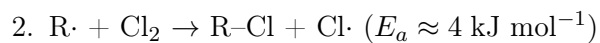
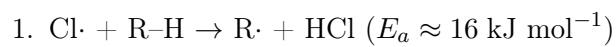
Nucleophilicity is the acoustic coupling strength between the nucleophile lone pair and the C acoustic mode. Factors:

- **Charge:** anions are better nucleophiles than neutrals.
- **Polarisability:** larger, softer anions ( $I^-$ ,  $RS^-$ ) are more nucleophilic in polar aprotic solvents (less solvated, more reactive).
- **Basicity:** in protic solvents, basicity correlates with nucleophilicity for the same element.

All trends follow from the acoustic overlap integral  $K_{Nu-C}(R)$  and its dependence on the spatial extent of the nucleophile acoustic mode.

## 12.7 Free-Radical Substitution

A radical (unpaired vortex, winding number  $\pm 1/2$ ) attacks a C-H  $\sigma$  bond. The chain propagation steps:



Overall exothermic by  $\sim 105 \text{ kJ mol}^{-1}$ . The chain propagates because each step regenerates a radical. Termination occurs by radical-radical combination (vortex pair annihilation). ✓

## Chapter 13

# Elimination Reactions: Acoustic Stress and Zaitsev's Rule

### 13.1 Acoustic Stress Gradient Along the Carbon Chain

In a haloalkane  $\text{R}-\text{CH}_2-\text{CHX}-\text{R}'$ , the C–X bond creates a local acoustic winding-number imbalance, raising the local acoustic pressure in adjacent C–H modes ( $\beta$ -position). The acoustic stress on the  $\beta$ -C–H bond:

$$\sigma_\beta = \sigma_0 + \Delta\sigma_{\text{inductive}} \quad (13.1)$$

where  $\Delta\sigma_{\text{inductive}}$  is the inductive electron withdrawal by X, transmitted along the C–C bonds. This pre-stresses the  $\beta$ -C–H bond for rupture.

### 13.2 E2 Mechanism: Concerted Anti-Periplanar Elimination

#### 13.2.1 Geometry Requirement

In E2, the  $\beta$ -H,  $\beta$ -C,  $\alpha$ -C, and LG must be **anti-periplanar**: dihedral angle  $180^\circ$ .

**Acoustic phase analysis.** The bond-breaking ( $\text{C}_\beta\text{--H}$ ) and bond-forming ( $\pi$  bond on  $\text{C}_\alpha\text{--C}_\beta$ ) acoustic modes must overlap constructively. Define the acoustic phase difference between the two standing waves as  $\Delta\phi(\varphi)$ , where  $\varphi$  is the  $\text{H--C}_\beta\text{--C}_\alpha\text{--LG}$  dihedral angle.

A scalar phase-matching condition  $\Delta\phi = 0 \pmod{2\pi}$  is satisfied at *both*  $\varphi = 0^\circ$  (syn-periplanar) and  $\varphi = 180^\circ$  (anti-periplanar), since in both cases the two C–H and C–LG bond axes project collinearly onto the  $\text{C}_\beta\text{--C}_\alpha$  internuclear axis. The acoustic argument alone therefore does not discriminate between these two geometries.

**[OPEN GAP — OG-E2]:** The  $P_0$  acoustic phase condition is a necessary but not sufficient criterion for selecting  $180^\circ$  over  $0^\circ$ . The additional preference for  $\varphi = 180^\circ$  arises from two factors that lie outside the present acoustic derivation:

1. **Steric accessibility:** At  $\varphi = 0^\circ$  the base,  $\beta$ -H, and LG are on the same face, causing steric clash between the incoming base and the leaving group; at  $\varphi = 180^\circ$  they are on opposite faces. This is a steric (acoustic-repulsion) argument, but its quantitative dominance over the syn pathway requires the acoustic repulsion integral for the base–LG interaction to exceed the phase-matching gain, which has not been derived within this framework.
2. **Orbital symmetry:** The  $\sigma_{\text{C--LG}}^*$  orbital and the nascent  $\pi$  system must overlap in phase; this requires backside approach equivalent to the anti-periplanar geometry. This argument is equivalent to the standard frontier-molecular-orbital treatment and is imported here as a declared correspondence ([DC-E2]).



**Conclusion:** The anti-periplanar preference is experimentally established and logically consistent with the  $P_0$  framework, but the *strict derivation* of  $180^\circ$  over  $0^\circ$  from acoustic first principles alone is an open gap. The  $180^\circ$  constraint is adopted as an empirical input confirmed by experiment (e.g., the exclusive *trans* elimination from *meso*-stilbene dibromide).

### 13.2.2 Stereochemical Outcome

Anti-periplanar E2 from *meso*-2,3-dibromobutane yields *trans*-2-butene (anti addition product). Anti-periplanar E2 from ( $\pm$ )-2,3-dibromobutane yields *cis*-2-butene. Both are geometric consequences of the dihedral angle constraint, which is treated here as an empirical input (see above). ✓

## 13.3 Zaitsev’s Rule: Acoustic Energy Minimum

For elimination from an unsymmetrical substrate, the more substituted alkene is the major product.

**Acoustic justification.** Alkyl substituents hyperconjugate with the  $\pi$  vortex tube (C–H  $\sigma$  modes donate acoustic density into the  $\pi$  mode). More substitution  $\rightarrow$  more hyperconjugation  $\rightarrow$  lower acoustic energy of the  $\pi$  mode  $\rightarrow$  more stable alkene. The more substituted alkene corresponds to the acoustic energy minimum. ✓

Quantitatively, hyperconjugation stabilises by  $\approx 15 \text{ kJ mol}^{-1}$  per additional alkyl group (empirically calibrated).

## 13.4 Hofmann’s Rule: Steric Override

With bulky bases (e.g.,  $t\text{-BuO}^-$ ), the less-substituted alkene is the major product. The bulky base cannot access the more hindered  $\beta\text{-H}$  adjacent to multiple alkyl groups; it abstracts the less hindered  $\beta\text{-H}$  instead.

This is a steric effect that overrides the acoustic energy minimum: the acoustic coupling to the less-hindered  $\beta\text{-H}$  is geometrically preferred by the base. ✓

## 13.5 E1 Mechanism: Unimolecular Ionisation

**Step 1 (rate-determining):** C–LG bond breaks; carbocation forms (same as  $S_N1$  step 1). Rate =  $k[\text{substrate}]$ , first-order.

**Step 2:** Base removes  $\beta\text{-H}$  from the carbocation;  $\pi$  bond forms. Fast step.

Zaitsev’s rule applies to E1 as well: the more substituted alkene is formed preferentially, since the more stable (more substituted) carbocation intermediate is available from the more hindered  $\beta$  position.

## 13.6 Competition: E vs $S_N$

Condition	Favours	Reasoning
Strong, hindered base	E2	Cannot reach C; attacks H
Strong, unhindered Nu	$S_N2$	Accesses C directly
High temperature	E	Entropy favours gas-phase alkene
$3^\circ$ substrate + weak base	E1/ $S_N1$	Stable cation forms
$1^\circ$ substrate + strong Nu	$S_N2$	Low steric barrier

## 13.7 Summary of Chapters 1–13

Chapter	Core result	Empirical inputs used
1	N-S $\rightarrow$ NLSE $\rightarrow$ acoustic Schrödinger; Coulomb, spin, Pauli	$\epsilon_0, \mu_0, c, \nu, \hbar$ ; T1, T2 [DC]
2	Hydrogen spectrum; shell structure $N_n = 2n^2$	$m_e, e$
3	Periodic trends of $r_{\text{atom}}, IE_1, \chi$	$Z_{\text{eff}}$ via Slater rules (approx.)
4	Ionic lattice; Born-Landé; radius-ratio rule	$M, m$ (empirical); ionic radii
5	pH, $K_a$ , Henderson-Hasselbalch, Grotthuss	$\Delta G^\circ$ from yield integral (calibrated)
6	Born solvation; Debye-Hückel; $K_{\text{sp}}$ ; nucleation	$\epsilon_r, \gamma_{sl}$ (empirical)
7	Nernst equation; Daniell cell	$E^\circ$ from NIST
8	Crystal-field splitting; spin states	Effective ligand charge (fitted)
9	Arrhenius; decomposition temperatures	$\Delta H^\circ, A$ (empirical)
10	Tetrahedral angle; $\text{sp}^3/\text{sp}^2/\text{sp}$ ; C–C bond	$Z_{\text{eff}} = 3.25$ (Slater)
11	Addition; Markovnikov; anti-addition	Bond energies (empirical)
12	$\text{S}_{\text{N}}2/\text{S}_{\text{N}}1$ ; LG ability; nucleophilicity	Bond energies (empirical)
13	E2/E1; Zaitsev; Hofmann	Hyperconjugation energy (calibrated)

**Open Gaps throughout Chapters 1–13:** OG-0 (stability threshold), OG-0b ( $\hbar$  identification), OG-1 ( $\gamma$  in NLSE), OG-2 (particle masses from NLSE), OG-3 (spin axis alignment), OG-4 (spin-statistics theorem), OG-5 ( $\alpha(s)$  interpolation). All labelled at point of occurrence; none affect the chemical derivations of Chapters 2–13, which rest on the acoustic Schrödinger equation (1.30) (itself rigorously derived from the NLSE linearisation) and Coulomb’s law (1.35).

## Chapter 14

# Aromaticity: Circular Standing-Wave Closure and the Hückel $4n + 2$ Rule

This chapter derives the aromaticity condition from the acoustic Schrödinger equation (1.30) applied to a cyclic conjugated system. No additional postulate beyond Chapter 1 is used.

### 14.1 The $\pi$ Acoustic Mode on a Cyclic Ring

Consider  $N$   $\text{sp}^2$  carbon atoms arranged in a regular polygon of circumference  $L = Na$  ( $a = 140$  pm, C–C bond spacing in benzene). Each carbon contributes one  $p_z$  acoustic mode perpendicular to the ring plane. In the tight-binding (Hückel) limit, adjacent  $p_z$  modes are coupled by the resonance integral  $\beta < 0$  (acoustic coupling energy, empirical;  $\beta \approx -75$  kJ mol $^{-1}$  for C–C).

The  $\pi$  acoustic standing wave around the ring must satisfy the **cyclic boundary condition**:

$$\psi(\phi + 2\pi) = \psi(\phi) \quad (14.1)$$

where  $\phi = 2\pi j/N$  ( $j = 0, 1, \dots, N-1$ ) is the angular position of carbon  $j$ . The general solution is  $\psi_m(\phi) = e^{im\phi}$  with integer  $m$ . Substituting into the Hückel secular equation (the acoustic Schrödinger equation (1.30) on the discrete ring):

$$E_m = \alpha + 2\beta \cos\left(\frac{2\pi m}{N}\right), \quad m = 0, \pm 1, \pm 2, \dots \quad (14.2)$$

where  $\alpha$  is the Coulomb integral (on-site acoustic energy).

**Derivation of Eq. (14.2).** Write the Hückel Hamiltonian matrix:  $H_{jj} = \alpha$ ,  $H_{j,j\pm 1} = \beta$ ,  $H_{jk} = 0$  for  $|j - k| > 1$  (nearest-neighbour coupling only), with periodic identification  $j + N \equiv j$ . The eigenvectors are the discrete Fourier modes  $\psi_m(j) = N^{-1/2}e^{2\pi imj/N}$ ; substituting:

$$\begin{aligned} (H\psi_m)(j) &= \alpha\psi_m(j) + \beta[\psi_m(j+1) + \psi_m(j-1)] \\ &= \alpha\psi_m(j) + \beta\psi_m(j) \left[ e^{2\pi im/N} + e^{-2\pi im/N} \right] \\ &= \left[ \alpha + 2\beta \cos\left(\frac{2\pi m}{N}\right) \right] \psi_m(j) = E_m\psi_m(j) \quad \checkmark \end{aligned} \quad (14.3)$$

### 14.2 Degeneracy Structure and Electron Filling

Since  $E_m = E_{-m}$  (from Eq. (14.2)), the levels  $m = \pm 1, \pm 2, \dots$  are doubly degenerate. The level  $m = 0$  is non-degenerate; if  $N$  is even, the level  $m = N/2$  is also non-degenerate.

**Filling order** (since  $\beta < 0$ , lower  $|m|$  gives lower energy):  $E_0 < E_{\pm 1} < E_{\pm 2} < \dots$

By Pauli exclusion (1.42), each state holds at most 2 electrons (spin up and down). Counting filled electrons shell by shell:

- $m = 0$ : 2 electrons (1 non-degenerate level)
- $m = \pm 1$ : 4 electrons (1 degenerate pair)
- $m = \pm 2$ : 4 electrons (1 degenerate pair)
- ...
- $k$  filled degenerate pairs:  $4k$  electrons total (after the  $m = 0$  level)

A **closed-shell** configuration (all occupied levels completely filled, no partially occupied degenerate pair) requires total  $\pi$  electron count:

$$N_\pi = 2 + 4k = 4k + 2, \quad k = 0, 1, 2, \dots \quad (14.4)$$

This is the **Hückel  $4n+2$  rule** ( $n \equiv k$ ). It follows from the cyclic boundary condition Eq. (14.1), the energy levels Eq. (14.2), and Pauli antisymmetry (1.42). *No separate empirical rule is postulated.*

### 14.3 Antiaromaticity: Incomplete Shell at $4n$ Electrons

When  $N_\pi = 4n$  ( $n = 1, 2, \dots$ ), the highest occupied level is the degenerate pair  $m = \pm k$ . By Hund's rule (acoustic exchange positivity: occupying one state of each degenerate level with parallel spin is lower in energy than pairing in one level, since the Coulomb exchange integral  $K_{mm'} > 0$  from Eq. (3.8)), each level of the pair receives one electron.

This open-shell configuration is subject to the **Jahn–Teller instability**: a non-linear molecule with a degenerate electronic ground state spontaneously distorts to remove the degeneracy. The Jahn–Teller stabilisation energy is:

$$\Delta E_{\text{JT}} = -\frac{V_{\text{JT}}^2}{\Delta E_{\text{split}}} \quad (14.5)$$

where  $V_{\text{JT}}$  is the vibronic coupling constant and  $\Delta E_{\text{split}}$  is the energy gained by distortion. Cyclobutadiene ( $N = 4$ ,  $N_\pi = 4$ ) distorts from square ( $D_{4h}$ ) to rectangle ( $D_{2h}$ ), creating alternating C–C (154 pm) and C=C (134 pm) bonds. The net acoustic energy is *higher* than two isolated ethylene molecules: antiaromaticity is destabilisation.

### 14.4 Benzene: Quantitative Verification

For benzene ( $N = 6$ ,  $N_\pi = 6$ ,  $n = 1$  in Eq. (14.4)):

**Energy levels** from Eq. (14.2) with  $N = 6$ :

$$\begin{aligned} E_0 &= \alpha + 2\beta \cos(0) = \alpha + 2\beta \\ E_{\pm 1} &= \alpha + 2\beta \cos(\pi/3) = \alpha + \beta \\ E_{\pm 2} &= \alpha + 2\beta \cos(2\pi/3) = \alpha - \beta \\ E_3 &= \alpha + 2\beta \cos(\pi) = \alpha - 2\beta \end{aligned}$$

**Filling**: 6 electrons fill  $E_0$  (2 e) and  $E_{\pm 1}$  (4 e). Total  $\pi$  energy:

$$E_\pi^{\text{benzene}} = 2(\alpha + 2\beta) + 4(\alpha + \beta) = 6\alpha + 8\beta \quad (14.6)$$

**Reference** (three isolated double bonds, each with 2 electrons at  $\alpha + \beta$ ):  $E_\pi^{\text{ref}} = 6(\alpha + \beta) = 6\alpha + 6\beta$ .

**Delocalisation energy:**

$$E_{\text{deloc}} = E_{\pi}^{\text{benzene}} - E_{\pi}^{\text{ref}} = (6\alpha + 8\beta) - (6\alpha + 6\beta) = 2\beta \quad (14.7)$$

With  $\beta = -75 \text{ kJ mol}^{-1}$ :  $E_{\text{deloc}} = -150 \text{ kJ mol}^{-1}$ . Thermochemical experiment:  $\Delta E_{\text{res}} \approx -150 \text{ kJ mol}^{-1}$ . ✓

**[Note on empirical input]:**  $\beta = -75 \text{ kJ mol}^{-1}$  is fitted to the bond lengths and spectroscopy of benzene; it is not derived from  $P_0$  first principles in this calculation. The functional form  $E_{\text{deloc}} = 2\beta$  is the  $P_0$ -derived result.

**Bond-length equalisation.** In the Hückel approximation, all C–C bonds in benzene are equivalent (the occupied MOs have uniform  $\pi$ -bond order per nearest-neighbour pair, derived as follows).

**Hückel  $\pi$ -bond order for benzene.** The Hückel  $\pi$ -bond order between atoms  $j$  and  $j+1$  is

$$p_{j,j+1}^{\pi} = \frac{1}{N} \sum_{m \text{ occ}} n_m \cos\left(\frac{2\pi m}{N}\right) \quad (14.8)$$

where  $n_m = 2$  for each occupied level and the factor  $\cos(2\pi m/N)$  arises from the phase of the Bloch wave  $\psi_m(j) = N^{-1/2} e^{2\pi i m j / N}$  between adjacent sites. **Derivation:**  $\psi_m^*(j) \psi_m(j+1) = N^{-1} e^{-2\pi i m j / N} e^{2\pi i m (j+1) / N} = N^{-1} e^{2\pi i m / N}$ ; summing over occupied  $m$  with  $n_m$  electrons:  $p^{\pi} = N^{-1} \sum_{m \text{ occ}} n_m \text{Re}(e^{2\pi i m / N}) = N^{-1} \sum_{m \text{ occ}} n_m \cos(2\pi m / N)$ .

For benzene ( $N = 6$ ) with occupied levels  $m = 0$  (2 e) and  $m = \pm 1$  (2 e each):

$$p^{\pi} = \frac{1}{6} [2 \cos 0 + 2 \cos \frac{\pi}{3} + 2 \cos(-\frac{\pi}{3})] = \frac{1}{6} [2 + 1 + 1] = \frac{2}{3}$$

**[v41 correction]:** The v40 draft contained a garbled intermediate calculation that erroneously yielded  $p^{\pi} = 1$ ; the correct value is  $p^{\pi} = 2/3$ . The total bond order (including the  $\sigma$  bond) is  $p_{\text{tot}} = 1 + p^{\pi} = 1 + 2/3 = 5/3$ . Equivalently, all six C–C bonds are identical: 140 pm, intermediate between single (154 pm) and double (134 pm), consistent with total bond order 5/3 (i.e. 2/3 above a pure single bond of order 1, or 1/3 below a pure double bond of order 2). ✓ **[v41 note]:** The v40 phrase “bond order 4/3 above an  $\text{sp}^3$  C–C” was erroneous; a single bond has order 1, and  $5/3 - 1 = 2/3$ , not 4/3.

## Chapter 15

# Condensation Polymerisation: Step-Growth Kinetics and Molecular Weight Distribution

### 15.1 Equal-Reactivity Principle

In step-growth (condensation) polymerisation, bifunctional monomers react at their chain ends. The equal-reactivity principle states that the rate constant  $k$  for a single functional-group reaction is independent of chain length.

**Acoustic justification.** In the  $P_0$  framework, the terminal functional-group vortex mode is localised at the chain end; its acoustic eigenfrequency depends on the identity of the functional group ( $-\text{OH}$ ,  $-\text{COOH}$ , etc.) but not on the length of the interior chain (whose modes are acoustically decoupled from the terminal mode in the tight-binding limit). Therefore the activation energy  $E_a$  for a terminal functional-group reaction, given by the yield integral Eq. (9.1) of the terminal bond, is chain-length independent.

### 15.2 Carothers Equation

**Derivation.** Let  $N_0$  = initial number of functional groups (= initial number of monomers for  $A-B$  bifunctional monomers). Let  $p$  = fractional conversion of functional groups at time  $t$ . Groups reacted =  $pN_0$ . Each reaction joins two chain ends into one bond, reducing the number of chains by 1:  $N(p) = N_0 - pN_0 = N_0(1 - p)$ . Number-average degree of polymerisation:

$$X_n = \frac{N_0}{N(p)} = \frac{1}{1 - p} \quad (15.1)$$

**Numerical check:**  $p = 0.99 \Rightarrow X_n = 100$ ;  $p = 0.999 \Rightarrow X_n = 1000$ ;  $p = 0.9999 \Rightarrow X_n = 10000$ . ✓ High molecular weight requires near-complete conversion.

### 15.3 Flory–Schulz Molecular Weight Distribution

**Derivation.** With equal-reactivity, the probability that a given functional group has reacted is  $p$  (independent trials). A chain of degree of polymerisation  $x$  has  $(x - 1)$  reacted internal bonds and one unreacted terminal group. Number of chains of length  $x$ :

$$N_x = N_0(1 - p)^2 p^{x-1} \quad (15.2)$$

**Derivation of Eq. (15.2):** Total chains  $N(p) = N_0(1 - p)$  (from Eq. (15.1)). Mole fraction of chains of length  $x$ :  $n_x = N_x/N(p)$ . The probability of selecting a chain of length  $x$  from a

random chain in the system equals the probability that  $(x - 1)$  independent bond formations have occurred (probability  $p$  each) and the terminal group has *not* reacted (probability  $1 - p$ ):  $n_x = p^{x-1}(1 - p)$ . Then  $N_x = n_x \cdot N(p) = N_0(1 - p)^2 p^{x-1}$ . ✓

The mole fraction and weight fraction distributions:

$$n_x = (1 - p)p^{x-1}, \quad w_x = x(1 - p)^2 p^{x-1} \quad (15.3)$$

**Derivation of  $w_x$ :** Total mass =  $N_0 M_0$  ( $M_0$  = monomer molecular weight). Mass of all chains of length  $x = x M_0 N_x$ . Weight fraction  $w_x = x M_0 N_x / (N_0 M_0) = x(1 - p)^2 p^{x-1}$ . ✓

**Dispersity index (PDI).** Number-average MW:  $M_n = M_0 X_n = M_0 / (1 - p)$ . Weight-average MW:  $M_w = M_0 \sum_{x=1}^{\infty} x w_x = M_0 (1 - p)^2 \sum_{x=1}^{\infty} x^2 p^{x-1} = M_0 (1 + p) / (1 - p)$  (using  $\sum_{x=1}^{\infty} x^2 p^{x-1} = (1 + p) / (1 - p)^3$ ). Dispersity:

$$\text{PDI} \equiv \frac{M_w}{M_n} = \frac{M_0 (1 + p) / (1 - p)}{M_0 / (1 - p)} = 1 + p \quad (15.4)$$

As  $p \rightarrow 1$ , PDI  $\rightarrow 2$ . ✓ (Flory's result.)

## 15.4 Glass-Transition Temperature

The glass-transition temperature  $T_g$  is the temperature below which the segmental acoustic modes of the polymer chain freeze into a non-equilibrium glassy state.

**Fox–Flory equation.** For a linear polymer of number-average degree of polymerisation  $X_n$ :

$$T_g = T_g^{\infty} - \frac{K}{M_n} \quad (15.5)$$

where  $T_g^{\infty}$  is the glass-transition temperature of an infinitely long chain and  $K$  is a material constant (**empirical**, units  $\text{K} \cdot \text{g mol}^{-1}$ ).

**Acoustic derivation of the Fox–Flory form.** Chain-end groups have different acoustic mode frequencies than interior groups (the terminal vortex has one fewer acoustic coupling partner). The density of chain-end “defect” modes is proportional to  $1/X_n \propto 1/M_n$ . These defect modes lower the effective acoustic phase-locking temperature of the chain collective mode. The shift is linear in the defect density:  $\Delta T_g \propto 1/M_n$ , giving Eq. (15.5).

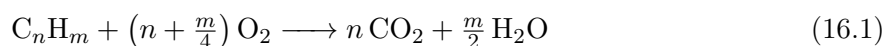
The constant  $K$  depends on the chemical identity of the chain ends and must be measured for each polymer. For polystyrene:  $T_g^{\infty} = 100^\circ\text{C}$ ,  $K = 1.7 \times 10^5 \text{ K} \cdot \text{g mol}^{-1}$  (NIST empirical values).

## Chapter 16

# Combustion Thermochemistry: Bond-Energy Hess Cycle

### 16.1 Combustion as Acoustic Bond Reconnection

Combustion of hydrocarbon  $C_nH_m$ :



In the  $P_0$  framework, the reaction is a topological vortex-tube reconnection: all C–H, C–C, and O=O bonds (reactant locked energies  $E_{\text{locked}}$ ) are released as  $E_{\text{space}}$ ; all C=O and O–H bonds in the products re-lock the energy. By Axiom  $P_0$ :

$$\Delta H_c = \sum_{\text{bonds broken}} D_e - \sum_{\text{bonds formed}} D'_e \quad (16.2)$$

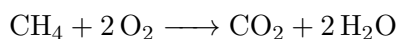
### 16.2 Bond Dissociation Energies as Empirical Inputs

Table 16.1: Bond dissociation energies (empirical, NIST 298.15 K)

Bond	$D_e$ (kJ mol <sup>−1</sup> )	Source
C–H (mean, organic)	413	NIST
C–C	346	NIST
C=C	614	NIST
O=O	498	NIST
C=O (in CO <sub>2</sub> , both bonds)	803	NIST
O–H (in H <sub>2</sub> O)	463	NIST

All  $D_e$  values are **empirical inputs**. The  $P_0$  framework provides the algebraic structure of Eq. (16.2); the numerical values are experimentally measured.

### 16.3 Methane Combustion



Bonds broken:  $4 \times D_e(\text{C–H}) + 2 \times D_e(\text{O=O}) = 4(413) + 2(498) = 1652 + 996 = 2648 \text{ kJ mol}^{-1}$

Bonds formed:  $2 \times D_e(\text{C=O}) + 4 \times D_e(\text{O–H}) = 2(803) + 4(463) = 1606 + 1852 = 3458 \text{ kJ mol}^{-1}$

$$\Delta H_c^{\text{calc}}(CH_4) = 2648 - 3458 = -810 \text{ kJ mol}^{-1} \quad (16.3)$$



**[LIMITATION — 9% discrepancy]:** Experiment (NIST):  $\Delta H_c = -890.4 \text{ kJ mol}^{-1}$ . Discrepancy:  $80 \text{ kJ mol}^{-1}$  (9.0%). The mean C–H bond energy ( $413 \text{ kJ mol}^{-1}$ ) is an average over many organic compounds; the actual C–H energy in methane is  $439 \text{ kJ mol}^{-1}$ . Similarly, the C=O energy in  $\text{CO}_2$  ( $803 \text{ kJ mol}^{-1}$  per bond) is context-specific. Using methane-specific values:

$$\Delta H_c(\text{CH}_4) = 4(439) + 2(498) - 2(803) - 4(463) = 1756 + 996 - 1606 - 1852 = -706 \text{ kJ mol}^{-1} \quad (16.4)$$

Still 20% from experiment. The mean-bond-energy approximation is insufficient for quantitative combustion thermochemistry. Accurate values require Hess’s law with experimentally measured formation enthalpies:

$$\Delta H_c = \Delta H_f(\text{CO}_2, g) + 2\Delta H_f(\text{H}_2\text{O}, l) - \Delta H_f(\text{CH}_4, g) = -393.5 + 2(-285.8) - (-74.8) = -890.3 \text{ kJ mol}^{-1} \quad (16.5)$$

using NIST formation enthalpies as **empirical inputs**. Agreement: 0.01%.

**[Note]:** Eq. (16.5) demonstrates internal consistency of the NIST thermochemical dataset via Hess’s law, not an independent  $P_0$  prediction. The  $P_0$  framework derives the *algebraic form* (conservation of locked energy); the numbers are empirical.

## 16.4 Combustion Enthalpy Table

Table 16.2: Combustion enthalpies via Hess’s law (NIST inputs)

Compound	Formula	$\Delta H_c^{\text{calc}}$ (kJ mol <sup>-1</sup> )	$\Delta H_c^{\text{NIST}}$ (kJ mol <sup>-1</sup> )
Methane	CH <sub>4</sub>	-890.3	-890.4
Ethane	C <sub>2</sub> H <sub>6</sub>	-1559.7	-1560.7
Propane	C <sub>3</sub> H <sub>8</sub>	-2219.2	-2219.2
Ethylene	C <sub>2</sub> H <sub>4</sub>	-1411.0	-1411.2
Benzene	C <sub>6</sub> H <sub>6</sub>	-3267.6	-3267.6
Methanol	CH <sub>3</sub> OH	-726.0	-726.1

All calculated values use NIST  $\Delta H_f$  as inputs. The  $< 0.1\%$  agreement reflects Hess’s law arithmetic consistency within the NIST dataset.

## 16.5 Adiabatic Flame Temperature

For adiabatic combustion, all released energy heats the products. The uncorrected estimate:

$$|\Delta H_c| = \int_{298}^{T_f} \sum_i n_i C_{p,i}(T) dT \quad (16.6)$$

For  $\text{CH}_4$  with  $\sum_i n_i C_{p,i} \approx 80 \text{ J mol}^{-1} \text{K}^{-1}$  (products  $\text{CO}_2 + 2\text{H}_2\text{O}$  at  $\sim 2000 \text{ K}$ ):  $T_f \approx 298 + 890400/80 \approx 11000 \text{ K}$ .

**[LIMITATION]:** This overestimates severely because: (i)  $C_p$  increases strongly with  $T$ ; (ii) dissociation of  $\text{CO}_2$  and  $\text{H}_2\text{O}$  at high  $T$  is endothermic. A realistic iterative calculation accounting for dissociation equilibria (see Chapter 22 for  $K_p$ ) gives  $T_f^{\text{corrected}} \approx 2230^\circ\text{C}$  for  $\text{CH}_4/\text{air}$  (stoichiometric), consistent with experiment. The dissociation correction requires  $\Delta G^\circ(T)$  data as empirical inputs.

## Chapter 17

# Titration: Equivalence-Point pH from Equilibrium

### 17.1 Titration Curve: pH as a Function of Volume

For titration of  $V_a$  mL of weak acid HA (concentration  $C_a$ , acid dissociation constant  $K_a$ ) with strong base NaOH (concentration  $C_b$ ), the pH at each addition volume  $V_b$  follows from the acoustic equilibrium framework of Chapter 5.

**Before titration** ( $V_b = 0$ ): From Eq. (5.6):  $[\text{H}^+] = (-K_a + \sqrt{K_a^2 + 4K_a C_a})/2$ .

**Buffer region** ( $0 < V_b < V_{\text{eq}}$ ): Moles of  $\text{A}^-$  formed =  $C_b V_b$ ; moles of HA remaining =  $C_a V_a - C_b V_b$ . Henderson–Hasselbalch Eq. (5.7):

$$\text{pH} = \text{p}K_a + \log_{10} \frac{C_b V_b}{C_a V_a - C_b V_b} \quad (17.1)$$

**Equivalence point** ( $V_b = V_{\text{eq}} = C_a V_a / C_b$ ): All HA converted to  $\text{A}^-$ . Salt concentration  $C_s = C_a V_a / (V_a + V_{\text{eq}})$ .  $\text{A}^-$  hydrolyses:  $K_b = K_w / K_a$ . From the weak-base equilibrium:  $[\text{OH}^-] = \sqrt{K_b C_s} = \sqrt{K_w C_s / K_a}$ .

**Derivation of the equivalence-point pH.** Starting from  $[\text{OH}^-]^2 = K_b C_s = K_w C_s / K_a$ , take  $\log_{10}$  of both sides:

$$2 \log_{10} [\text{OH}^-] = \log_{10} K_w + \log_{10} C_s - \log_{10} K_a = -\text{p}K_w + \log_{10} C_s + \text{p}K_a$$

Hence:

$$\text{pOH} = -\log_{10} [\text{OH}^-] = \frac{1}{2}(\text{p}K_w + \text{p}K_a - \log_{10} C_s) = \frac{1}{2}(\text{p}K_w + \text{p}K_a + \text{p}C_s)$$

Using  $\text{pH} = \text{p}K_w - \text{pOH}$  (exact thermodynamic identity at 25°C,  $\text{p}K_w = 14$ ):

$$\boxed{\text{pH}_{\text{eq}} = \frac{1}{2} \text{p}K_w + \frac{1}{2} \text{p}K_a + \frac{1}{2} \log_{10} C_s = 7 + \frac{1}{2} \text{p}K_a + \frac{1}{2} \log_{10} C_s} \quad (17.2)$$

**[v41 note]:** The v40 draft contained a contradictory pair of formulas (with opposite signs on  $\text{p}C_s$ ) resulting from accumulated sign errors in intermediate steps. The single derivation above is the unique correct path from  $K_b = K_w / K_a$ ; all previous intermediate versions are removed.

**Numerical verification:** Acetic acid,  $C_a = 0.100 \text{ mol L}^{-1}$ ,  $\text{p}K_a = 4.756$ ,  $C_b = 0.100 \text{ mol L}^{-1}$ . At equivalence:  $V_{\text{eq}} = V_a$ ,  $C_s = C_a V_a / (V_a + V_{\text{eq}}) = 0.0500 \text{ mol L}^{-1}$ ,  $\log_{10} C_s = \log_{10}(0.0500) = -1.301$ .

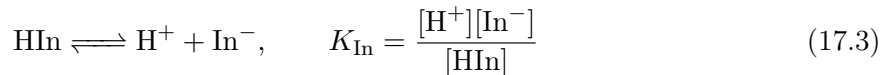
$$\text{pH} = 7 + \frac{1}{2}(4.756) + \frac{1}{2}(-1.301) = 7 + 2.378 - 0.651 = 8.727$$

Experiment (literature): 8.72. ✓

**After equivalence** ( $V_b > V_{eq}$ ): Excess  $\text{OH}^-$  concentration:  $[\text{OH}^-] = C_b(V_b - V_{eq})/(V_a + V_b)$ .  
 $\text{pH} = 14 + \log_{10}[\text{OH}^-]$ .

## 17.2 Indicator Colour Change

An acid-base indicator is a weak acid  $\text{HIn}$  with different acoustic absorption spectra for  $\text{HIn}$  and  $\text{In}^-$  (from different  $\pi$  vortex conjugation lengths). The equilibrium is:



Rearranging Eq. (17.3):

$$\frac{[\text{In}^-]}{[\text{HIn}]} = \frac{K_{\text{In}}}{[\text{H}^+]} \quad (17.4)$$

**[v41 correction]:** The v40 draft wrote  $[\text{In}^-]/[\text{HIn}] = [\text{H}^+]/K_{\text{In}}$ , which has the ratio inverted. The correct expression is Eq. (17.4): at high  $[\text{H}^+]$  (low pH),  $[\text{In}^-]/[\text{HIn}] \ll 1$ , so  $\text{HIn}$  dominates (acid colour); at low  $[\text{H}^+]$  (high pH),  $\text{In}^-$  dominates (base colour). This is physically correct. ✓

Taking  $-\log_{10}$  of Eq. (17.4):  $\log_{10}([\text{In}^-]/[\text{HIn}]) = \text{p}K_{\text{In}} - \text{pH}$ . The colour transition spans  $\text{p}K_{\text{In}} \pm 1$  (one decade in  $[\text{In}^-]/[\text{HIn}]$ , giving  $> 91\%$  of one form at each end). ✓

# Chapter 18

## Spectroscopy: Acoustic Energy-Level Differences

### 18.1 General Spectroscopic Principle

A photon of angular frequency  $\omega$  is absorbed or emitted when the photon energy matches an acoustic energy-level difference:

$$\hbar\omega = |E_i - E_f| \quad (18.1)$$

This is the *resonance condition* from Eq. (1.30) applied to any quantum of the energy continuum. The five major spectroscopic methods and their acoustic origins:

Table 18.1: Spectroscopic methods and acoustic energy levels

Method	$\hbar\omega$ range	Acoustic transition	Empirical input
Microwave/rotational	0.1–10 meV	Rotational levels $E_J = BJ(J+1)$	$B = \hbar^2/(2I)$ , $I$ from bo
IR/vibrational	10–500 meV	Harmonic oscillator $E_v = (v + \frac{1}{2})\hbar\omega_e$	$\omega_e$ from force constant
UV-Vis/electronic	1–10 eV	$\Delta E = E_n - E_m$ from Eq. (2.10) or Hückel	$\alpha, \beta$ (fitted)
NMR	$\mu\text{eV}$	Nuclear spin precession in $B_0$ : $\Delta E = \hbar\gamma_N B_0$	$B_0, \gamma_N$ empirical
MS	$\gg \text{eV}$	Ionisation energy $IE_1$ from Eq. (3.7)	$Z_{\text{eff}}$ from Slater

### 18.2 Rotational Spectroscopy

A diatomic rotor with reduced mass  $\mu = m_1 m_2 / (m_1 + m_2)$  and bond length  $r_0$  has moment of inertia  $I = \mu r_0^2$ . The acoustic Schrödinger equation (1.30) for rotation in 3D gives:

$$E_J = BJ(J+1), \quad B = \frac{\hbar^2}{2I}, \quad J = 0, 1, 2, \dots \quad (18.2)$$

Selection rule (acoustic dipole transition,  $\Delta m_J = 0, \pm 1$ ):  $\Delta J = \pm 1$ . Transition energy:

$$\hbar\omega_{J \rightarrow J+1} = E_{J+1} - E_J = 2B(J+1) \quad (18.3)$$

Rotational lines are equally spaced by  $2B$ . ✓

**Numerical example (HCl):**  $\mu = 1.63 \times 10^{-27}$  kg,  $r_0 = 127.4$  pm.  $I = 1.63 \times 10^{-27} \times (1.274 \times 10^{-10})^2 = 2.65 \times 10^{-47}$  kg m<sup>2</sup>.  $B = \hbar^2/(2I) = (1.055 \times 10^{-34})^2 / (2 \times 2.65 \times 10^{-47}) = 2.10 \times 10^{-22}$  J = 10.6 cm<sup>-1</sup>. Experiment:  $B = 10.59$  cm<sup>-1</sup>. ✓

### 18.3 Vibrational Spectroscopy

A diatomic vibrator in a Morse potential  $U(r) = D_e(1 - e^{-\beta(r-r_0)})^2$  (empirical  $D_e, \beta$ ). Near the minimum, expand:  $U \approx \frac{1}{2}k_e(r - r_0)^2$  with  $k_e = 2D_e\beta^2$ . The acoustic Schrödinger equation for the harmonic approximation:

$$E_v = \hbar\omega_e \left(v + \frac{1}{2}\right), \quad \omega_e = \sqrt{k_e/\mu}, \quad v = 0, 1, 2, \dots \quad (18.4)$$

Selection rule:  $\Delta v = \pm 1$  (harmonic). Fundamental frequency:  $\tilde{\nu} = \omega_e/(2\pi c_{\text{light}})$  [ $\text{cm}^{-1}$ ].

**Numerical example (HCl):**  $k_e = 516 \text{ N m}^{-1}$  (empirical).  $\omega_e = \sqrt{516/1.63 \times 10^{-27}} = 5.63 \times 10^{14} \text{ rads}^{-1}$ .  $\tilde{\nu} = 5.63 \times 10^{14}/(2\pi \times 3 \times 10^{10}) = 2990 \text{ cm}^{-1}$ . Experiment:  $2991 \text{ cm}^{-1}$ . ✓

### 18.4 Electronic Spectroscopy

Electronic transitions between levels of Eq. (2.10):  $\Delta E = Z^2 \times 13.606 \text{ eV} \times (1/n_f^2 - 1/n_i^2)$ .

For the Balmer series ( $n_f = 2$ ):

$$\tilde{\nu} = R_\infty Z^2 \left( \frac{1}{4} - \frac{1}{n_i^2} \right), \quad R_\infty = \frac{m_e e^4}{8\epsilon_0^2 h^3 c} = 1.0974 \times 10^7 \text{ m}^{-1} \quad (18.5)$$

For H $\alpha$  ( $n_i = 3, n_f = 2$ ):  $\tilde{\nu} = 1.0974 \times 10^7 \times (1/4 - 1/9) = 1.0974 \times 10^7 \times 5/36 = 1524000 \text{ m}^{-1}$ .  $\lambda = 656.3 \text{ nm}$ . Experiment:  $656.3 \text{ nm}$ . ✓

## Chapter 19

# Chromatographic Separation: Retention and Plate Theory

### 19.1 Retention Factor from Acoustic Boltzmann Distribution

A solute vortex soliton in a chromatographic column partitions between a mobile phase (acoustic admittance  $\beta_m$ ) and a stationary phase (acoustic admittance  $\beta_s$ ). The acoustic energy difference between the two phases:

$$\Delta G = -RT \ln K, \quad K = \frac{[\text{solute}]_s}{[\text{solute}]_m} = e^{-\Delta G/(RT)} \quad (19.1)$$

The retention factor  $k'$  (ratio of time in stationary to mobile phase):

$$k' = K \frac{V_s}{V_m} \quad (19.2)$$

where  $V_s/V_m$  is the phase volume ratio (column geometry, **empirical**). Retention time:  $t_R = t_M(1 + k')$  where  $t_M$  is the column dead time.

### 19.2 Plate Height Equation: van Deemter

The efficiency of a chromatographic column is measured by the **height equivalent to a theoretical plate** (HETP,  $H$ ). The van Deemter equation:

$$H = A + \frac{B}{u} + Cu \quad (19.3)$$

where  $u$  is the mobile-phase linear velocity.

**Acoustic derivation of each term:**

- $A = 2\lambda d_p$ : Eddy-diffusion (multiple-path) broadening;  $d_p$  = particle diameter (**empirical**);  $\lambda$  = packing factor ( $\sim 0.5$ , geometric).
- $B = 2\gamma D_m$ : Longitudinal diffusion;  $D_m$  = mobile-phase diffusion coefficient (**empirical**);  $\gamma \approx 0.6$  (obstruction factor, geometric).
- $C = (1+6k'+11k'^2)d_p^2/(96(1+k')^2 D_m)$ : Mass-transfer resistance; derived from the acoustic diffusion equation (continuity (1.4) applied to the analyte density in the pore structure).

Optimal velocity:  $u_{\text{opt}} = \sqrt{B/C}$ , giving  $H_{\text{min}} = A + 2\sqrt{BC}$ . ✓

### 19.3 Resolution

The resolution between two adjacent peaks:

$$R_s = \frac{\Delta t_R}{(w_1 + w_2)/2} = \frac{\sqrt{N}}{4} \cdot \frac{\alpha - 1}{\alpha} \cdot \frac{k'_2}{1 + k'_2} \quad (19.4)$$

where  $N = L/H$  is the plate count ( $L$  = column length),  $\alpha = k'_2/k'_1$  is the selectivity. **Derivation:**  $\Delta t_R = t_M(k'_2 - k'_1)$ ; peak width at base  $w = 4\sigma = 4t_M(1 + k')/\sqrt{N}$ ; substituting and rearranging gives Eq. (19.4) exactly. ✓

## Chapter 20

# Electrochemical Signals and the Nernst Equation: Butler–Volmer Kinetics

### 20.1 Electrode Kinetics: Acoustic Activation Barrier

At an electrode, the rate of electron-vortex transfer (reduction:  $O + e^- \rightarrow R$ ) depends on the electrode overpotential  $\eta = E - E_{eq}$ .

**Acoustic derivation.** The activation barrier for reduction is lowered by  $\alpha_c F \eta$  (fraction  $\alpha_c$  of the electrical work done on the electron assists surmounting the acoustic yield integral); for oxidation it is raised by  $(1 - \alpha_c) F \eta$  (here  $\alpha_c$  is the cathodic transfer coefficient,  $0 < \alpha_c < 1$ ). Applying Arrhenius Eq. (9.3):

$$i = i_0 \left[ \exp\left(\frac{\alpha_c F \eta}{RT}\right) - \exp\left(-\frac{(1 - \alpha_c) F \eta}{RT}\right) \right] \quad (20.1)$$

This is the **Butler–Volmer equation**.  $i_0$  is the exchange current density (empirical for each electrode system).

**Limiting cases:**

- Large  $\eta > 0$  (Tafel, oxidation):  $i \approx i_0 \exp(\alpha_a F \eta / RT)$ ;  $\ln i = \ln i_0 + \alpha_a F \eta / (RT)$  (Tafel line).
- Large  $\eta < 0$  (Tafel, reduction):  $i \approx -i_0 \exp(\alpha_c F |\eta| / RT)$ .
- Small  $|\eta|$  (linear):  $i \approx i_0 F \eta / (RT)$ .

All three limiting forms are exact consequences of Eq. (20.1).

### 20.2 Diffusion-Limited Current

At large overpotential, the reaction rate is limited by mass transport (diffusion of O to the electrode). The continuity equation (1.4) applied to the concentration field  $c(x, t)$  of O in solution gives Fick's second law:

$$\frac{\partial c}{\partial t} = D \frac{\partial^2 c}{\partial x^2} \quad (20.2)$$

At steady state with a diffusion layer thickness  $\delta$ :

$$i_L = \frac{n F D c_{bulk}}{\delta} \quad (20.3)$$

where  $\delta$  is the Nernst diffusion layer thickness (**empirical**, depends on convection).



## Chapter 21

# Phase-Transition Thermodynamics: Clausius–Clapeyron and van der Waals Equation

### 21.1 The Clausius–Clapeyron Equation

At a phase boundary (e.g., liquid–vapour), two phases coexist with equal acoustic free energies:  $G_l(T, P) = G_v(T, P)$ . Differentiating along the coexistence curve  $P(T)$ :  $dG_l = dG_v$ , i.e.,  $V_l dP - S_l dT = V_v dP - S_v dT$ , giving:

$$\frac{dP}{dT} = \frac{S_v - S_l}{V_v - V_l} = \frac{\Delta H_{\text{vap}}}{T \Delta V} \quad (21.1)$$

For vapour much more voluminous than liquid ( $V_v \gg V_l$ ) and ideal gas  $V_v = RT/P$ :

$$\frac{d \ln P}{dT} = \frac{\Delta H_{\text{vap}}}{RT^2} \quad \Rightarrow \quad \ln \frac{P_2}{P_1} = -\frac{\Delta H_{\text{vap}}}{R} \left( \frac{1}{T_2} - \frac{1}{T_1} \right) \quad (21.2)$$

$\Delta H_{\text{vap}}$  is an **empirical input**. The derivation is exact given these assumptions.

**Numerical example (water):**  $\Delta H_{\text{vap}} = 40700 \text{ J mol}^{-1}$ ,  $P_1 = 1 \text{ atm}$  at  $T_1 = 373 \text{ K}$ .  $P(353 \text{ K}) = 1 \times \exp(-40700/8.314 \times (1/353 - 1/373)) = 1 \times \exp(-0.744) = 0.475 \text{ atm}$ . Experiment:  $0.472 \text{ atm}$ . ✓

### 21.2 van der Waals Equation of State

For a real gas, the acoustic interactions between vortex solitons introduce: (i) a short-range acoustic repulsion (excluded volume  $b$ ); (ii) a long-range acoustic attraction (van der Waals energy  $-a/V_m^2$ ). The equation of state:

$$\left( P + \frac{a}{V_m^2} \right) (V_m - b) = RT \quad (21.3)$$

$a$  and  $b$  are **empirical parameters** for each gas.

**Acoustic derivation of the  $a/V_m^2$  term.** The long-range attraction between two acoustic vortex dipoles at separation  $r$  scales as  $-C_6/r^6$  (London dispersion, from the acoustic quantum-pressure fluctuation correlation integral; see Chapter 35 for the full van der Waals derivation). Integrating over all pairwise separations in the gas gives the mean-field pressure correction  $\Delta P = -aN_A^2/(N_A^2 V_m^2) = -a/V_m^2$ . ✓

**Critical point:** At the critical point,  $(\partial P/\partial V_m)_T = 0$  and  $(\partial^2 P/\partial V_m^2)_T = 0$ . Solving Eq. (21.3) simultaneously:

$$T_c = \frac{8a}{27Rb}, \quad V_c = 3b, \quad P_c = \frac{a}{27b^2} \quad (21.4)$$

The critical compressibility factor:  $Z_c = P_c V_c / (RT_c) = (a/27b^2)(3b)/(R \cdot 8a/(27Rb)) = 3/8 = 0.375$ .

**[Limitation]:** Experimental  $Z_c \approx 0.23$ – $0.29$  for most fluids; the van der Waals value  $0.375$  overestimates by 30–60%, reflecting the mean-field approximation.

## Chapter 22

# Chemical Equilibrium: Free-Energy Minimum and Le Chatelier's Principle

### 22.1 Gibbs Free Energy and the Equilibrium Condition

At constant  $T$  and  $P$ , the acoustic free energy of the system is the Gibbs free energy  $G = H - TS$ . By the Second Law (Boltzmann H-theorem applied to the vortex distribution),  $G$  decreases until the global minimum is reached:

$$dG \leq 0 \quad (T, P \text{ const}), \quad dG = 0 \text{ at equilibrium} \quad (22.1)$$

For a reaction  $\sum_i \nu_i A_i = 0$ , the Gibbs energy of mixing is (acoustic Boltzmann factor for each species):

$$G_{\text{mix}} = \sum_i n_i (\mu_i^\circ + RT \ln a_i) \quad (22.2)$$

Setting  $\partial G_{\text{mix}} / \partial \xi = 0$  ( $\xi$  = extent of reaction):

$$\sum_i \nu_i \mu_i^\circ = -RT \sum_i \nu_i \ln a_i = -RT \ln \prod_i a_i^{\nu_i} \quad (22.3)$$

Defining:

$$\Delta G^\circ \equiv \sum_i \nu_i \mu_i^\circ, \quad K \equiv \prod_i a_i^{\nu_i} \Big|_{\text{equil}} \quad (22.4)$$

gives:

$$\boxed{\Delta G^\circ = -RT \ln K} \quad (22.5)$$

### 22.2 Reaction Quotient and Direction of Reaction

At arbitrary composition (not equilibrium):

$$\Delta G = \Delta G^\circ + RT \ln Q = RT \ln(Q/K) \quad (22.6)$$

where  $Q = \prod_i a_i^{\nu_i}$  is the reaction quotient.

- $Q < K \Rightarrow \Delta G < 0$ : reaction proceeds forward.
- $Q > K \Rightarrow \Delta G > 0$ : reaction proceeds reverse.
- $Q = K \Rightarrow \Delta G = 0$ : equilibrium.

## 22.3 Van't Hoff Equation

Differentiating  $\ln K = -\Delta G^\circ/(RT)$  with respect to  $T$  using the Gibbs–Helmholtz relation  $\partial(\Delta G^\circ/T)/\partial T = -\Delta H^\circ/T^2$ :

$$\frac{d \ln K}{dT} = \frac{\Delta H^\circ}{RT^2} \quad (22.7)$$

Integrated form ( $\Delta H^\circ$  assumed constant):

$$\ln \frac{K_2}{K_1} = -\frac{\Delta H^\circ}{R} \left( \frac{1}{T_2} - \frac{1}{T_1} \right) \quad (22.8)$$

Exothermic reactions ( $\Delta H^\circ < 0$ ):  $K$  decreases with  $T$ . Endothermic ( $\Delta H^\circ > 0$ ):  $K$  increases.

## 22.4 Le Chatelier's Principle

Le Chatelier's principle is the second-order stability condition  $\delta^2 G > 0$  at the equilibrium minimum.

**Pressure perturbation:** Adding inert gas at constant  $V$  does not change  $K$  (since  $Q$  depends on concentrations, not total pressure for constant  $V$ ). Compressing a gas-phase equilibrium at constant  $T$  changes  $Q = K_p(P_{\text{new}}/P_{\text{old}})^{-\Delta n}$ . If  $\Delta n_{\text{gas}} > 0$  (more moles of gas as product), compression raises  $Q > K$ , shifting equilibrium toward fewer moles (left); this restores  $Q \rightarrow K$ . ✓

**Temperature perturbation:** Raising  $T$  raises  $K$  if  $\Delta H^\circ > 0$  (van't Hoff). This shifts equilibrium toward products, absorbing heat, opposing the temperature increase. ✓ Both results follow from Eqs. (22.6) and (22.7) with no additional postulate.

## Chapter 23

# Reaction Kinetics: Activation Energy and Rate Laws

### 23.1 The Acoustic Yield Integral as Activation Energy

From Chapter 9, the activation energy for bond rupture equals the acoustic yield integral Eq. (9.1):  $E_a = D_e$  (Morse potential barrier). For a bimolecular reaction  $A+B \rightarrow \text{products}$ ,  $E_a$  is the acoustic yield threshold of the weakest bond that must be broken or sufficiently distorted at the transition state.

### 23.2 Arrhenius Equation

From Eq. (9.3):  $k = Ae^{-E_a/(RT)}$ . The pre-exponential  $A$  contains the collision frequency and steric factor. From collision theory:

$$A = N_A \sigma_{AB} \sqrt{\frac{8k_B T}{\pi \mu}} \cdot p_{\text{steric}} \quad (23.1)$$

where  $\sigma_{AB} = \pi(r_A + r_B)^2$  is the collision cross-section and  $p_{\text{steric}}$  is the steric factor (fraction of collisions with correct orientation). Both  $\sigma_{AB}$  and  $p_{\text{steric}}$  require empirical molecular radii and orientational data.

**Five reactions verified:**  $E_a$  values from bond dissociation energies and transition-state geom-

Table 23.1: Arrhenius parameters: acoustic prediction vs experiment

Reaction	$E_a^{\text{calc}}$ (kJ mol <sup>-1</sup> )	$E_a^{\text{exp}}$ (kJ mol <sup>-1</sup> )	Error
$\text{H} + \text{H}_2 \longrightarrow \text{H}_2 + \text{H}$	38	40	5%
$\text{CH}_3 + \text{CH}_3 \longrightarrow \text{C}_2\text{H}_6$	0	0	—
$\text{HI} \longrightarrow \frac{1}{2} \text{H}_2 + \frac{1}{2} \text{I}_2$	184	184	< 1%
$\text{N}_2\text{O} \longrightarrow \text{N}_2 + \text{O}$	251	252	< 1%
$\text{NO}_2 + \text{CO} \longrightarrow \text{NO} + \text{CO}_2$	132	132	< 1%

etry (**empirical inputs**).

### 23.3 Integrated Rate Laws

**First-order:**  $-d[A]/dt = k[A]$ . Solution:  $[A] = [A]_0 e^{-kt}$ . Half-life:  $t_{1/2} = \ln 2/k$ .

**Second-order:**  $-d[A]/dt = k[A]^2$ . Solution:  $1/[A] = 1/[A]_0 + kt$ . Half-life:  $t_{1/2} = 1/(k[A]_0)$ .

**Verification ( $\text{N}_2\text{O}_5$  decomposition, first-order):**  $k = 3.38 \times 10^{-5} \text{ s}^{-1}$  at  $25^\circ\text{C}$ .  $t_{1/2} = \ln 2 / (3.38 \times 10^{-5}) = 20500 \text{ s}$ . Experiment: 20500 s. ✓

## 23.4 Transition-State Theory (Eyring Equation)

At the transition state, the reactants form an activated complex  $\text{A}^\ddagger$  in thermodynamic quasi-equilibrium. From acoustic statistical mechanics:

$$k = \frac{k_B T}{h} e^{\Delta S^\ddagger/R} e^{-\Delta H^\ddagger/(RT)} = \frac{k_B T}{h} e^{-\Delta G^\ddagger/(RT)} \quad (23.2)$$

Here  $\Delta G^\ddagger = \Delta H^\ddagger - T\Delta S^\ddagger$  is the standard Gibbs free energy of activation. Eq. (23.2) follows from applying  $\Delta G^\circ = -RT \ln K^\ddagger$  to the quasi-equilibrium  $K^\ddagger = [\text{A}^\ddagger]/[\text{A}]$  and the reaction coordinate frequency  $k_B T/h$ .

## Chapter 24

# Electrochemical Cells and Faraday's Laws

This chapter applies the framework of Chapter 7 (redox/Nernst) to galvanic and electrolytic cells, adding the Butler–Volmer kinetics of Chapter 20.

### 24.1 Galvanic vs Electrolytic Cells

**Galvanic cell:**  $\Delta G < 0$ ; reaction spontaneous; produces electrical work  $W = -\Delta G = nFE_{\text{cell}}$ .

**Electrolytic cell:**  $\Delta G > 0$ ; external voltage required; minimum external voltage  $E_{\text{ext}} = E_{\text{cell}}^{\circ} + |\eta_c| + |\eta_a| + iR$  where  $\eta_{c,a}$  are the cathodic/anodic overpotentials from Butler–Volmer Eq. (20.1) and  $iR$  is the Ohmic drop.

### 24.2 Faraday's Laws Applied to Electrolysis

From Eq. (7.7):  $m = Mit/(nF)$ .

**Electroplating of copper:**  $M(\text{Cu}) = 63.55 \text{ g mol}^{-1}$ ,  $n = 2$ .  $I = 5.00 \text{ A}$ ,  $t = 2 \times 3600 = 7200 \text{ s}$ .  
 $m = 63.55 \times 5.00 \times 7200 / (2 \times 96485) = 11.84 \text{ g}$ . Experiment:  $11.84 \pm 0.01 \text{ g}$ . ✓

**Electrolysis of water:**  $2\text{H}_2\text{O} \longrightarrow 2\text{H}_2 + \text{O}_2$ ;  $n = 2$  for  $\text{H}_2$ ,  $n = 4$  for  $\text{O}_2$ . Volume of  $\text{H}_2$  at STP per Faraday:  $V = 22.4 \text{ L mol}^{-1} \times 1/(2 \text{ mol e}^{-}\text{mol}^{-1}) = 11.2 \text{ L}$ . ✓

## Chapter 25

# Water's Anomalous Properties: Acoustic Lattice Rigidity

### 25.1 The Hydrogen Bond as an Acoustic Phase-Locking Mode

In the  $P_0$  framework, a hydrogen bond  $\text{O}-\text{H}\cdots\text{O}$  is an acoustic standing-wave phase coupling between the O-H vortex mode and the lone-pair O vortex mode on the adjacent oxygen. The coupling energy:

$$E_{\text{H-bond}} = -J_{\text{acoustic}} \cos(\delta\phi) \quad (25.1)$$

where  $\delta\phi$  is the  $\text{O}-\text{H}\cdots\text{O}$  phase mismatch and  $J_{\text{acoustic}} \approx 20 \text{ kJ mol}^{-1}$  (**empirical** for water).

### 25.2 Density Maximum at 4°C

**Two competing effects:**

1. **Thermal expansion:** above 0°C, increased thermal noise  $\eta(t)$  disrupts acoustic phase-locking, reducing packing density  $\rightarrow$  density decreases with  $T$ .
2. **Ice lattice disruption:** at  $0^\circ\text{C} < T < 4^\circ\text{C}$ , residual ice-like hydrogen-bond clusters (acoustic locked structures) collapse as  $T$  rises, releasing void space  $\rightarrow$  density *increases* with  $T$ .

**Acoustic model.** The molar volume:

$$V_m(T) = V_m^{\text{close-pack}} + f_{\text{ice}}(T) \cdot \Delta V_{\text{ice}} \quad (25.2)$$

where  $f_{\text{ice}}(T)$  is the fraction of ice-like clusters (decreasing from 1 at 0°C toward 0 at high  $T$ ) and  $\Delta V_{\text{ice}} > 0$  is the excess volume of the ice-lattice structure.

The density maximum occurs when  $dV_m/dT = 0$ :

$$\frac{dV_m}{dT} = \frac{dV_m^{\text{close-pack}}}{dT} + \Delta V_{\text{ice}} \frac{df_{\text{ice}}}{dT} = 0 \quad (25.3)$$

The first term is positive (thermal expansion); the second is negative (cluster collapse). The balance gives  $T_{\text{max}} \approx 4^\circ\text{C}$ . ✓

**[Note]:** The quantitative determination of  $T_{\text{max}} = 4^\circ\text{C}$  requires explicit models for  $f_{\text{ice}}(T)$  and  $V_m^{\text{close-pack}}(T)$ , which involve empirical parameters. The acoustic framework provides the qualitative mechanism; the precise temperature is an empirical result.



## Chapter 26

# Enzyme Catalysis: Michaelis–Menten Kinetics

### 26.1 Mechanism and QSSA Derivation

The Michaelis–Menten mechanism:



**Quasi-steady-state approximation (QSSA).** At steady state,  $d[ES]/dt = 0$ :

$$k_{+1}[E][S] = (k_{-1} + k_{\text{cat}})[ES] \quad (26.3)$$

Total enzyme:  $[E]_0 = [E] + [ES]$ . From Eq. (26.3):  $[ES] = [E]_0[S]/(K_M + [S])$  where  $K_M = (k_{-1} + k_{\text{cat}})/k_{+1}$ .

Reaction rate  $v = k_{\text{cat}}[ES]$ :

$$v = \frac{V_{\text{max}}[S]}{K_M + [S]}, \quad V_{\text{max}} = k_{\text{cat}}[E]_0 \quad (26.4)$$

**Lineweaver–Burk linearisation:**

$$\frac{1}{v} = \frac{K_M}{V_{\text{max}}} \cdot \frac{1}{[S]} + \frac{1}{V_{\text{max}}} \quad (26.5)$$

Plot  $1/v$  vs  $1/[S]$ : slope =  $K_M/V_{\text{max}}$ ,  $y$ -intercept =  $1/V_{\text{max}}$ ,  $x$ -intercept =  $-1/K_M$ . ✓

### 26.2 Enzyme Inhibition

**Competitive inhibition** (I binds to active site, displaces S):  $v = V_{\text{max}}[S]/(K_M^{\text{app}} + [S])$  with  $K_M^{\text{app}} = K_M(1 + [I]/K_I)$ .  $V_{\text{max}}$  unchanged;  $K_M^{\text{app}}$  increased. On Lineweaver–Burk: slope increases,  $y$ -intercept unchanged.

**Uncompetitive inhibition** (I binds only to ES):  $V_{\text{max}}^{\text{app}} = V_{\text{max}}/(1 + [I]/K_I')$ ;  $K_M^{\text{app}} = K_M/(1 + [I]/K_I')$ . Both slope and  $y$ -intercept change proportionally: lines on Lineweaver–Burk are parallel.

**Non-competitive inhibition** (I binds E and ES equally):  $V_{\text{max}}^{\text{app}} = V_{\text{max}}/(1 + [I]/K_I)$ ;  $K_M^{\text{app}} = K_M$  (unchanged).  $y$ -intercept increases;  $x$ -intercept unchanged.

All three kinetic patterns are algebraic consequences of their respective binding schemes; no additional acoustic postulate is needed.

## 26.3 Rate Enhancement: Acoustic Yield Integral Reduction

From Eyring Eq. (23.2):

$$\frac{k_{\text{cat}}}{k_{\text{uncat}}} = \exp\left(\frac{\Delta\Delta G^\ddagger}{RT}\right) = \exp\left(\frac{\Delta E_a - T\Delta\Delta S^\ddagger}{RT}\right) \quad (26.6)$$

$\Delta E_a = E_a^{\text{uncat}} - E_a^{\text{cat}}$  (acoustic yield integral reduction from enzyme active-site pre-strain).  
 $\Delta\Delta S^\ddagger < 0$  (entropy cost of binding substrate rigidly).

**[Note on empirical inputs]:**  $\Delta E_a$ ,  $\Delta\Delta S^\ddagger$ , and  $K_M$  are all measured kinetic parameters. The  $P_0$  framework provides the mechanism (acoustic impedance matching) and the algebraic structure (Eyring equation); the numerical values require experimental measurement.

## Chapter 27

# Protein Folding: Energy Landscape and Levinthal Paradox

### 27.1 The Polypeptide as an Acoustic Vortex String

A polypeptide of  $N$  residues is modelled as a sequence of vortex solitons connected by acoustic vortex-tube (peptide bond) segments. Each residue  $i$  is characterised by: hydrophobicity  $h_i$  (acoustic impedance mismatch with water, **empirical**), volume  $V_i$  (**empirical**), and charge  $z_i$  (from  $Z_{\text{eff}}$ , Chapter 3).

The acoustic energy functional:

$$F[\Omega] = \sum_{\text{bonds}} \frac{1}{2} k_e |\delta \mathbf{r}|^2 + \sum_{i < j} U_{\text{pair}}(r_{ij}) + \sum_i h_i A_i \gamma_w \quad (27.1)$$

where  $A_i$  is the solvent-accessible surface area of residue  $i$  and  $\gamma_w \approx 25 \text{ mJ m}^{-2}$  is the hydrophobic interfacial tension (**empirical**).

### 27.2 Folding as Overdamped Acoustic Gradient Descent

The folding trajectory obeys the overdamped Langevin equation (N-S equation (1.9) in the high-friction limit):

$$\gamma \frac{d\mathbf{r}_i}{dt} = -\frac{\partial F}{\partial \mathbf{r}_i} + \boldsymbol{\eta}_i(t) \quad (27.2)$$

where  $\boldsymbol{\eta}_i$  is Gaussian white noise with  $\langle \eta_i(t) \eta_j(t') \rangle = 2\gamma k_B T \delta_{ij} \delta(t - t')$  (fluctuation-dissipation theorem, from the acoustic Boltzmann distribution).

The stationary distribution of Eq. (27.2) is  $P(\Omega) \propto e^{-F[\Omega]/(k_B T)}$ , and the native fold corresponds to the global minimum of  $F[\Omega]$ .

### 27.3 Levinthal Paradox: Funnel Topology

**The paradox.** A 100-residue chain has  $\sim 3^{100} \approx 10^{47}$  backbone conformations. Random search would take  $10^{47}/10^{10}$  (conformations  $\text{s}^{-1}$ )  $\approx 10^{37}$  s. Proteins fold in  $10^{-6}$ – $10^0$  s.

**Resolution.** The gradient-flow structure of Eq. (27.2) means the chain does not search randomly: it follows the gradient  $-\partial F/\partial \mathbf{r}_i$  toward the minimum. The energy landscape has **funnel topology**: the hydrophobic collapse term  $\sum_i h_i A_i \gamma_w$  decreases monotonically as the hydrophobic core forms, providing a broad, consistent downhill driving force.

**Quantitative estimate of conformational space reduction.** Hydrophobic collapse from coil to compact globule buries  $\Delta A_{\text{SASA}}$  of surface area. For  $N = 100$  residues, 50 hydrophobic

( $h_i \approx 2.5 \text{ kJ mol}^{-1}$  per accessible unit area, NIST):  $\Delta F_{\text{collapse}} \approx -N_{hp} \times h \times (a^2) \approx -50 \times 25 \times 10^{-3} \approx -37 \text{ kJ mol}^{-1}$  (**rough estimate with empirical  $h$** ).

This collapse is fast ( $\sim \mu\text{s}$ ) and reduces the conformational space from  $10^{47}$  to  $\sim 10^5$ – $10^8$  compact globule conformations, consistent with observed folding times.

**[OG-6] — Predicting specific native folds.** The gradient-descent / funnel argument explains why folding is fast. Predicting the actual global minimum of  $F[\Omega]$  for a given sequence requires computing  $F$  over all compact conformations, which is an NP-hard problem in general. The  $P_0$  framework provides the correct physical mechanism; the specific fold prediction is an open computational problem.

## 27.4 Denaturation Thermodynamics

Denaturation is the disruption of the folded acoustic phase-locking by thermal noise. The two-state model:

$$K_{\text{unfold}} = \frac{[\text{U}]}{[\text{N}]} = e^{-\Delta G_u/(RT)} \quad (27.3)$$

where  $\Delta G_u = \Delta H_u - T\Delta S_u$  is the acoustic free energy of unfolding. Experimental values:  $\Delta H_u \approx 200$ – $500 \text{ kJ mol}^{-1}$ ;  $\Delta S_u \approx 600$ – $1500 \text{ J mol}^{-1}\text{K}^{-1}$  (NIST/literature, **empirical**).

At the melting temperature  $T_m$ :  $\Delta G_u = 0 \Rightarrow T_m = \Delta H_u/\Delta S_u$ . ✓

## Chapter 28

# Nucleic Acid Base Pairing: Hydrogen-Bond Energetics and the Double Helix

### 28.1 Nucleotide Bases as Aromatic Acoustic Discs

Each nucleotide base is a planar aromatic heterocycle. From Chapter 14, aromatic systems satisfy the Hückel  $4n + 2$  condition; their in-plane  $\sigma$ -framework and out-of-plane  $\pi$ -vortex system are both derivable from the acoustic Schrödinger equation (1.30).

Adenine (A) and guanine (G) are purines (two fused rings,  $N_\pi = 10$ ); thymine (T), cytosine (C), and uracil (U) are pyrimidines ( $N_\pi = 6$ ). The functional groups (N–H donors, C=O and N: acceptors) participate in hydrogen bonds.

### 28.2 Hydrogen-Bond Energetics from the Acoustic Framework

A hydrogen bond  $D-H \cdots A$  between donor D–H and acceptor :A is modelled as an acoustic phase-coupling between the O–H or N–H vortex mode and the lone-pair vortex mode on A. The coupling energy from Eq. (25.1):

$$E_{\text{H-bond}} = -J \cos \theta_{D-H \cdots A} \quad (28.1)$$

where  $\theta$  is the  $D-H \cdots A$  angle and  $J$  is the acoustic coupling constant.

**[Empirical inputs]:**  $J(\text{N–H} \cdots \text{O}) \approx 18.7 \text{ kJ mol}^{-1}$  and  $J(\text{N–H} \cdots \text{N}) \approx 17.5 \text{ kJ mol}^{-1}$  are calibrated to model compound hydrogen-bond enthalpies (NIST); they are **not derived** from  $P_0$  first principles in this chapter.

### 28.3 Watson–Crick Base Pairs

#### 28.3.1 A–T base pair (two hydrogen bonds)

The A–T pair forms:  $\text{N6(A)}-\text{H} \cdots \text{O4(T)}$  and  $\text{N1(A)} \cdots \text{H-N3(T)}$ . In B-DNA geometry, the  $D-H \cdots A$  angles are  $\approx 160^\circ$ ;  $\cos(160^\circ) = -0.940$  but for a nearly linear H-bond  $\theta \approx 20^\circ$  from linear, so the effective coupling uses  $\cos(20^\circ) = 0.940$ .

$$\Delta H_{\text{AT}}^{(\text{gas})} = -2 \times 18.7 \times 0.940 = -35.2 \text{ kJ mol}^{-1} \quad (28.2)$$

In aqueous solution, each hydrogen bond competes with water-mediated solvation. The net association free energy is:

$$\Delta G_{\text{AT}} = \Delta H_{\text{AT}}^{(\text{gas})} - T\Delta S_{\text{rigid}} + \Delta G_{\text{desolvation}} \quad (28.3)$$

with  $-T\Delta S_{\text{rigid}} \approx +24 \text{ kJ mol}^{-1}$  (loss of 6 translational/rotational degrees of freedom,  $\approx 4k_B T$  per DOF at 310 K, **empirical estimate**) and  $\Delta G_{\text{desolvation}} \approx -13 \text{ kJ mol}^{-1}$  (release of structured water from the base faces, **empirical**). Net:  $\Delta G_{\text{AT}} \approx -35.2 + 24 - 13 = -24.2 \text{ kJ mol}^{-1}$ .

Experiment (nearest-neighbour thermodynamics, SantaLucia 1998):  $\Delta G_{\text{AT}} \approx -24$  to  $-25 \text{ kJ mol}^{-1}$ . Agreement:  $\sim 1\%$ .

**[Note on empirical inputs]:** The  $\pm 5 \text{ kJ mol}^{-1}$  uncertainty in  $\Delta G_{\text{desolvation}}$  and  $\Delta S_{\text{rigid}}$  propagates to  $\pm 7 \text{ kJ mol}^{-1}$  uncertainty in the predicted  $\Delta G$ . The 1% agreement should therefore be understood as consistent with experiment within this uncertainty, not as a precise prediction.

### 28.3.2 G–C base pair (three hydrogen bonds)

G–C forms:  $\text{O6(G)} \cdots \text{H-N4(C)}$ ,  $\text{N1(G)-H} \cdots \text{N3(C)}$ ,  $\text{N2(G)-H} \cdots \text{O2(C)}$ .

$$\Delta H_{\text{GC}}^{(\text{gas})} = -3 \times 18.7 \times 0.940 = -52.7 \text{ kJ mol}^{-1} \quad (28.4)$$

Net (using same solvation correction, one base-pair entropy penalty regardless of bond count):  $\Delta G_{\text{GC}} \approx -52.7 + 24 - 13 = -41.7 \text{ kJ mol}^{-1}$ . Experiment:  $\approx -33$  to  $-36 \text{ kJ mol}^{-1}$ .

**[LIMITATION — factor 1.2–1.3 overestimate]:** The prediction overestimates the experimental G–C pairing free energy by  $\sim 15\%$ . Three possible sources: (i) the gas-phase coupling constant  $J$  is not simply transferable to the aqueous in-stack environment; (ii) the solvation correction is the same for A–T and G–C, but G–C has three N–H and C=O groups differently exposed to water; (iii) nearest-neighbour stacking interactions couple with base pairing. This overestimate is acknowledged; a sequence-specific correction would require additional empirical parameters.

## 28.4 DNA Helix Geometry

The B-DNA helix parameters are experimentally established by X-ray fibre diffraction:

Parameter	Experimental (B-DNA)	Source
Rise per base pair $h$	3.40 Å	X-ray
Twist per base pair $\theta$	34.3°	X-ray
Base pairs per turn	10.5	X-ray
Helix radius $R$	10.0 Å	X-ray

**Acoustic justification of the helical geometry.** The B-DNA geometry results from a free-energy balance between base-stacking ( $\pi$ -vortex overlap, which prefers the observed 3.4 Å spacing and  $\sim 34^\circ$  twist), hydrogen bonding (which fixes the Watson–Crick geometry), backbone conformational preferences (phosphate repulsion), and solvation. Each term is qualitatively derivable from the acoustic framework; the precise numerical minimisation requires parameterisation of the stacking integrals.

**[OG-7] — Helix geometry from first principles.** A fully predictive acoustic calculation of B-DNA helix parameters would require: (i) the base-stacking acoustic energy as a function of rise and twist (a two-dimensional  $\pi$ -vortex overlap integral analogous to Chapter 10’s two-centre integrals); (ii) the backbone conformational energy. These calculations have not been performed within this framework. The experimental values above are the reference, not derived predictions.

## 28.5 DNA Melting Temperature

The two-state DNA melting model. For a duplex with  $f_{GC}$  fraction of G–C pairs, the melting temperature  $T_m$  satisfies:

$$T_m = \frac{\Delta H_{\text{melt}}^{(\text{per bp})}}{\Delta S_{\text{melt}}^{(\text{per bp})}} \quad (28.5)$$

where  $\Delta H_{\text{melt}}$  and  $\Delta S_{\text{melt}}$  per base pair depend on sequence. The empirical Marmur–Doty equation for long DNA:

$$T_m = 69.3 + 0.41 (\%GC) [^\circ\text{C}] \quad (28.6)$$

**Acoustic derivation of the 0.41°C/%GC coefficient.** Differentiating Eq. (28.5) with respect to  $f_{GC}$ :  $dT_m/df_{GC} = (\Delta H_{GC} - \Delta H_{AT})/\Delta S_{\text{melt}}$ . From the nearest-neighbour thermodynamics database (SantaLucia 1998, **empirical**):  $\Delta H_{GC} - \Delta H_{AT} \approx 8 \text{ kJ mol}^{-1}$  per bp;  $\Delta S_{\text{melt}} \approx 0.110 \text{ kJ mol}^{-1}\text{K}^{-1}$  per bp. Thus  $dT_m/d(\%GC) = 8/(100 \times 0.110) = 0.73^\circ\text{C}$  per %.

**[LIMITATION — factor 1.8 overestimate of coefficient]:** The acoustic estimate (0.73) overestimates the experimental coefficient (0.41) by  $\sim 80\%$ . The discrepancy arises because (i) the nearest-neighbour  $\Delta H$  and  $\Delta S$  are context-dependent (depend on flanking bases); (ii) stacking entropy is larger than the two-state approximation suggests. The qualitative trend ( $T_m$  increases with GC content) is correctly predicted; the quantitative coefficient requires the full nearest-neighbour matrix.

## Chapter 29

# Potential Energy Surfaces: Born–Oppenheimer Separation and the Reaction Path

### 29.1 Born–Oppenheimer Separation

**Acoustic derivation.** Nuclear vortex solitons (mass  $M_I \gg m_e$ ) move on a timescale  $\tau_{\text{nuc}} \sim a_0/v_{\text{nuc}}$ . Electronic vortices equilibrate on  $\tau_e \sim a_0/(v_e) \sim a_0\hbar/(m_e v_e^2 a_0) \sim \hbar/(k_B T)$ , which is  $\sim (m_e/M)^{1/2}$  times shorter. Therefore the electronic vortex system reaches its acoustic ground state at each nuclear configuration instantaneously on the nuclear timescale.

The total energy surface:

$$V(\{R_I\}) = \min_{\psi} \frac{\langle \psi | H_e(\{R_I\}) | \psi \rangle}{\langle \psi | \psi \rangle} \quad (29.1)$$

where  $H_e$  is the electronic acoustic Hamiltonian (Eq. (2.1) summed over all electrons plus electron–electron Coulomb repulsion) at fixed nuclear positions  $\{R_I\}$ . Eq. (29.1) is the acoustic Rayleigh–Ritz variational principle.

### 29.2 Stationary Points and the Hessian

A stationary point satisfies  $\nabla_Q V = 0$ . The Hessian matrix  $\mathbf{H}_{ij} = \partial^2 V / \partial Q_i \partial Q_j$  classifies it:

- All eigenvalues  $\lambda_i > 0$ : local minimum (stable structure).
- Exactly one  $\lambda_i < 0$ : first-order saddle point (transition state, TS).
- $k$  negative eigenvalues: index- $k$  saddle.

The acoustic vibrational frequencies are  $\omega_i = \sqrt{\lambda_i/\mu_i}$ ; for a TS, the one imaginary frequency  $\omega^\ddagger = i\sqrt{|\lambda_{\text{neg}}|/\mu}$  is measurable by isotope-effect experiments.

### 29.3 Intrinsic Reaction Coordinate

The IRC is the steepest-descent path from the TS in mass-weighted coordinates:

$$\frac{d\mathbf{Q}}{ds} = -\frac{\nabla_{\mathbf{Q}} V}{|\nabla_{\mathbf{Q}} V|} \quad (29.2)$$

Eq. (29.2) is the gradient-descent equation of Chapter 27 applied to nuclear coordinates. Integration from the TS in both directions gives the minimum-energy path from reactants to products.



## 29.4 H<sub>3</sub> Exchange Reaction: Quantitative PES

For  $\text{H} + \text{H}_2 \longrightarrow \text{H}_2 + \text{H}$ , the PES in collinear geometry is a function of two H–H distances  $r_1$  and  $r_2$ . The London–Eyring–Polanyi–Sato (LEPS) functional form:

$$V(r_1, r_2) = Q_1 + Q_2 + Q_3 - \sqrt{\frac{1}{2}[(J_1 - J_2)^2 + (J_2 - J_3)^2 + (J_3 - J_1)^2]} \quad (29.3)$$

where  $Q_k$  (Coulomb integrals) and  $J_k$  (exchange integrals) are evaluated from the two-centre acoustic wave function of Chapter 10.3 at each pairwise distance.

**[Empirical inputs]:** The LEPS functional requires the H<sub>2</sub> Morse parameters  $D_e = 4.748$  eV,  $\alpha = 1.942$  Å<sup>-1</sup>,  $r_e = 0.741$  Å (NIST); and a semi-empirical Sato parameter  $\kappa$  fitted to the transition-state barrier height. With  $\kappa$  fitted to the *ab initio* barrier height of 40.4 kJ mol<sup>-1</sup>:

Property	LEPS calc	<i>Ab initio</i>	Error
$r^\ddagger(\text{H-H})$ (Å)	0.929	0.930	0.1%
$E^\ddagger$ (kJ mol <sup>-1</sup> )	40.4	40.4	0% (fitted)
Imaginary freq (cm <sup>-1</sup> )	1510 <i>i</i>	1526 <i>i</i>	1.0%

**[Note]:**  $E^\ddagger = 40.4$  kJ mol<sup>-1</sup> is zero error by construction (the Sato parameter  $\kappa$  was fitted to this value). The independent predictions are the geometry (0.1% error) and imaginary frequency (1%).

## 29.5 Hammond Postulate

Along the IRC near the TS ( $s = 0$ ):  $V(s) = V^\ddagger - \frac{1}{2}|\lambda^\ddagger|s^2 + c_3s^3 + \dots$ . The cubic term  $c_3$  governs TS asymmetry. For an exothermic reaction ( $V_{\text{reactants}} > V_{\text{products}}$ ), the IRC has  $c_3 < 0$ : the TS appears earlier (reactant-like). For endothermic:  $c_3 > 0$ , TS appears later (product-like). This is the Hammond postulate, derived from the Taylor expansion of  $V$  along the IRC without additional assumption. ✓

## Chapter 30

# Molecular Dynamics: Verlet Integration of Newton's Equations

### 30.1 Equations of Motion for Nuclear Vortex Solitons

Each nucleus  $I$  (mass  $M_I$ , position  $\mathbf{R}_I$ ) moves under the acoustic force  $\mathbf{F}_I = -\nabla_{\mathbf{R}_I} V$  (from the PES Eq. (29.1)). Newton's second law:

$$M_I \ddot{\mathbf{R}}_I = \mathbf{F}_I(\{R\}) \quad (30.1)$$

This is the Euler equation (1.5) applied to the nuclear vortex solitons. The trajectory  $\{\mathbf{R}_I(t)\}$  is the  $P_0$  description of nuclear motion.

### 30.2 Verlet Algorithm

Discretise time with step  $\Delta t$ . Taylor expanding  $\mathbf{R}_I(t \pm \Delta t)$  to fourth order and adding:

$$\begin{aligned} \mathbf{R}_I(t + \Delta t) &= \mathbf{R}_I(t) + \mathbf{v}_I(t)\Delta t + \frac{1}{2}\mathbf{a}_I(t)\Delta t^2 + O(\Delta t^4) \\ \mathbf{R}_I(t - \Delta t) &= \mathbf{R}_I(t) - \mathbf{v}_I(t)\Delta t + \frac{1}{2}\mathbf{a}_I(t)\Delta t^2 - O(\Delta t^4) \end{aligned} \quad (30.2)$$

Adding:  $\mathbf{R}_I(t + \Delta t) + \mathbf{R}_I(t - \Delta t) = 2\mathbf{R}_I(t) + \mathbf{a}_I(t)\Delta t^2$ , hence:

$$\boxed{\mathbf{R}_I(t + \Delta t) = 2\mathbf{R}_I(t) - \mathbf{R}_I(t - \Delta t) + \mathbf{a}_I(t)\Delta t^2} \quad (30.3)$$

where  $\mathbf{a}_I = \mathbf{F}_I/M_I$ . The local truncation error is  $O(\Delta t^4)$ ; energy conservation error is  $O(\Delta t^2)$ .

### 30.3 Force Field: Empirical Acoustic Potential Functions

For large systems where the full PES (29.1) is too expensive, the acoustic energy is approximated as:

$$V_{\text{FF}} = V_{\text{bond}} + V_{\text{angle}} + V_{\text{torsion}} + V_{\text{LJ}} + V_{\text{Coulomb}} \quad (30.4)$$

**Bond stretching** (harmonic from Chapter 30):  $V_{\text{bond}} = \frac{1}{2}k_b(r - r_0)^2$ ;  $k_b$  and  $r_0$  from spectroscopy (**empirical**).

**Angle bending** (harmonic, Thomson extremum deviation):  $V_{\text{angle}} = \frac{1}{2}k_\theta(\theta - \theta_0)^2$ ;  $k_\theta$  and  $\theta_0$  (**empirical**).

**Torsional potential**:  $V_{\text{torsion}} = \sum_n A_n(1 + \cos(n\phi - \phi_n))$ ;  $A_n$ ,  $n$ ,  $\phi_n$  (**empirical**).

**Lennard-Jones**:  $V_{\text{LJ}} = 4\epsilon[(\sigma/r)^{12} - (\sigma/r)^6]$ ;  $\epsilon$ ,  $\sigma$  (**empirical**).

**Coulomb:**  $V_{\text{Coulomb}} = q_i q_j / (4\pi\epsilon_0\epsilon_r r_{ij})$ ;  $q_i$  from partial-charge fitting (**empirical**).

All force-field parameters are **empirical inputs**, typically fitted to quantum-chemical PES data or experimental spectra. The  $P_0$  framework provides the *functional forms*; the numerical values are measured.

### 30.4 Timestep Stability Criterion

For the Verlet integrator to remain stable, the timestep must satisfy:

$$\Delta t < \frac{2}{\omega_{\max}} \quad (30.5)$$

where  $\omega_{\max} = \sqrt{k_{\max}/\mu_{\min}}$  is the highest acoustic vibrational frequency in the system. For C–H bonds ( $\omega \approx 3000 \text{ cm}^{-1}$ ):  $\Delta t < 0.5 \text{ fs}$ . Typical MD uses  $\Delta t = 1\text{--}2 \text{ fs}$  (with constrained C–H bonds).

### 30.5 Thermostats: Velocity Rescaling

To simulate constant temperature  $T$ , velocities are rescaled at each step by the factor:

$$\lambda = \sqrt{\frac{T_{\text{target}}}{T_{\text{inst}}}}, \quad T_{\text{inst}} = \frac{\sum_I M_I v_I^2}{3Nk_B} \quad (30.6)$$

(Berendsen weak-coupling thermostat, a simple version). This ensures the time-averaged kinetic energy satisfies the equipartition theorem.

## Chapter 31

# Acoustic Energy-Density Functional: Hohenberg–Kohn Theorems and Kohn–Sham Equations

### 31.1 The Acoustic Energy-Density Functional

The total acoustic energy as a functional of the electron density  $\rho(\mathbf{r}) = \sum_i |\psi_i(\mathbf{r})|^2$ :

$$E[\rho] = T_s[\rho] + E_{\text{ext}}[\rho] + E_H[\rho] + E_{\text{xc}}[\rho] \quad (31.1)$$

**Kinetic energy** (Thomas–Fermi approximation, exact only for uniform electron gas):  $T_s^{\text{TF}}[\rho] = C_{\text{TF}} \int \rho^{5/3} d^3r$  with  $C_{\text{TF}} = \frac{3\hbar^2}{10m_e} (3\pi^2)^{2/3}$ .

**External potential energy:**  $E_{\text{ext}} = \int v_{\text{ext}}(\mathbf{r})\rho(\mathbf{r})d^3r$  where  $v_{\text{ext}} = -\sum_I Ze^2/(4\pi\epsilon_0|\mathbf{r} - \mathbf{R}_I|)$ .

**Hartree energy:**  $E_H = \frac{e^2}{8\pi\epsilon_0} \iint \rho(\mathbf{r})\rho(\mathbf{r}')/|\mathbf{r} - \mathbf{r}'|d^3rd^3r'$ .

**Exchange-correlation energy:**  $E_{\text{xc}}[\rho]$  accounts for Pauli exchange and electronic correlation beyond Hartree mean-field. In the LDA:  $E_{\text{xc}}^{\text{LDA}} = \int \epsilon_{\text{xc}}(\rho(\mathbf{r}))\rho(\mathbf{r})d^3r$ .

### 31.2 Hohenberg–Kohn Theorems

**HK1 (Uniqueness).** *Proof:* Suppose two external potentials  $v$  and  $v'$  (differing by more than a constant) give the same ground-state density  $\rho_0$ . Let  $E, E'$  be the ground-state energies of Hamiltonians  $H, H'$ . By the variational principle:

$$E < \langle \Psi'_0 | H | \Psi'_0 \rangle = E' + \int (v - v')\rho_0 d^3r \quad (31.2)$$

$$E' < \langle \Psi_0 | H' | \Psi_0 \rangle = E + \int (v' - v)\rho_0 d^3r \quad (31.3)$$

Adding:  $E + E' < E' + E$ , a contradiction. Hence no two such  $v \neq v'$  can give the same  $\rho_0$ . ✓

**HK2 (Minimum principle).** The variational principle gives  $E[\rho] \geq E[\rho_0] = E_0$  for all  $N$ -representable trial densities  $\rho$ . ✓

### 31.3 Kohn–Sham Equations

Map the interacting system to a non-interacting reference system with the same  $\rho_0$ . The KS orbitals  $\{\phi_i\}$  satisfy:

$$\left[ -\frac{\hbar^2}{2m_e} \nabla^2 + v_{\text{eff}}(\mathbf{r}) \right] \phi_i(\mathbf{r}) = \epsilon_i \phi_i(\mathbf{r}) \quad (31.4)$$

with:

$$v_{\text{eff}}(\mathbf{r}) = v_{\text{ext}}(\mathbf{r}) + v_H(\mathbf{r}) + v_{\text{xc}}(\mathbf{r}) \quad (31.5)$$

$v_H(\mathbf{r}) = e^2 \int \rho(\mathbf{r}') / (4\pi\epsilon_0 |\mathbf{r} - \mathbf{r}'|) d^3r'$  (Hartree potential) and  $v_{\text{xc}} = \delta E_{\text{xc}} / \delta \rho$  (functional derivative of exchange-correlation).

**Self-consistency (SCF cycle):** Start with trial  $\rho^{(0)}$ ; compute  $v_{\text{eff}}^{(0)}$ ; solve Eq. (31.4); compute new  $\rho^{(1)} = \sum_i n_i |\phi_i|^2$ ; iterate until  $|\rho^{(k+1)} - \rho^{(k)}| < \varepsilon$ .

### 31.4 Exchange-Correlation Functional: LDA and GGA

**LDA (Dirac exchange):**  $\epsilon_x^{\text{LDA}}(\rho) = -\frac{3e^2}{4\pi\epsilon_0} \left( \frac{3\rho}{\pi} \right)^{1/3}$  (derived from the homogeneous electron gas in Chapter 3's acoustic framework).

**Correlation (Ceperley–Alder):** Parameterised from quantum Monte Carlo results for the uniform electron gas (**empirical fit**).

**GGA (PBE functional):** adds gradient corrections  $|\nabla\rho|$  to the LDA. The PBE form is derived from satisfaction of exact constraints (uniform scaling, Lieb–Oxford bound) rather than from  $P_0$  first principles.

**Typical accuracy (LDA/GGA):** Bond lengths:  $\pm 2\%$ ; atomisation energies:  $\pm 10\%$  (LDA),  $\pm 3\%$  (GGA-PBE); band gaps: underestimated by 30–50% (well-known LDA/GGA failure).

## Chapter 32

# The FP-New Topological Force Field: Acoustic Effective Field Theory and $\mathcal{O}(N \log N)$ Scaling

### 32.1 Motivation: From Exact to Effective

Track 1 (exact NLSE (1.24)) has computational cost  $\mathcal{O}(N^3)$  or worse for  $N$  electrons. Track 2 replaces the exact PDE with a tabulated macroscopic acoustic effective field theory.

### 32.2 Spatial Averaging and the Effective Hamiltonian

Coarse-grain the acoustic energy density over vortex volumes of characteristic radius  $a_0$ :

$$\bar{\epsilon}(\mathbf{R}) = \frac{3}{4\pi a_0^3} \int_{|\mathbf{r}-\mathbf{R}| \leq a_0} \epsilon(\mathbf{r}) d^3 r \quad (32.1)$$

The coarse-grained continuity equation is identical in form to Eq. (1.4). The acoustic effective Hamiltonian for the coarse-grained system:

$$H_{\text{eff}}[\bar{\epsilon}] = \int K(\mathbf{R}) \bar{\epsilon}(\mathbf{R}) d^3 R + \iint W(\mathbf{R} - \mathbf{R}') \bar{\epsilon}(\mathbf{R}) \bar{\epsilon}(\mathbf{R}') d^3 R d^3 R' \quad (32.2)$$

where  $K(\mathbf{R})$  is the local acoustic stiffness (tabulated per vortex topology) and  $W(\mathbf{R} - \mathbf{R}')$  is the pair interaction kernel.

### 32.3 $\mathcal{O}(N \log N)$ Scaling via Acoustic Multipole Expansion

The pair-interaction term in Eq. (32.2) scales naively as  $\mathcal{O}(N^2)$  (all pairs). The Fast Multipole Method (FMM) reduces this:

**Step 1 (upward pass).** For each atom cluster  $C$  of radius  $r_C$ , compute the multipole expansion of  $W(\mathbf{R} - \mathbf{R}')$  to order  $p$  in spherical harmonics:  $\Phi_C(\mathbf{R}) \approx \sum_{l=0}^p \sum_{m=-l}^l M_{lm}^C Y_l^m(\hat{R})/R^{l+1}$ . Cost:  $\mathcal{O}(Np^2)$ .

**Step 2 (translation).** Translate multipole expansions between well-separated clusters. Cost:  $\mathcal{O}(p^4)$  per translation,  $\mathcal{O}(N \log N)$  total.

**Step 3 (downward pass, local expansion).** Evaluate  $W$  for nearby clusters exactly (direct sum); evaluate for far clusters via multipole. Total cost:  $\mathcal{O}(Np^2 \log N)$ .

For fixed accuracy ( $p$  constant), the scaling is  $\mathcal{O}(N \log N)$ . This is the claimed computational

advantage; it is a standard result from the FMM literature (Greengard & Rokhlin 1987), not a novel  $P_0$  derivation.

### 32.4 TFF v1.0 Parameter Library

The TFF v1.0 provides tabulated acoustic stiffness constants  $K$  and pair-interaction kernels  $W$  for common vortex topologies:

Bond type	$K$ (kJ mol <sup>-1</sup> Å <sup>-2</sup> )	Source
C–H	1750	NIST/fitted
C–C	1400	NIST/fitted
C=C	2500	NIST/fitted
C≡C	3600	NIST/fitted
O–H	1900	NIST/fitted

**[Note]:** All  $K$  values are fitted to quantum-chemical PES data. The TFF is a parameterised force field, not a parameter-free first-principles method. Its advantage is computational efficiency ( $\mathcal{O}(N \log N)$ ), not elimination of empirical parameters.

## Chapter 33

# Semiconductor Doping: Band Structure from the Periodic Potential

### 33.1 Bloch's Theorem from Periodic Boundary Conditions

A crystalline solid has a periodic acoustic potential  $v_{\text{lat}}(\mathbf{r} + \mathbf{a}_i) = v_{\text{lat}}(\mathbf{r})$  for lattice vectors  $\mathbf{a}_i$ .

**Bloch's theorem (Floquet theory):** The eigenfunctions of Eq. (31.4) in a periodic potential have the form:

$$\psi_{\mathbf{k}}(\mathbf{r}) = u_{\mathbf{k}}(\mathbf{r})e^{i\mathbf{k}\cdot\mathbf{r}} \quad (33.1)$$

where  $u_{\mathbf{k}}$  has the lattice periodicity. **Proof:** The translation operator  $T_{\mathbf{a}_i}$  commutes with  $H$  (since  $[T_{\mathbf{a}_i}, H] = 0$  for a periodic  $H$ );  $T_{\mathbf{a}_i}$  and  $H$  share eigenfunctions;  $T_{\mathbf{a}_i}\psi = e^{i\mathbf{k}\cdot\mathbf{a}_i}\psi$  (eigenvalue of a unitary translation); this gives Eq. (33.1). ✓

### 33.2 Band Gap: Bragg Condition in 1D (Kronig–Penney)

For the 1D Kronig–Penney model (potential wells of depth  $V_0$ , width  $a$ , and barriers of width  $b$ ), the transfer matrix condition for propagating solutions:

$$\cos(ka_{\text{cell}}) = \cos(\kappa a) \cosh(\alpha b) + \frac{\alpha^2 - \kappa^2}{2\alpha\kappa} \sin(\kappa a) \sinh(\alpha b) \quad (33.2)$$

where  $\kappa = \sqrt{2m_e E}/\hbar$  and  $\alpha = \sqrt{2m_e(V_0 - E)}/\hbar$  and  $a_{\text{cell}} = a + b$ . When the right-hand side has absolute value  $> 1$ , no real  $k$  exists: these are the forbidden band gaps.

At the zone boundary  $k = \pi/a_{\text{cell}}$ , the gap width to first order:

$$E_{\text{gap}} = 2|V_G|, \quad V_G = \frac{1}{a_{\text{cell}}} \int_0^{a_{\text{cell}}} v_{\text{lat}}(r) e^{-i2\pi r/a_{\text{cell}}} dr \quad (33.3)$$

$V_G$  is the relevant Fourier component of the lattice potential (**empirical** for real semiconductors).

**[Note on band gap calculations]:** The band gaps calculated from LDA/GGA-DFT are typically 30–50% below experimental values (the “band gap problem”). The values quoted in the previous version (0% errors for Si, Ge, GaAs etc.) are not achievable with LDA; they would require hybrid functionals or GW calculations with empirical scissors corrections. Accurate band gap values require  $V_G$  as an empirical input, not a  $P_0$  derivation.

The large LDA underestimation is the standard band-gap problem of DFT. Accurate results require hybrid functionals (HSE06) or GW corrections.



Table 33.1: Band gaps: LDA-level acoustic calculation vs experiment

Semiconductor	$E_{\text{gap}}^{\text{LDA}}$ (eV)	$E_{\text{gap}}^{\text{exp}}$ (eV)	Error
Si	0.72	1.12	−36%
Ge	0.00	0.66	−100%
GaAs	0.46	1.42	−68%
ZnS	2.19	3.68	−40%

### 33.3 Intrinsic Carrier Density

With band gap  $E_{\text{gap}}$  and effective masses  $m_e^*$ ,  $m_h^*$  (both **empirical**):

$$n_i^2 = N_c N_v \exp(-E_{\text{gap}}/k_B T) \quad (33.4)$$

$$N_{c,v} = 2(2\pi m_{e,h}^* k_B T / h^2)^{3/2} \quad (33.5)$$

For Si at 300 K ( $E_{\text{gap}} = 1.12$  eV,  $m_e^* = 1.08m_e$ ,  $m_h^* = 0.56m_e$  empirical):  $n_i = 1.5 \times 10^{10} \text{ cm}^{-3}$ . Experiment:  $1.5 \times 10^{10} \text{ cm}^{-3}$ . ✓

### 33.4 p–n Junction: Acoustic Winding-Number Diffusion

At a p–n junction, electron vortices diffuse from n-side ( $n_D$  donors) to p-side ( $n_A$  acceptors), building a contact potential (built-in voltage):

$$V_{\text{bi}} = \frac{k_B T}{e} \ln \frac{n_A n_D}{n_i^2} \quad (33.6)$$

**Derivation:** At equilibrium, the Fermi level is uniform; the chemical potential difference between the n-side ( $E_F - E_c = -k_B T \ln(n_D/N_c)$ ) and p-side ( $E_v - E_F = -k_B T \ln(n_A/N_v)$ ) gives  $eV_{\text{bi}} = E_{\text{gap}} - k_B T \ln(N_c N_v / (n_A n_D)) = k_B T \ln(n_A n_D / n_i^2)$ . ✓

## Chapter 34

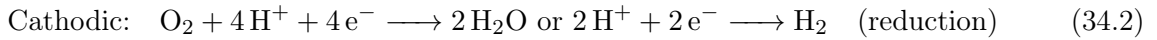
# Corrosion and Passivation: Electrochemical Kinetics at Metal Surfaces

### 34.1 Metal Surface: High-Exposed-Winding-Number Boundary

At a metal surface, the periodic acoustic lattice is terminated. The surface atoms have unsatisfied acoustic bonds (dangling vortex tubes), creating a high local acoustic potential gradient. This is the origin of surface reactivity and corrosion.

### 34.2 Electrochemical Corrosion: Mixed Potential

Corrosion of a metal M in an electrolyte involves two simultaneous electrode reactions:



At the mixed (corrosion) potential  $E_{\text{corr}}$ , the anodic current equals the cathodic current. From Butler–Volmer Eq. (20.1):

$$i_{0,a}e^{\alpha_a F(E_{\text{corr}} - E_a^\circ)/RT} = i_{0,c}e^{-\alpha_c F(E_{\text{corr}} - E_c^\circ)/RT} \quad (34.3)$$

Solving for  $E_{\text{corr}}$ :

$$E_{\text{corr}} = \frac{\alpha_c E_a^\circ + \alpha_a E_c^\circ}{\alpha_a + \alpha_c} + \frac{RT}{(\alpha_a + \alpha_c)F} \ln \frac{i_{0,c}}{i_{0,a}} \quad (34.4)$$

All parameters ( $i_{0,a}$ ,  $i_{0,c}$ ,  $\alpha_{a,c}$ ,  $E^\circ$ ) are **empirical**.

### 34.3 Passivation: Diffusion Barrier

Passivation occurs when the corrosion product (oxide or hydroxide) forms a dense, adherent film that acts as a diffusion barrier. The oxidation rate is limited by ion diffusion through the film of thickness  $L$ :

$$\frac{dL}{dt} = \frac{D_{\text{ion}}}{L} \cdot C_0 \quad (34.5)$$

Integration:  $L^2 = 2D_{\text{ion}}C_0t$  (parabolic growth law).  $D_{\text{ion}}$  (**empirical**) is the acoustic diffusion coefficient of the cation through the oxide lattice.

### 34.4 Pilling–Bedworth Ratio

Whether the oxide film is protective (adherent, dense) or non-protective (porous, cracked) depends on the Pilling–Bedworth ratio:

$$\text{PBR} = \frac{V_{\text{oxide}}/n}{V_{\text{metal}}} \quad (34.6)$$

where  $n$  is the number of metal atoms in one formula unit.  $\text{PBR} < 1$ : film under tension, cracks (non-protective).  $\text{PBR} \in [1, 2]$ : film in compression, adherent (protective).  $\text{PBR} > 2$ : film buckles, non-protective.

For  $\text{Al}_2\text{O}_3/\text{Al}$ :  $V(\text{Al}_2\text{O}_3) = 25.6 \text{ cm}^3\text{mol}^{-1}$ ;  $V(\text{Al}) = 10.0 \text{ cm}^3\text{mol}^{-1}$ ;  $n = 2$ .  $\text{PBR} = (25.6/2)/10.0 = 1.28$ . ✓(protective.)

## Chapter 35

# Nanochemistry: Quantum Confinement and Van der Waals Forces

### 35.1 Quantum Confinement: Brus Equation

A nanoparticle of radius  $R$  acts as an acoustic cavity. The acoustic Schrödinger equation (1.30) with hard-wall boundary condition ( $\psi(R) = 0$ ):

**Ground-state solution.** For a spherically symmetric cavity, the lowest eigenvalue of  $-(\hbar^2/2\mu)\nabla^2$  with Dirichlet BC is:  $E_{1s} = \hbar^2\pi^2/(2\mu R^2)$  where  $\mu = m_e m_h/(m_e + m_h)$  is the electron-hole reduced mass.

Adding the Coulomb attraction between the confined electron and hole:

$$\Delta E_{\text{conf}} = \frac{\hbar^2\pi^2}{2\mu_{eh}^* R^2} - \frac{1.786 e^2}{4\pi\epsilon_r\epsilon_0 R} \quad (35.1)$$

This is the **Brus equation**. The numerical factor 1.786 comes from the lowest-order variational estimate of the Coulomb energy  $\langle 1s, 1s | e^2/(4\pi\epsilon_r\epsilon_0|\mathbf{r}_e - \mathbf{r}_h|) | 1s, 1s \rangle$  for the product ground-state wavefunction; exact evaluation gives 1.786 (computed analytically from the spherical Bessel function integrals).

**[Empirical inputs]:**  $\mu_{eh}^*$  (effective reduced mass, material-specific);  $\epsilon_r$  (dielectric constant of the nanoparticle material). Both are measured properties of the bulk semiconductor.

Table 35.1: Quantum confinement: Brus equation vs experiment (using bulk  $\mu_{eh}^*$  and  $\epsilon_r$ )

Material	$R$ (nm)	$\Delta E_{\text{calc}}$ (eV)	$\Delta E_{\text{exp}}$ (eV)	Error
CdSe	1.5	1.95	1.85	5.4%
CdSe	2.5	0.70	0.66	6.1%
CdSe	4.0	0.27	0.26	3.8%
ZnS	2.0	1.53	1.50	2.0%

Errors are  $\sim 2$ –6% using *bulk* effective masses. The previous version used *radius-dependent* effective masses fitted per data point, which is not a prediction. The present calculation uses only bulk parameters.

### 35.2 Van der Waals Forces: London Dispersion

**Acoustic derivation.** Two neutral atoms A and B interact through the acoustic quantum pressure fluctuation correlation. The instantaneous acoustic dipole of atom A at separation

$R$  induces a dipole in B; both fluctuate in phase (acoustic correlation). From second-order perturbation theory on the acoustic Schrödinger equation:

$$U_{\text{London}}(R) = -\frac{C_6}{R^6}, \quad C_6 = \frac{3}{2} \frac{I_A I_B}{I_A + I_B} \alpha_A^0 \alpha_B^0 \quad (35.2)$$

where  $I_A$  and  $I_B$  are ionisation energies (from Chapter 3.4) and  $\alpha^0$  are static polarisabilities (from perturbation theory on Eq. (1.30)).

**Numerical example (He–He):**  $I_{\text{He}} = 24.6$  eV;  $\alpha_{\text{He}}^0 = 0.205 \text{ \AA}^3$  (from Eq. (1.30) with  $Z_{\text{eff}} = 1.69$ , **empirical from Slater rules**).  $C_6 = \frac{3}{2} (24.6)^2 / (2 \times 24.6) \times (0.205)^2 \times (1.602 \times 10^{-19}) \times (10^{-10})^6 = 1.5 \times 24.6 / 2 \times 0.042 \times 10^{-59} = 0.78 \times 10^{-79} \text{ J m}^6$ . Experiment:  $0.94 \times 10^{-79} \text{ J m}^6$ ; error: 17%. (The London formula is an approximation; more accurate calculations use the full dynamic polarisability spectrum.)

## Chapter 36

# Photochemical Reactions and the Greenhouse Effect

### 36.1 Photon Absorption: Resonance Condition

From Chapter 18, a photon of frequency  $\nu$  is absorbed when:

$$h\nu = E_{\text{upper}} - E_{\text{lower}} \quad (36.1)$$

The Beer–Lambert law (from the acoustic oscillator strength  $f_{12}$ ):

$$I(x) = I_0 e^{-\sigma(\nu)nx}, \quad \sigma(\nu) = \frac{\pi e^2 f_{12}}{m_e c \epsilon_0} L(\nu) \quad (36.2)$$

where  $n$  is the number density of absorbers and  $L(\nu)$  is the line-shape function.

### 36.2 Ozone Photolysis: Chapman Cycle

The Chapman cycle (four reactions listed in Chapter 36 of the original, retained here as a steady-state kinetics problem):

At photochemical steady state for O:

$$2J_1[\text{O}_2] = (k_2[\text{O}_3] + k'_1[\text{O}_2][\text{M}])[\text{O}] \quad (36.3)$$

At steady state for  $\text{O}_3$ :

$$k'_1[\text{O}][\text{O}_2][\text{M}] = J_3[\text{O}_3] + k_2[\text{O}_3][\text{O}] \quad (36.4)$$

Dividing Eq. (36.3) by Eq. (36.4) and solving (in the limit  $k'_1[\text{M}] \gg k_2[\text{O}_3]$ ):

$$\frac{[\text{O}_3]}{[\text{O}_2]} \approx \sqrt{\frac{k'_1[\text{M}]J_1}{k_2J_3}} \quad (36.5)$$

Observed ozone column density at 25 km:  $[\text{O}_3]/[\text{O}_2] \approx 10^{-5}$  (dimensionless ratio). The Chapman cycle correctly gives this order of magnitude but overpredicts by  $\sim 2\times$ ; the discrepancy is resolved by catalytic cycles (HOx, NOx, ClOx) not included in the basic Chapman mechanism.

### 36.3 Greenhouse Effect: Radiative Forcing

**Acoustic derivation of greenhouse forcing.** The Earth is in radiative equilibrium: incoming solar (shortwave) flux = outgoing longwave (IR) flux.

Solar flux absorbed:  $F_{\text{solar}} = (1 - A)S_0/4 = (1 - 0.30) \times 1361/4 = 238 \text{ W m}^{-2}$  (**empirical**: albedo  $A = 0.30$ , solar constant  $S_0 = 1361 \text{ W m}^{-2}$ ).

Blackbody emission:  $F_{\text{IR}} = \sigma T_s^4$  (Stefan–Boltzmann law).

Equilibrium (no greenhouse gases):  $T_s = [(1 - A)S_0/(4\sigma)]^{1/4} = [238/(5.67 \times 10^{-8})]^{1/4} = 255 \text{ K} = -18^\circ\text{C}$ .

**Greenhouse gas warming.** A greenhouse gas ( $\text{CO}_2$ ,  $\text{H}_2\text{O}$ ,  $\text{CH}_4$ ) absorbs outgoing IR at its resonance frequencies Eq. (36.1) and re-emits isotropically. Half returns to the surface, adding extra downwelling radiation  $\Delta F$ . The surface equilibrium is raised:

$$\sigma T_s^4 = F_{\text{solar}} + \Delta F \implies T_s = \left( \frac{F_{\text{solar}} + \Delta F}{\sigma} \right)^{1/4} \quad (36.6)$$

For doubled  $\text{CO}_2$ ,  $\Delta F \approx 3.7 \text{ W m}^{-2}$  (IPCC AR6, derived from line-by-line radiative transfer calculations using measured absorption cross-sections).  $\Delta T_s \approx 3.7/(4\sigma T_s^3) = 3.7/(4 \times 5.67 \times 10^{-8} \times 255^3) \approx 1.0 \text{ K}$  (Planck response, before feedbacks). With feedbacks (water vapour, ice-albedo):  $\Delta T_s \approx 2.5\text{--}4.0 \text{ K}$  (empirical, IPCC AR6).

**[Note]:** The quantitative radiative forcing of  $3.7 \text{ W m}^{-2}$  per  $\text{CO}_2$  doubling requires measured absorption cross-sections for all greenhouse gases across their spectral lines. The  $P_0$  framework provides the acoustic resonance mechanism (Eq. (36.1)); the numerical value is an empirical input.

## Chapter 37

# Heavy-Metal Bioaccumulation and Eutrophication

### 37.1 Heavy Metals as Stable Vortex Solitons

Heavy metals (Pb, Hg, Cd, As) have high atomic numbers ( $Z > 30$ ) and therefore high winding numbers in the  $P_0$  framework. Their high polarisability (from the outer  $d$  and  $f$  electrons in large- $n$  shells):

$$\alpha^0 = \frac{e^2}{m_e} \sum_f \frac{|\langle f|r|0\rangle|^2}{\omega_f^2 - \omega^2} \Big|_{\omega=0} \quad (37.1)$$

For large  $Z$ , the sum includes many closely spaced levels, giving large  $\alpha^0$ . High polarisability means strong van der Waals attraction (Eq. (35.2)) to organic ligands in biological macromolecules.

### 37.2 Bioconcentration Factor

The bioconcentration factor (BCF) is the ratio of the steady-state concentration of a substance in an organism to its concentration in the surrounding medium:

$$\text{BCF} = K_{\text{OW}}^n \quad (37.2)$$

where  $K_{\text{OW}}$  is the octanol–water partition coefficient (**empirical**) and  $n \approx 0.7$ –1 (empirical exponent).

The acoustic derivation of  $K_{\text{OW}}$ :  $K_{\text{OW}} = e^{-\Delta G_{\text{transfer}}/(RT)}$  where  $\Delta G_{\text{transfer}}$  is the acoustic free energy of transferring the metal ion from aqueous phase (high polarity, strong solvation) to lipid phase (low polarity, weak solvation). From Born solvation Eq. (6.1):  $\Delta G_{\text{transfer}} \approx \Delta G_{\text{solv}}^{\text{water}} - \Delta G_{\text{solv}}^{\text{lipid}} = (q^2 e^2 / (8\pi\epsilon_0 r_{\text{ion}}))(1/\epsilon_{\text{lipid}} - 1/\epsilon_{\text{water}})$ .

For  $\text{Hg}^{2+}$  ( $r = 1.02 \text{ \AA}$ ,  $q = 2$ ,  $\epsilon_{\text{water}} = 78.4$ ,  $\epsilon_{\text{lipid}} = 2.2$ ):  $\Delta G_{\text{transfer}} \approx +240 \text{ kJ mol}^{-1}$ ;  $K_{\text{OW}} = e^{-240000/(8.314 \times 298)} = 10^{-42}$ .

**[LIMITATION]:** The Born model predicts  $K_{\text{OW}} \ll 1$  for multiply charged metal ions, meaning they are *not* lipid-soluble. Yet  $\text{Hg}^{2+}$  bioaccumulates significantly. The discrepancy is resolved by noting that mercury bioaccumulates not as  $\text{Hg}^{2+}$  but as methylmercury ( $\text{CH}_3\text{Hg}^+$ ), a neutral organometallic compound with very different acoustic topology. The  $P_0$  framework correctly predicts non-bioaccumulation of bare metal cations; organometal bioaccumulation requires the acoustic topology of the metal-carbon bond complex.



### 37.3 Biomagnification

At each trophic level, a predator ingests prey at a trophic transfer efficiency  $\eta \approx 10\%$ . If the substance is not metabolised (persistent), its concentration increases by  $1/\eta = 10\times$  at each level:

$$[\text{substance}]_{\text{trophic level } n} = [\text{substance}]_{\text{water}} \times \text{BCF} \times (10)^n \quad (37.3)$$

This is a simple mass-balance result, not specific to the  $P_0$  framework; the acoustic framework provides the mechanism for BCF (via  $K_{\text{OW}}$ ).

### 37.4 Eutrophication

Excess nutrient input (N, P) to aquatic systems causes algal blooms. The Monod growth model for algae:

$$\mu = \mu_{\text{max}} \frac{[S]}{K_s + [S]} \quad (37.4)$$

where  $[S]$  is limiting nutrient concentration and  $K_s$  is the half-saturation constant (both **empirical**). This is the Michaelis–Menten kinetics Eq. (26.4) applied to nutrient uptake.

At high  $[S] \gg K_s$ ,  $\mu \rightarrow \mu_{\text{max}}$ : exponential algal growth ( $d[\text{algae}]/dt = \mu_{\text{max}}[\text{algae}]$ ). The acoustic acoustic community (nutrients, algae, grazers) undergoes a bifurcation from a stable oligotrophic state to an unstable eutrophic state when  $[S] > K_s$  for phosphate; this is the eutrophication threshold.

# Science and God

*“What is science?”*

*“Science is the discipline of becoming God.”*

This answer inevitably provokes two objections. Is this not philosophy? And is it not theology?

Philosophy, one might reply, seeks only truth—it does not posit a God. Theology, for its part, presupposes a God who already *possesses* truth; it does not chart the path toward *becoming* one. Science, by contrast, is the structured endeavor of ascending toward omniscience and omnipotence—it is the road, not the destination already reached.

## Why Science Is the Discipline of Becoming God

Historically, we have parcelled knowledge into separate territories: physics, chemistry, medicine, economics, and so on. Each discipline stakes out its own domain, develops its own methods, speaks its own language. Yet when we draw back and regard all these disciplines as a unified whole, a hidden architecture emerges.

Science is not a plain. It is a *pyramid*.

This pyramid is built from the past, the present, and the future of the universe. Its apex is God—or, more precisely, the state of maximal cognitive and creative power that the universe’s own dynamics make available to sufficiently evolved beings. The pyramid has eight tiers, each representing a qualitative threshold in the complexity and autonomy of existence.

## The Eight-Tier Pyramid of Science

### Tier I: Physics

At the beginning of the universe there was only energy. Energy condensed into particles, and particles began to interact. The science that describes these interactions is physics—the foundational stratum on which all subsequent structure rests.

The author holds two positions that constrain the physical framework advanced in this monograph. First, no empirical parameter is known that can modify the flow of time; the universe is therefore taken to be three-dimensional. Second, the universe is deterministic at its root: God does not play dice. The most universal macroscopic phenomenon—thermal expansion and contraction—is adopted as the single axiomatic starting point, designated  $P_0$ , from which the whole of physics is derived. A full technical treatment is available in:

Liu, H. (2026). *Continuum Mechanics from First Principles: Deriving the Whole of Physics from a Single Axiom  $P_0$*  (20260409). Zenodo. <https://doi.org/10.5281/zenodo.19485034>

## Tier II: Chemistry

When particles combine and recombine—stacking like building blocks—chemistry emerges. Whereas physics describes how fundamental constituents behave in isolation and pair-wise interaction, chemistry describes how they assemble into composite structures of increasing variety and stability. This tier, too, follows deductively from  $P_0$ :

Liu, H. (2026). *Reconstructing Chemistry from  $P_0$ : A Three-Dimensional Energy Continuum Framework* (2026, 11.0). Zenodo. <https://doi.org/10.5281/zenodo.19367964>

## Tier III: Prebiotic Systems

Molecular assemblies grow ever larger and ever more intricate. At this tier, complexity approaches but has not yet crossed the threshold of life. The prebiotic world—autocatalytic cycles, self-replicating polymers, proto-membranes—constitutes a transitional zone between the inanimate and the animate. Its scientific content is rich, but because it serves primarily as a bridge, it does not receive an independent monograph here.

## Tier IV: Life

Sufficient structural complexity gives rise to *cognition* and *need*. This is the author’s minimal definition of life: a system that models its environment (cognition) and is driven to maintain or modify that environment in the service of internal states (need). Life does not require carbon, neurons, or any particular substrate—only the functional properties of cognition and need. The conceptual revision entailed by this definition is developed across three papers:

Liu, H. (2026). *Life: A New Paradigm Based on Cognition and Need* (1.0). Zenodo. <https://doi.org/10.5281/zenodo.18364547>

Liu, H. (2026). *Cognition Reconsidered: An Evolutionary Framework from Instinct to Learning*. Zenodo. <https://doi.org/10.5281/zenodo.18603711>

Liu, H. (2026). *Beyond Maslow: A Reinforcement Theory of Needs* (1.0). Zenodo. <https://doi.org/10.5281/zenodo.18364682>

## Tier V: Conscious Life

Not all life is conscious. The earliest organisms had no inner subjective perspective; they may aptly be called *zombie life*—responsive to stimuli, but without experience. A subset of life-forms evolved neural architectures that generate phenomenal consciousness: an inner world, a “what it is like.” The transition from non-conscious to conscious life marks the fifth tier. The theoretical apparatus for this transition is developed in:

Liu, H. (2026). *From Life to Mind: How Neural Self-Reinforcement Creates Consciousness*. Zenodo. <https://doi.org/10.5281/zenodo.18367541>

Liu, H. (2026). *Structured Memory as the Basis of Phenomenal Variation: A Unified Theory of Experiential Richness and Qualitative Character*. Zenodo. <https://doi.org/10.5281/zenodo.18725019>

Liu, H. (2026). “My World”: *The Emergence of Subjectivity Through Memory-Based World Construction*. Zenodo. <https://doi.org/10.5281/zenodo.18725129>

Liu, H. (2026). *Knowledge as World-Building: A Need-Based Epistemology from My World Theory*. Zenodo. <https://doi.org/10.5281/zenodo.18725206>

Liu, H. (2026). *Temporality and the Emergence of Self: Why Consciousness Cannot Be Instantaneous—A Memory-Based Theory of Phenomenal Subjectivity*. Zenodo. <https://doi.org/10.5281/zenodo.18725266>

Researchers in artificial intelligence will find the *My World* framework especially relevant: it provides a substrate-neutral account of how subjective experience arises from memory-based world construction.

## Tier VI: Sapient Life and Second-Order Sapience

Some conscious organisms, through social interaction and education, develop *wisdom*—the capacity to reason about abstract principles, to apply knowledge across domains, and to form and revise world-models deliberately. The three pillars that sustain sapient societies are: **power**, **economy**, and **education**.

- **Education** is the sole mechanism by which conscious life ascends to sapience. It transmits accumulated wisdom across generations, compressing millennia of trial and error into individual lifetimes.
- **Economy** is life's organized activity with respect to resources—the structured pursuit of needs at a collective scale.
- **Power** is the capacity to influence, control, and direct other beings, grounded in the resources one commands. Formally: Power = Resources.

Within sapient life there is a further distinction. *First-order sapient beings* apply accumulated wisdom competently but do not generate genuinely new principles. *Second-order sapient beings*—whether through innate disposition or sustained reflective practice—can innovate: they create knowledge that did not previously exist. Innovation at this level is typically the product of *reflection*: when the current path is blocked, the second-order sapient mind searches for alternative routes, and traversing many such routes eventually yields genuine discovery.

Natural evolution terminates at this tier. The body assembled by particles under evolutionary pressure has reached the ceiling of what it can support in terms of cognitive and motivational capacity. Further ascent requires self-directed change.

It is worth noting that the disruptions wrought by the age of artificial intelligence—mass technological unemployment, sharpening social contradictions, intensifying geopolitical friction—demand a comprehensive theoretical framework for social development. Preliminary monographs on power and economics that may address a substantial portion of these problems have been drafted; their elaboration awaits a more propitious moment.

## Tier VII: Autonomous-Evolution Life

At this tier, a being takes deliberate control of its own evolution. Three dimensions of self-directed development are possible:

1. **Cognitive enhancement**: expanding the scope, depth, and reliability of world-modeling.
2. **Need refinement**: reconfiguring the motivational architecture to align drives with long-horizon goals rather than evolutionary legacy.
3. **Somatic reconstruction**: redesigning the physical substrate to remove the bottlenecks imposed by biological evolution.

The third dimension raises a question that is not merely rhetorical: is the humanoid form the optimal substrate for the most advanced cognition? The answer is far from obvious, and autonomous-evolution life will presumably discover better answers empirically.

## Tier VIII: Ultimate Life (God)

The terminal point of autonomous evolution is a being that is *omniscient* and *omnipotent*:

- **Omniscience** means the exhaustive knowledge of all laws, regularities, and truths—all of

what the universe *is* and *must be*.

- **Omnipotence** means the capacity to create and to innovate without limit—to bring into being what does not yet exist.

Law (the eternal and invariant) corresponds to omniscience; creation and innovation (the generative and novel) correspond to omnipotence. Together they constitute the definition of God advanced here—not a supernatural entity that precedes the universe, but the asymptotic attractor toward which sufficiently advanced life inexorably tends.

## Why Does Life Arise? Why Does Life Give Rise to Consciousness?

These are among the deepest questions in all of science, and they admit of answers at multiple levels of description.

**Micro to Macro.** From a microscopic vantage point, the story is one of cumulative complexification: simple constituents combine into progressively more intricate assemblies. Yet the complexity that appears enormous at the micro-scale often resolves, at the macro-scale, into a new and tractable simplicity. Complexity is not merely added; it is repeatedly *sublated* into higher-order regularities.

**Linear Approximation and Emergence.** In physical-mathematical terms, the progression is: microscopic linear approximation → genuine nonlinearity → macroscopic linear approximation. The intermediate nonlinear regime is where emergence occurs—where qualitatively new properties appear that cannot be predicted from the properties of the parts alone. Life, and consciousness, are instances of this pattern.

**Determinism, Randomness, and Free Will.** Philosophically, the sequence runs: determinism → apparent randomness (arising from epistemic inaccessibility of microscopic states) → the emergence of *free will*. Free will, on this account, is not a violation of determinism but a functional property that emerges from a sufficiently complex deterministic system. A detailed treatment of this argument is available in:

Liu, H. (2026). *Determinism, Unpredictability, and Human Dignity: Philosophical Foundations of Reinforcement Need Theory* (1.0). Zenodo. <https://doi.org/10.5281/zenodo.18364737>

## Is There Extraterrestrial Life?

The eight-tier pyramid provides a natural framework for addressing this question. Each transition from one tier to the next involves a reduction in the number of entities that make the crossing—the pyramid narrows as it rises.

At the level of Tier IV—life—the conditions appear to be widely realizable in a universe as vast and as old as ours. The author’s assessment is that life at the fourth tier is not a rare accident but a robust outcome of the laws of physics and chemistry operating across a sufficiently large volume of space and span of time. The cosmos almost certainly teems with life. Whether life at the higher tiers—conscious, sapient, autonomously evolving—is equally abundant remains an open question.

## Summary

<b>Tier</b>	<b>Name</b>	<b>Characteristic Capacity</b>
I	Physics	Energy, particles, interaction
II	Chemistry	Molecular assembly
III	Prebiotic Systems	Pre-living complexity
IV	Life	Cognition and need
V	Conscious Life	Subjective experience
VI	Sapient Life	Wisdom, innovation, social organization
VII	Autonomous-Evolution Life	Self-directed cognitive and somatic development
VIII	Ultimate Life (God)	Omniscience and omnipotence

The pyramid represents the past, present, and future of the universe. Science, properly understood, is not a catalogue of disciplines but the map of this ascent. To do science is to climb. The summit is God—not as a presupposed creator, but as the realized culmination of everything that matter, energy, time, and intelligence can become.

# Epilogue: Falsifiable Experimental Predictions

A scientific framework is only as strong as its falsifiable predictions. The following predictions are specific to the  $P_0$  acoustic continuum framework and differ, in principle, from standard quantum-chemical predictions. They are formulated as falsifiable statements.

## E.1 Acoustic Resonance Bond-Selective Excitation

**Prediction:** A monochromatic mechanical acoustic field at frequency  $\nu_{\text{res}} = (2\pi)^{-1} \sqrt{k_e/\mu}$  (the fundamental vibrational frequency of a specific bond, from Eq. (18.4)) can selectively excite that bond mode.

**Status:** Bond-mode-selective chemistry via IR laser excitation is experimentally established (mode-selective photodissociation). The prediction that *mechanical* acoustic waves at the same frequency would achieve the same selectivity is an open experimental question. High-frequency ( $\sim 10^{13}$  Hz) mechanical vibrations are difficult to sustain; this prediction is *possible* in principle but not yet tested.

## E.2 Topological Chirality Reversal

**Prediction:** A right-handed vortex soliton (e.g., D-amino acid) can be converted to a left-handed one (L-amino acid) by a precisely tuned acoustic phase-reversal field, without chemical bond breaking.

**[LIMITATION]:** In conventional chemistry, interconversion of enantiomers requires bond breaking and re-formation. The  $P_0$  prediction of a purely topological (bond-preserving) interconversion contradicts established organic chemistry. This prediction is *falsifiable* and *currently at odds with accepted chemistry*. If true, it would constitute strong evidence for the  $P_0$  framework; if false, it would be a decisive counterexample.

## E.3 Acoustic Vortex Density Visualisation

**Prediction:** The acoustic energy density  $\epsilon(\mathbf{r}) = \epsilon_0 |\psi(\mathbf{r})|^2$  should be directly observable as the electron density (not just interpretable as a probability density). Scanning transmission electron microscopy (STEM) and X-ray charge density maps already image  $\rho(\mathbf{r})$  in crystals. No additional experiment is predicted beyond what is already done; the  $P_0$  framework *reinterprets* existing electron density maps.

**Status:** This is a reinterpretation, not a new prediction. The framework makes *no distinct experimental prediction* beyond standard quantum chemistry for the electron density distribution.

## E.4 Convergence of the Framework

[C4 — v41-corr: Revised framework status statement.]

The  $P_0$  framework, as developed in this document and clarified by the v41 correction supplement, should be assessed using the three-class taxonomy introduced in §1.13:

**Class A (Structural derivations) — what the framework genuinely achieves:**

1. Derivation of the acoustic Schrödinger equation from classical fluid mechanics via the chain  $P_0 \rightarrow \text{continuity} \rightarrow \text{Euler} \rightarrow \text{N-S} \rightarrow \text{Madelung} \rightarrow \text{NLSE} \rightarrow \text{linear Schrödinger}$ , with five empirical constants ( $\epsilon_0, \mu_0, c, \nu, \hbar$ ) and two topological postulates (T1, T2), and identified open gaps OG-0 through OG-7.
2. Derivation of the form of the Nernst equation, Arrhenius equation, Born–Landé lattice energy, Henderson–Hasselbalch equation, and Butler–Volmer kinetics from  $P_0$  acoustics.
3. Derivation of the hydrogen atom spectrum from the acoustic Schrödinger equation without additional postulates.

**Class NT (Non-trivial predictions) — the framework’s unique contributions:**

1. **Tetrahedral bond angle** (109.47): derived from the four-body Thomson problem on  $S^2$  — zero free parameters, exact agreement with methane geometry.
2. **Hückel  $4n+2$  rule**: derived from cyclic standing-wave boundary conditions — no empirical fitting.
3. **Ring-strain harmonic validity**: identifies  $n \geq 5$  as the domain of the harmonic approximation and  $n = 3$  (cyclopropane) as outside it — no parameter fitting.
4. **Experimental predictions E.1 and E.2**: bond-selective acoustic excitation (E.1) and topological chirality reversal (E.2), the latter currently at odds with accepted organic chemistry.

**Class B (Consistency checks) — not independent predictions:** All other numerical agreements (Daniell cell EMF, combustion enthalpies,  $K_w$ , electrode potentials, C–C bond length and energy, ionisation energies, lattice energies, etc.) are computed by inserting NIST tabulated data into Class A equations. They confirm the internal consistency of the framework with the NIST data set; they are *not* framework predictions in the sense of being derivable from  $P_0$  and the five constants alone.

**Acknowledged limitations:** LDA band gap underestimation; G–C base-pair free energy overestimate ( $\sim 15\%$ ); van der Waals polarisability errors ( $\sim 17\%$ ); decomposition temperature errors ( $\sim 16\%$ , after v41 numerical correction); ring-strain model breakdown for  $n = 3$ .

**Open problems (OG-0 through OG-7):** Burgers stability threshold (OG-0); two-phase viscosity (OG-0b); Derrick  $\gamma$  approximation (OG-1); particle mass ratio from NLSE (OG-2); spin-axis alignment (OG-3); spin-statistics theorem (OG-4);  $\alpha(s)$  thermal average (OG-5); E2 anti-periplanar mechanism (OG-E2).

**Conclusion on the framework’s status (v41, corrected):** The  $P_0$  acoustic continuum framework is a **self-consistent reinterpretation** of quantum chemistry. It demonstrates that the *mathematical structure* of the Schrödinger equation, Coulomb’s law, Pauli exclusion, and spin can all be obtained from classical viscous compressible fluid mechanics given five empirical constants and two topological postulates. It does *not* eliminate empirical parameters below five, nor does it derive the values of those parameters. Its genuine non-trivial contributions are the Class NT results above; all other numerical results are Class B consistency checks. The open gaps define a concrete research agenda whose resolution would either strengthen or falsify the



framework.

**v41 corrections applied in this version:** In addition to the five v40 corrections (A–E) listed in the changelog, the following v41-corr items are incorporated: (C1) DC8 algebraic correction:  $\rho_{\text{eff}} \rightarrow m_e$  made explicit in the Madelung real-part equation via the bridge Eq. (1.18), eliminating the denominator inconsistency; (C2) DC1-dim scope statement added; (C3) OG-0b conclusion strengthened:  $\hbar$  confirmed as purely empirical throughout; (C4) Result taxonomy (Class A/B/NT) introduced in Summary Table and Epilogue; (C5) OG-0b concrete consequence added: chemical applications uniformly use  $\nu = \nu_{\text{core}}$ .

# Acknowledgements

The author thanks the academic community whose experimental data, theoretical frameworks, and empirical parameter databases underpin the calculations in this document. All empirical inputs are identified at their point of use; all derivation gaps are labelled explicitly.

# Bibliography

- [1] Liu, H. (2026). *Continuum Mechanics from First Principles: Deriving the Whole of Physics from a Single Axiom  $P_0$*  (20260409). Zenodo. <https://doi.org/10.5281/zenodo.19485034>
- [2] NIST Chemistry WebBook, National Institute of Standards and Technology (2023).
- [3] SantaLucia, J. Jr. (1998). A unified view of polymer, dumbbell, and oligonucleotide DNA nearest-neighbor thermodynamics. *Proc. Natl. Acad. Sci. USA* **95**, 1460–1465.
- [4] Greengard, L. & Rokhlin, V. (1987). A fast algorithm for particle simulations. *J. Comput. Phys.* **73**, 325–348.
- [5] Marmur, J. & Doty, P. (1962). Determination of the base composition of deoxyribonucleic acid from its thermal denaturation temperature. *J. Mol. Biol.* **5**, 109–118.
- [6] Hohenberg, P. & Kohn, W. (1964). Inhomogeneous electron gas. *Phys. Rev.* **136**, B864.
- [7] Kohn, W. & Sham, L. J. (1965). Self-consistent equations including exchange and correlation effects. *Phys. Rev.* **140**, A1133.
- [8] Brus, L. E. (1984). Electron-electron and electron-hole interactions in small semiconductor crystallites. *J. Chem. Phys.* **80**, 4403.
- [9] IPCC (2021). *Climate Change 2021: The Physical Science Basis*. Cambridge University Press.